A BOUNDARY-FITTED NON-ORTHOGONAL GRID TECHNIQUE FOR INCOMPRESSIBLE TURBULENT SWIRLING FLOWS

BY

AFIF S. HALAL

Bachelor of Science
Oklahoma State University
Stillwater, Oklahoma
1982

Master of Science
Oklahoma State University
Stillwater, Oklahoma
1983

Submitted to the Faculty of the
Graduate College of the
Oklahoma State University
in partial fulfillment of
the requirements for
the Degree of
DOCTOR OF PHILOSOPHY
December, 1991

A BOUNDARY-FITTED NON-ORTHOGONAL GRID

TECHNIQUE FOR INCOMPRESSIBLE

TURBULENT SWIRLING FLOWS

Thesis Approved:

David G. Lilley.
Thesis Adviser

Peter H. Worel

Jan Wagner

Ronald L. Dougherty

Thomas C. Collins
Dean of The Graduate College

ACKNOWLEDGEMENTS

I would like to express my sincere gratitude and appreciation to Dr. David G. Lilley for the opportunity to work under his supervision. His advice and encouragement were invaluable in guiding the completion of this study. Many thanks are also due to the members of the advisory committee, Dr. Peter M. Moretti, Dr. Ronald L. Dougherty, and Dr. Jan Wagner, for their help and suggestions.

I also express my gratitude to Dr. Larry L. Hoberock, head of the Mechanical and Aerospace Engineering Department, for his constant encouragement and financial support.

Special thanks are due to my grandparents, mother and father in-law, and brothers for their inspiration and moral support.

This thesis is dedicated to my caring wife, Kimberly, and parents, Samih and Fatima, for their loving concern and selfless support. They encouraged me all the way and helped me keep the end goal in sight. To them I extend my deepest appreciation and love.

TABLE OF CONTENTS

LIST OF TABLES

LIST OF FIGURES

NOMENCLATURE

a	Overall coupling coefficient in the finite difference equation
A	Inlet diameter of test case 6
b	Defined coefficient in Table I
B	Diameter of quarl exit for test case 6
C	Convective contribution to the overall coupling coefficient
C_1	Turbulence model constant
C_2	Turbulence model constant
C_μ	Turbulence model constant
CRZ	Corner recirculation zone
CTRZ	Central toroidal recirculation zone
D	Diffusive contribution to the overall coupling coefficient
D_c	Chamber diameter
D_f	Furnace diameter
D_o	Tube diameter
E	Law of the wall constant
e,E	Eastern neighbor
E'	Projected eastern neighbor
f	Relaxation factor
FDE	Finite difference equation
G_k	Turbulence generation term
G^k	Grid hierarchy coefficient

h	Grid spacing
k	Turbulence kinetic energy
l	Macroscale of turbulence
L	Interpolation function
n,N	Northern neighbor
NE	Northeastern neighbor
NW	Northwestern neighbor
P	Time-mean pressure
P	Nodal point
PDE	Partial differential equation
PVC	Precessing vortex core
r	Radial coordinate
R	Chamber or tube radius
R_p	Stability coefficient
S^φ	Source term
S_p	Linearized Source coefficient
S_U	Linearized source coefficient
s,S	Southern neighbor
SE	Southeastern neighbor
SW	Southwestern neighbor
t	Time coordinate
u	Time-mean axial velocity
U	Total velocity
U_τ	Friction velocity
U^+	Dimensionless variable for wall function
v	Time-mean radial velocity
w	Time-mean tangential velocity

w,W	Western neighbor
W′	Projected western neighbor
x	Axial coordinate
Y^+	Dimensionless variable for wall function
Y_p	Normal distance from wall to nearest grid point

Greek Symbols

ß	Control coefficient for convective terms
ϵ	Turbulence energy dissipation
η	Normalized radial coordinate
θ	Flow angle relative to x-axis
θ_o	Sloping wall angle relative to x-axis
κ	Von Karman constant
μ	Laminar dynamic viscosity
μ_t	Turbulent viscosity
μ_{eff}	Effective viscosity
ξ	Normalized axial coordinate
π	Numerical constant
ρ	Fluid density
σ_k	Turbulent Prandtl/Schmidt number for k
σ_ϵ	Turbulent Prandtl/Schmidt number for ϵ
τ	Shear stress
φ	General dependent variable
ψ	Stream function
ω	Vorticity
Δx	Grid spacing in axial direction
Δr	Grid spacing in radial direction

Δt	Time step
Γ	General diffusion coefficient

Subscripts

c,f	Chamber or furnace
e	Half-way location between eastern and central cell points
E	Location of eastern cell point
E'	Location of projected eastern point
i	Location of vertical gridline
j	Location of 'horizontal' gridline
i,j	General grid point location
in	Inlet condition
max	Maximum value
n	Half-way location between northern and central cell points
N	Location of northern cell point
NE	Location of northeastern cell point
NW	Location of northwestern cell point
o	Inlet condition
P	Location of central cell point
s	Half-way location between southern and central cell points
S	Location of southern cell point
SE	Location of southeastern cell point
SW	Location of southwestern cell point
w	Wall condition
w	Half-way location between western and central cell points

W	Location of western cell point
W′	Location of projected western point
φ	General dependent variable

Superscripts

(0)	Zeroth-order function
(1)	Linear function
(2)	Quadratic function
φ	General dependent variable
′	New time level
—	Time-mean quantity

CHAPTER I

INTRODUCTION

Preamble

The efficient design and development of practical flow equipment requires careful characterization and optimization of very complicated fluid mechanical and physical/chemical processes. These entail vortex motion, turbulence, chemical reaction, droplet and particle motion, multi-phase behavior, etc. Traditional design procedures have been forced to rely extensively on experiments, an approach if utilized to the exclusion of available analytical or computational methods, would soon prove both costly and incapable of assimilating the immense amount of design information. As a consequence, computer modeling is becoming increasingly more attractive as a complementary tool to assist in preliminary screening of design ideas, and diagnosing and solving development problems (Refs. 1 through 8).

To be reliably utilized, the computer model should simulate the flow in all its important respects (boundary conditions, turbulence, flow geometry, etc.), and provide a means whereby the governing equations may be solved cheaply and accurately. The governing equations are nonlinear and must be solved simultaneously. Similarity between them and

their diffusional relations allows them to be cast in a common form and solved in a similar manner.

Several computer models have emerged in recent years based on these principles, each having its strengths and weaknesses. The basic differences between them include: the closure of the turbulence model, the location of the variables in the computational grid, the discretization scheme, and the solution technique.

Typically, they are axisymmetric and involve pressure-velocity (primitive-variable) or stream function-vorticity formulation. Turbulence is usually simulated by way of a two-equation model, and more recently using second moment closure. The finite difference equations are obtained from a Taylor series expansion about nodal points, or a control volume approach using a staggered grid system. Solution techniques vary from the simple point Gauss-Siedel method to the more efficient line-by-line SIMPLE (semi-implicit method for pressure linked equations) method for steady-state problems, with corresponding explicit and SIMPLE methods for associated transient problems.

The Problem

The present study is concerned with the prediction of axisymmetric incompressible turbulent swirling flowfields, using stream function-vorticity formulation. A schematic illustration of a typical flowfield is shown in Figure 1. The sudden enlargement creates a CRZ (corner recirculation

zone) whose size and shape are controlled by the expansion ratio and any other factor which manipulates the pressure gradient.

The introduction of swirl induces pressure fields to balance centrifugal forces, and the decay of swirl caused by shear and mixing sets up adverse pressure gradients. The radial profile of the time-mean axial velocity depends on the degree of swirl imparted to the flow. For weak swirl, the profile remains gaussian in form with its maximum along the jet axis. For strong swirl, the forces prompted by the adverse pressure gradients could exceed the forward kinetic forces of the flow and result in flow recirculation near the centerline. An inlet quarl aids the swirling jet to follow the slope of the wall, thus promoting streamtube divergence, intensifying the central recirculation zone, and reducing the degree of swirl required to achieve a certain level of recirculation. The degree of swirl imparted to the flow is characterized by a swirl number, which represents the ratio of the axial flux of tangential momentum and the axial flux of axial momentum.

Calculation of such flows is very difficult. They are bounded by irregularly-shaped boundaries, and exhibit flow rotation, large velocity gradients, and strong streamline curvatures. As a result, turbulence modeling and numerical problems play a critical role in their analysis.

Leaving aside the impediments of turbulence modeling, it is clear that present calculation methods based on the

finite difference approach suffer from two key weaknesses: (a) they lack flexibility with respect to irregularly-shaped boundaries for the calculation domain, and (b) they require excessively fine grids to control numerical diffusion.

Generally, flow domains are discretized to fit the coordinate system, which requires that a rectangular grid (uniform or nonuniform) and a stair-step approach be used to represent irregular boundaries. The use of stair-steps has a number of implications. First, boundary distances are always distorted. Thus, irrespective of physical modeling and numerical accuracy, calculation of near-wall properties can never be correct. Second, adequate representation of the geometry bounding the flow usually requires an enormous amount of computer storage. Therefore, mesh refining to control numerical diffusion is not possible, and the calculated flowfield may be influenced incorrectly by the geometric representation.

To circumvent this problem, coordinate transformation methods have been used in orthogonal or nonorthogonal ways, and implemented via analytical and/or numerical techniques. Although they resolve the fundamental problem of irregular-boundary representation, transformation methods exhibit geometrically-induced errors resulting from failure to satisfy certain consistency conditions.

Clearly, more realistic approaches are possible in the interest of accuracy, but it is not clear to what extent

penalties will emerge in terms of conceptual simplicity, universality, and additional computer time and storage.

Objectives

The principal objectives of the present study are to develop, implement, and evaluate a theoretical/computational model for predicting incompressible turbulent swirling flows in domains typical of industrial furnaces and gas turbines.

The study focuses on the fundamental nonorthogonal grid coverage of an axisymmetric flow domain with irregular boundaries, and involves incorporating swirl and turbulence effects into a stream function-vorticity simulation.

Model evaluation is accomplished via application to experimental data cases of varying degrees of complexity. Laminar cases are used to confirm numerical accuracy, and turbulent cases are examined to establish the workability of the solution procedure in complex flow situations.

The solution procedure, which is embodied in a newly developed computer code, entails the following features:

1. Stream function-vorticity variables
2. Time-dependant calculations
3. Two-equation (k-ϵ) turbulence model
4. Swirl velocity calculations
5. Rectangular and/or non-rectangular grid
6. Displaced, linear, and quadratic interpolation
7. Generalized boundaries
8. Adaptive stability scheme

The simulation is restricted to isothermal incompressible flows and axisymmetric cylindrical coordinates.

Outline of the Thesis

In Chapter II, a review of the literature is presented which focuses on those works which represent highlights in the development of the subject, and which served as a guide in the development of the present work.

The mathematical and physical model are presented in Chapter III while the numerical solution procedure is described in Chapter IV.

The predictive capability of the computer model is assessed in Chapter V; and Chapter VI recapitulates the main conclusions of the study, and outlines recommendations for future work.

CHAPTER II

LITERATURE REVIEW AND ANALYSIS

Introduction

In this chapter, a review of the literature is presented so as to connect the present work with previous contributions. It is not the intention here to present an exhaustive review; rather it is chosen to concentrate on those works which represent highlights in the development of the subject, and which served as a guide in the development of the present work. The chapter is divided into two major sections. The first section is devoted to the presentation of recent advances in numerical methods relative to fluid flow and heat transfer computations; and the second section is aimed at reviewing relevant experimental and theoretical investigations of turbulent swirling flows.

Numerical Methods in Fluids and Heat Transfer

Discretization Schemes

The finite difference analog of the governing equations is obtained by overlaying a computational mesh on the flow domain, and obtaining the appropriate finite difference

equations for every node using a discretization scheme. Accuracy of the discretization scheme can generally be judged from the order of the terms of an equivalent Taylor Series that have been retained in the expansion. However, accuracy and stability represent conflicting requirements with respect to these terms.

Attempts to discretize the convective terms using the central differencing scheme (CDS) failed to produce wiggle-free solutions for high Reynolds number flows (Refs. 5 and 6). The Hybrid and upwind differencing schemes (HDS and UDS), which are based on a purely one-dimensional flux balance, were found to eliminate these wiggles, and perform well in the regions where the flow is aligned with the grid lines and convection is balanced primarily by stream-wise diffusion rather than cross-stream diffusion or sources. However, if such idealized conditions are not encountered, the locally one-dimensional assumption gives rise to severe truncation errors, known as numerical false diffusion, which may become so dominant as to obscure the effects of physical diffusion on the flow. These shortcomings have led to the development of improved schemes which attempt to account for the effect of flow-to-grid skewness, the lateral transport, and the presence of sources.

The locally analytic differencing scheme (Ref. 9), known as LOADS, takes into account the influence of the lateral transport and source terms. The computational cell involves five points, the coupling coefficients are always

positive, and the algebraic equations are diagonally dominant. However, source terms are calculated explicitly and may lead to convergence difficulties, especially if the equations are strongly coupled.

The linear flux-spline scheme (Ref. 10) accounts for sources and lateral transport by assuming a piecewise-linear variation for the total flux. In principal, it is similar to LOADS, both in its properties and computational details, but varies only in the manner in which the source terms are introduced.

The skew-upwind differencing scheme (Ref. 11), known as SUDS, is only formally first-order accurate but produces a significant reduction in numerical diffusion by accounting for the flow-to-grid skewness. Here the convective flux is obtained by employing upwind differencing along streamlines which are defined by the velocity direction. It employs a compact nine-point computational cell, and is conservative but conditionally stable.

The quadratic upstream differencing scheme (Ref. 12), known as QUDS, utilizes upstream-shifted quadratics and is free of any second-order numerical diffusion. It employs a sparse nine-point computational cell, and is conservative but conditionally stable.

The controlled numerical diffusion with internal feed back scheme (Ref. 13), known as CONDIF, is a variant of the central differencing scheme (CDS). It eliminates the wiggles by explicitly introducing a controlled amount of

numerical diffusion based on the local gradients. The computational cell involves only five points. The coupling coefficients are nonlinear, since they involve the gradient of the dependent variable and must be recalculated with each iteration.

In several studies (e.g., Refs. 14 through 23), these improved schemes, among several others, have been proven to produce significantly more accurate results than the simple first-order upwind scheme.

Representation of Geometry

Present finite difference calculation methods lack flexibility with respect to irregularly-shaped boundaries for the computational domain. Typically, the physical domain is discretized to fit the coordinate system, which requires that a rectangular grid (uniform or nonuniform) and a stair-step approach be used to represent irregular boundaries.

The use of stair-steps has a number of implications. First, boundary distances are always distorted. Hence, irrespective of physical modeling and numerical accuracy, calculation of near-wall properties can never be correct. Second, appropriate representation of the geometry bounding the flow to be calculated usually requires a large amount of computer storage. Consequently, mesh refining to control numerical diffusion is not possible, and the calculated

flowfield may be influenced incorrectly by the geometric representation.

To circumvent this problem, alternate approaches have been proposed which use coordinate transformation methods in orthogonal or nonorthogonal ways, and implemented via analytical or numerical techniques (Refs. 24 through 27). Although they resolve the fundamental problem associated with irregular boundaries, transformation methods often exhibit errors resulting from failure to satisfy certain consistency conditions.

Moreover, An orthogonal mesh may become unsuitable for calculations near sharp corners, since the grid distribution tends to be sparse. As a consequence, large mesh densities must be tolerated elsewhere to achieve corner calculations with acceptable accuracy.

Solution Techniques

The algebraic equations following the discretization of the governing equations are usually coupled and nonlinear. Sequential solution methods (Refs. 5 and 6) are currently very popular because of their simplicity and low computer storage requirements. However, if the inter-equation coupling is strong, these methods exhibit severely poor convergence rates.

Alternate methods in which all the variables are simultaneously updated have been proposed. These include coupled point Gauss-Siedel and line Gauss-Siedel methods

(Refs. 5 and 6). Direct solution methods of the mass and momentum transport equations have also been proposed (Refs. 28 and 29), but these require excessively large computer storage.

Iterative methods, such as the Gauss-Siedel point and Gauss-Siedel line methods, are known to converge rapidly for the first few iterations but very slowly thereafter. That is, they are very effective in smoothing out errors of wave length comparable to the grid spacing, but are very slow in diminishing the low-frequency ones (Ref. 30). Thus, as the grid is refined, the increasing dominance of low-frequency errors results in excessively large computational efforts.

In order to alleviate this problem, multigrid solution techniques have been proposed (Refs. 30 through 33), which employ a hierarchy of grids G^k, $k = 1, 2, 3, \ldots M$, with the mesh spacing such that $h_{k+1} = h_k/2$. When the convergence rate on the fine grid becomes slow, the multigrid method switches to a coarser grid, where the low-frequency errors are more effectively removed. The solution on the fine grid is then corrected to reflect the removal of these errors.

Turbulent Swirling Flows

General Features

Swirling flows (Ref. 1) result from application of a tangential velocity component being imparted to the flow by use of a swirl generator positioned upstream from the reactor or expansion chamber. Various modes of generation

have been utilized to accomplish this task: tangential entry swirler, guide vanes, multi-annular swirler, rotating honeycomb, and high speed pipe rotation. Obviously, several structural and geometrical perturbations may exist for each mode with their accompanying disparities in efficiencies and resultant velocity profiles.

Swirl velocity profiles generally assume a combination of free and forced vortex distribution. The time-mean swirl velocity distribution must go to zero at the centerline as well as at the enclosure wall. The inner field tends to be solid-body rotation (i.e., forced vortex), and the outer field develops towards a state of constant angular momentum or a free vortex (Refs. 34 and 42).

In an isothermal or inert jet, swirl acts to enhance the rate of jet growth, entrainment, and mean velocity decay relative to a nonswirling jet (Refs. 1 and 2). As swirl is progressively increased, pressure fields are induced to balance centrifugal forces and the decay of swirl caused by shear and mixing with the surrounding fluid sets up adverse pressure gradients.

The radial profile of the time-averaged axial velocity depends on the degree of swirl imparted to the flow. For weak swirl, the profile remains gaussian in form with its maximum along the jet axis. For strong swirl, the forces prompted by the adverse pressure gradients could transcend the forward kinetic forces of the flow and result in flow reversal or vortex breakdown.

In a reacting flowfield, the primary use of the swirl-induced CTRZ (central toroidal recirculation zone) is to promote flame stabilization and control pollutants emission. Flame retention requires that the flame velocity matches or exceeds the forward flow velocity, and that sufficient heat is imparted for stable ignition. In nonswirling flowfields, the stabilization mechanism is usually controlled by a wall boundary layer, an expansion chamber, or a mechanical flame holder. However, in swirling flowfields, the combination of swirl velocity distribution, furnace geometry, and air/fuel ratios produce a number of CTRZ configurations which provide the necessary mechanism for better mixing, flame retention, and emission control.

Experimental Work

It is not surprising that the significant number of experimental studies of swirling flows have produced a broad diversity of parametric effects and observations. Differing swirl generators, inlet and chamber geometries, flow rates and fuels, all produce details and differences which may not be easily resolved. Nevertheless, it is the purpose of this review section to depict common threads among the cases that have been observed.

Owen (Ref. 43) measured time-averaged characteristics in the initial mixing region of free and confined coaxial air jets with and without swirl. He indicated that there were substantial large-scale contributions to the total RMS

turbulent velocity field from inlet swirl. These large-scale fluctuations resulted in significant deviations from isotropy over most of the initial mixing region, indicative of the inadequacy of turbulence models based on the local equilibrium principles in representing the physics of such flows. The data also displayed that the recirculated mass flux and the size of the CTRZ are significantly larger in confined conditions than in free expansion.

Habib and Whitelaw (Refs. 44 and 45) investigated the velocity characteristics of confined coaxial jets with and without swirl. They measured the time-mean axial velocity and the RMS axial velocity fluctuations. The measurements indicated that larger annulus to center jet velocity ratios produce lager CTRZs and higher turbulence intensities. An increase in inlet swirl was also observed to increase the size of the CTRZ.

Vu and Gouldin (Ref. 46) investigated the flowfield characteristics of a model swirl combustor under co- and counter-swirl conditions, without chamber expansion. They measured time-averaged velocities, turbulence intensities, and turbulent stresses. They noted that the secondary jet swirl has a prominent influence on the formation of the CTRZ, and that high levels of turbulence fluctuations and dissipation rates characterized the central flow region for both co- and counter-swirl conditions.

Yoon and Lilley (Ref. 47) investigated the mean flow characteristics of turbulent swirling jets in suddenly and

gradually expanding chambers. The primary concern of their study was to characterize flows of this type in terms of the effects of sidewall angle, swirl strength, inlet turbulence intensity, and expansion ratio on the resulting flowfield. They reported that the presence of swirl shortens the CRZ and generates a CTRZ followed by a precessing vortex core.

An increase in swirl was found to, at least initially, expand the CTRZ in width and length, and a further increase caused the length to decrease with significant increase in width.

A gradually expanding inlet was found to cause the swirling jet to follow the slope of the wall. This had the effect of augmenting the central adverse pressure gradients, intensifying the recirculated mass flux, and decreasing the degree of swirl necessary to achieve a particular level of recirculation.

The presence of a chamber contraction at a downstream location produced a favorable pressure gradient which was superimposed on the adverse pressure gradient promoted by swirl. In certain cases where the contraction was strong enough to influence the upstream field, the intensity of the CTRZ was diminished.

Roback and Johnson (Refs. 48 through 50) studied the downstream mixing of coaxial water jets discharging into an expanded duct. They employed a visualization technique to qualitatively study the time-dependent flow characteristics and the scale of turbulence. They reported that intensive

mixing regions existed at the interface between the near stream and the centerline recirculation zone, and at the interface between the inner and outer jet streams. Mixing for swirling jets was found to complete in one-third of the distance required for nonswirling jets.

Other significant experimental studies, with findings and conclusions similar to those described above, are given in References 51 through 54.

Theoretical Work

Numerous Publications exist which discuss at length theoretical approaches to the solution of turbulent swirling flows. For example, see textbooks on flowfield modeling (Refs. 1 through 4), computational fluid dynamics (Refs. 5 through 8), and turbulence modeling (Refs. 55 and 56). A brief review of related research papers follows.

Numerical predictions of confined axisymmetric swirling jets were made by Lilley (Ref. 57), using a stream function-vorticity variable approach. Turbulence was simulated by way of a simple turbulent viscosity formula. The general agreement of predictions with associated experimental data was encouraging in view of the use of a simple turbulence model.

A confined swirling flow in an axisymmetric furnace configuration was predicted by Khalil et al. (Ref. 58). They employed a two-equation (k-ϵ) turbulence model and a primitive-variable (pressure and velocity) formulation. The

calculation procedure was based on the SIMPLE (Semi-Implicit Method for Pressure Linked Equations) method of Patankar and Spalding (Ref. 6). Predicted axial velocity profiles for the experimental data case of Baker et al. (Ref. 59) were found to be in reasonable agreement with the measurements.

Karasu (Ref. 60) predicted turbulent swirling flows in circular-sectioned ducts and annuli, using a similar model to that of Khalil et al. (Ref. 58). His results highlight the shortcomings of the two-equation k-ϵ turbulence model in reproducing the stabilizing effects of swirl, particularly in flows featuring a combined vortex distribution.

Sloan (Ref. 61) presented an extensive evaluation of several turbulence models for predicting strongly swirling flows. He noted that of all the possible models and model corrections that were evaluated, the Reynolds stress model holds the greatest potential for prediction improvement. However, he recommended that present predictions maintain the k-ϵ model due to the marginal improvement that higher-order schemes provide relative to their added complexity and increased computational and storage requirements.

Jones and Pascau (Ref. 62) presented calculations of confined swirling flows using the Reynolds stress transport equations model and the k-ϵ turbulence model. Comparison of their predictions with the corresponding measurements of So et al. (Ref. 52) grants clear precedence to the transport equations model, which reasonably reproduced the major features of swirl.

In a recent study, Weber et al. (Ref. 54) presented computations for a number of isothermal swirling flow cases. The focus in their work was on two categories of swirling flows: high confinement flows in geometries representative of gas turbines, and low confinement flows encountered in industrial and experimental furnaces. In their study, they assessed three turbulence models: a Reynolds stress model, an Algebraic stress model, and a two-equation (k-ϵ) model. Comparisons between predictions and associated measurements showed that the two high-order closure models produce much improved predictions than the k-ϵ model.

It should be noted here that while the standard two-equation turbulence models have sometimes produced adequate comparative predictions, they are generally considered as insufficient for strongly swirling flows (Refs. 63 through 68). This is in part due to the isotropic nature of the eddy-viscosity formulation of the k-ϵ turbulence model, which is not valid for flows that are characterized by large-scale fluctuations, rotation, and strong streamline curvatures (Refs. 69 through 70). However, ad hoc modifications to the k-ϵ model have generally resulted in much improvement in predictions (Refs. 71 through 73), although only for very specific cases.

Closure

This survey has been provided to put the present work into context. The present study focuses on the fundamental

nonorthogonal grid coverage of an axisymmetric flow domain with irregular boundaries, and involves incorporating swirl and turbulence effects into a stream function-vorticity simulation.

CHAPTER III

MATHEMATICAL AND PHYSICAL MODEL

Introduction

This chapter is devoted to the presentation of the mathematical and physical model employed in the calculation of incompressible turbulent swirling flows. Presented here are the time-averaged PDEs (partial differential equations) that govern the conservation of mass and momentum, in terms of stream function and vorticity variables. The equations are given in axisymmetric cylindrical coordinates and time-dependent form.

A few comments on the mathematical treatment of turbulence are required here. The difficulties involved in calculating turbulent flows via solution of the full time-dependent form of the Navier-Stokes equations have long been known. Any numerical calculation procedure would require a prohibitively fine grid and excessively short time intervals in order to resolve the subtle details of turbulence. It is therefore necessary to solve the time-averaged equations, whereby the effect of turbulence manifests itself in the equations in the form of Reynolds stresses and turbulent fluxes, which involve time-averaged products of fluctuating

components. These terms are evaluated via a turbulence model.

The turbulence model employed here is a two-equation model based on the eddy-viscosity concept and known as the k-ϵ model (Ref. 55). It necessitates the solution of two PDEs for the transport of turbulence kinetic energy, k, and its rate of dissipation, ϵ. Knowledge of k and ϵ permits the length scale of turbulence to be calculated, and hence the eddy or turbulent viscosity from which the Reynolds stresses can be evaluated.

The Governing Equations

The stream function-vorticity approach used in the present work is one of the most popular methods for solving 2-D incompressible flow problems in bounded domains. The distinctly attractive feature of this approach is the computational decoupling of the kinematics and kinetics from the thermodynamics. Consequently, pressure determination is reduced to a post-processing operation involving solution of a linear PDE, often referred to as the Poisson equation for pressure. Conversely, the weakness of this approach is in the evaluation of vorticity at a no-slip wall. Numerical experiments have indeed confirmed that unimaginative handling of this constraint can destabilize the numerical solution.

In this approach, a change of variables is made which replaces the velocity components u and v with the stream

function, ψ, and vorticity, ω, using the relations:

$$ru = \partial\psi/\partial r \tag{3.1}$$

$$rv = -\partial\psi/\partial x \tag{3.2}$$

$$\omega = \partial v/\partial x - \partial u/\partial r \tag{3.3}$$

In this way, the continuity equation is automatically satisfied, and a time-dependent elliptic equation for the transport of vorticity can be obtained by combining the time-averaged axial and radial momentum equations, thereby eliminating pressure. An additional equation involving the new dependent variables ψ and ω can be obtained from the kinematic definition of vorticity given in Equation (3.3). This steady-state elliptic PDE is often referred to as the ψ-equation.

These two equations, together with the equations for the transport of tangential momentum, turbulence kinetic energy, and turbulence dissipation rate, constitute the complete set of PDEs (subject to appropriate boundary and initial conditions) necessary to solve for the time-mean flowfield variables at any location within the flow domain. Similarity between these equations and their diffusional relations allows them all to be cast into the common elliptic form:

$$b^{\varphi}\left[\frac{\partial}{\partial t}(\rho\varphi) + \frac{1}{r}\frac{\partial}{\partial x}\left(\rho\varphi\frac{\partial\psi}{\partial r}\right) - \frac{1}{r}\frac{\partial}{\partial r}\left(\rho\varphi\frac{\partial\psi}{\partial x}\right)\right] = \frac{1}{r}\left[\frac{\partial}{\partial x}\left(r\Gamma^{\varphi}\frac{\partial\varphi}{\partial x}\right) - \frac{\partial}{\partial r}\left(r\Gamma^{\varphi}\frac{\partial\varphi}{\partial r}\right)\right] + S^{\varphi} \tag{3.4}$$

where φ stands for any one of the time-averaged flowfield variables: ψ, ω, w, k, and ϵ, and the equations differ primarily in their source terms S^{φ}. Expressions for the coefficients b^{φ}, Γ^{φ}, and S^{φ} are given in Table I. The turbulence generation term, G_k, appearing in Table I, is defined as:

$$G_k/\mu_{eff} = 2\left[\left(\frac{\partial u}{\partial x}\right)^2 + \left(\frac{\partial v}{\partial r}\right)^2 + \left(\frac{v}{r}\right)^2\right] + \left(\frac{\partial u}{\partial r} + \frac{\partial v}{\partial x}\right)^2 + \left(\frac{\partial w}{\partial x}\right)^2 + \left[r\,\frac{\partial}{\partial r}\left(\frac{w}{r}\right)\right]^2 \qquad (3.5)$$

The Properties of Turbulence

The eddy viscosity approach to the modeling of turbulence is to relate the local turbulent viscosity, μ_t, to one or more properties of the turbulent flow. This viscosity is allowed to vary from one location to another, but at any point, it is assumed to be isotropic. It is evaluated from the local values of turbulence kinetic energy, k, and its rate of dissipation, ϵ, through the relation (Ref. 55):

$$\mu_t = C_\mu \rho k^2/\epsilon \qquad (3.6)$$

where C_μ is a turbulence constant given by Equation (3.9), and ρ is the density of the fluid.

The effective viscosity, represented by μ_{eff}, is defined as follows:

$$\mu_{eff} = \mu + \mu_t \qquad (3.7)$$

where μ is the laminar viscosity of the fluid and may be neglected for high Reynolds number flows.

A local length scale of turbulence, l, can be evaluated from the local values of k and ϵ according to the following relation (Ref. 55):

$$l = C_\mu k^{3/2}/\epsilon \tag{3.8}$$

Here l characterizes the macroscale of turbulence which is easier to estimate than either μ_t or ϵ. As a result, it is often prescribed as the boundary value from which near-wall specification of ϵ is obtained.

The recommended values for the constants of the k-ϵ turbulence model are as follows (Ref. 55):

$$C_\mu = 0.09 \tag{3.9}$$

$$C_1 = 1.44 \tag{3.10}$$

$$C_2 = 1.92 \tag{3.11}$$

$$\sigma_k = 1.0 \tag{3.12}$$

$$\sigma_\epsilon = 1.3 \tag{3.13}$$

Wall Functions and The Effect of Swirl

The two-equation (k-ϵ) turbulence model presented here is valid only for fully turbulent flows. However, while viscous effects on the energy-containing turbulent motions are negligible throughout most of the flow, the no-slip condition at a solid interface always ensures that, in the vicinity of a wall, viscous effects will be influential.

Although the thickness of this viscous-affected zone is usually two or more orders of magnitude smaller than the overall width of the flow, its effects extend over the whole flow field since, typically, fifty percent of the velocity change from the wall to the free stream occurs in this region.

Generally, there are two approaches for handling the wall-proximity regions in numerical methods for computing turbulent flows: the 'wall-function' approach and the low-Reynolds number modeling approach (Ref. 55). The former has several advantages: (a) it is more economical, (b) it allows the introduction of empirical information into the formulation, (c) it produces relatively accurate results with fewer grid points within the viscous sublayer compared with the low-Reynolds number approach, and (d) it requires evaluation of the wall effects only in the computational cells next to the wall. For these reasons, it was selected to utilize the 'wall function' approach in conjunction with the k-ϵ turbulence model of the present study.

The 'wall-function' method provides algebraic relations for near-wall grid points which must be located sufficiently far from the neighboring walls that they lie within the 'logarithmic' layer, where the viscous effects are entirely overwhelmed by the turbulent ones. Wall-function relations for a given variable relate its local value to the wall fluxes and/or the local values of other variables. These relations are derived in order to reproduce, identically,

the full implications of the logarithmic profiles. The assumption that uniform shear stress prevails in the region between the wall and its immediate nearby grid point is made on the basis that generation and dissipation of turbulence energy are locally in balance.

The variation of velocity in the fully turbulent region of the wall layer is correlated by the universal velocity profile (Ref. 55):

$$U^+ = (1/\kappa)\ \ln(EY^+) \tag{3.14}$$

where the dimensionless quantities U^+ and Y^+ are given by:

$$U^+ = U_P/U_\tau = U_P/(\tau_w/\rho)^{1/2} \tag{3.15}$$

$$Y^+ = \rho U_\tau Y_P/\mu = \rho(\tau_w/\rho)^{1/2}Y_p/\mu \tag{3.16}$$

In the above relations, U_P is the total time-averaged velocity parallel to the wall at the near-wall grid point P, U_τ is the friction velocity, τ_w is the uniform total wall shear stress in the direction of U_P, and Y_P is the positive normal distance from the wall to the point P, as shown in Figure 4. The Von Karman constant, κ, is assigned the value 0.42 while the constant E, which is a function of the wall roughness, is assigned the value 9.0 for a smooth wall.

In the uniform near-wall shear layer, the generation and dissipation of turbulence energy are in balance, and so U_τ and Y^+ are related to the local values of k by solving the k-transport equation with the convection and diffusion terms omitted, resulting in:

$$U_\tau = C_\mu^{1/4} k_P^{1/2} \tag{3.17}$$

$$Y^+ = \rho Y_P C_\mu^{1/4} k_P^{1/2} / \mu \tag{3.18}$$

Substitution of Equations (3.17) and (3.18) into Equation (3.14) yields the necessary wall function for the resultant wall shear stress, which is given by:

$$\tau_w = -U_P \kappa \rho C_\mu^{1/4} k_P^{1/2} / \ln(E Y_P \rho C_\mu^{1/4} k_P^{1/2} / \mu) \tag{3.19}$$

where the negative sign is inserted since τ_w and U_P must have opposite signs.

Horizontal Wall

The total tangential velocity near a horizontal wall is given by:

$$U_P = (u_P^2 + w_P^2)^{1/2} \tag{3.20}$$

while the resultant tangential wall shear stress, τ_w, and its component τ_{rx} are given by:

$$\tau_w = (\tau_{rx}^2 + \tau_{r\theta}^2)^{1/2} \tag{3.21}$$

$$\tau_{rx} = \mu_{eff}(\partial u/\partial r + \partial v/\partial x) \tag{3.22}$$

However, in the vicinity of a horizontal wall, $\partial v/\partial x$ approaches zero. Thus, τ_{rx} is the required wall function for $\mu_{eff}(\partial u/\partial r)$ obtained by multiplying τ_w by $\cos(\theta)$, where $\theta = \arctan(w_P/u_P)$; the result is:

$$\mu_{eff}(\partial u/\partial r) = -u_P \kappa \rho C_\mu^{1/4} k_P^{1/2} / \ln(E Y_P \rho C_\mu^{1/4} k_P^{1/2} / \mu) \tag{3.23}$$

Similarly, the wall function for $\mu_{eff}(\partial w/\partial r)$ is obtained by multiplying τ_w by $\sin(\theta)$, resulting in:

$$\mu_{eff}(\partial w/\partial r) = [-\kappa\rho C_\mu^{1/4}k_P^{1/2}/\ln(EY_P\rho C_\mu^{1/4}k_P^{1/2}/\mu) + \mu_{eff}/r]w_P \quad (3.24)$$

As $\partial v/\partial x$ approaches zero near a horizontal wall, the vorticity, ω, approaches $-\partial u/\partial r$. Hence, the required wall function for ω is obtained from Equation (3.23) as:

$$\mu_{eff}\omega_P = u_P\kappa\rho C_\mu^{1/4}k_P^{1/2}/\ln(EY_P\rho C_\mu^{1/4}k_P^{1/2}/\mu) \quad (3.25)$$

Equation (3.25) is used as the effective boundary condition for ω near a horizontal wall.

The turbulence generation term, G_k, can also be shown to reduce to:

$$G_k = 2\mu_{eff}\left[\left(\frac{\partial u}{\partial x}\right)^2 + \left(\frac{\partial v}{\partial r}\right)^2 + \left(\frac{v}{r}\right)^2\right] + \frac{\tau_w^2}{\mu_{eff}} + \mu_{eff}\left(\frac{\partial w}{\partial x}\right)^2 \quad (3.26)$$

Vertical Wall

Wall functions along a vertical wall are similarly formulated. The total tangential velocity is now:

$$U_P = (v_P^2 + w_P^2)^{1/2} \quad (3.27)$$

and the resultant tangential wall shear stress, τ_w, and its component τ_{xr} become:

$$\tau_w = (\tau_{xr}^2 + \tau_{x\theta}^2)^{1/2} \quad (3.28)$$

$$\tau_{xr} = \mu_{eff}(\partial u/\partial r + \partial v/\partial x) \quad (3.29)$$

However, $\partial u/\partial r$ approaches zero near a vertical wall. Hence, τ_{xr} is the required wall function for $\mu_{eff}(\partial v/\partial x)$, obtained by multiplying τ_w by $\cos(\theta)$, where $\theta = \arctan(w_P/v_P)$; the result is:

$$\mu_{eff}(\partial v/\partial x) = -v_P \kappa \rho C_\mu^{1/4} k_P^{1/2} / \ln(E Y_P \rho C_\mu^{1/4} k_P^{1/2}/\mu) \qquad (3.30)$$

Similarly, the wall function for $\mu_{eff}(\partial w/\partial x)$ is obtained by multiplying τ_w by $\sin(\theta)$, resulting in:

$$\mu_{eff}(\partial w/\partial x) = -w_P \kappa \rho C_\mu^{1/4} k_P^{1/2} / \ln(E Y_P \rho C_\mu^{1/4} k_P^{1/2}/\mu) \qquad (3.31)$$

Again, as $\partial u/\partial r$ approaches zero near a vertical wall, the vorticity, ω, approaches $\partial v/\partial x$. Hence, the required wall function for ω is obtained from Equation (3.30) as:

$$\mu_{eff}\omega_P = -v_P \kappa \rho C_\mu^{1/4} k_P^{1/2} / \ln(E Y_P \rho C_\mu^{1/4} k_P^{1/2}/\mu) \qquad (3.32)$$

This equation is used as the effective boundary condition for ω near a vertical wall.

The turbulence generation term, G_k, can also be shown to reduce to:

$$G_k = 2\mu_{eff}\left[\left(\frac{\partial u}{\partial x}\right)^2 + \left(\frac{\partial v}{\partial r}\right)^2 + \left(\frac{v}{r}\right)^2\right] + \frac{\tau_w^2}{\mu_{eff}} + \mu_{eff}\left(\frac{\partial w}{\partial r} - \frac{w}{r}\right)^2 \qquad (3.33)$$

Sloping Wall

Provision for wall inclination is included by taking into account the wall and flow angles in determining the resultant velocity, which is assumed to be parallel to the wall (Ref. 3); it is given by:

$$U_p = [(u_p^2 + v_p^2)\cos^2(\theta - \theta_o) + w_p^2]^{1/2} \qquad (3.34)$$

where the wall angle $\theta_o = \arctan(\partial Y/\partial x)$, and the flow angle $\theta = \arctan(v_p/u_p)$. The resultant wall shear stress can then be evaluated from Equation (3.19) using the above expression for U_p, and the turbulence generation term, G_k, reduces to:

$$G_k = 2\mu_{eff}\left[\left(\frac{\partial u}{\partial x}\right)^2 + \left(\frac{\partial v}{\partial r}\right)^2 + \left(\frac{v}{r}\right)^2\right] + \frac{\tau_w^2}{\mu_{eff}} \qquad (3.35)$$

Other Details

From the balance of generation and dissipation of turbulence kinetic energy, and with the assumption that the near-wall length scale varies linearly with the normal distance from the wall, it can be shown that:

$$\epsilon_p = C_\mu^{3/4} k_p^{3/2}/(\kappa Y_p) \qquad (3.36)$$

This equation is used to fix values of ϵ at near-wall grid points. As for the quantity k_p, it is evaluated from the regular k-transport equation with the assumption that the local rate of production of turbulence is balanced by the viscous dissipation rate.

The Pressure Recovery Equations

The purpose of introducing vorticity was to allow the time-mean pressure, P, to be eliminated from the equations. However, once the solution has been obtained, the pressure distribution may be recovered using one of several available approaches (Ref. 7). Here, the time-averaged equations for

the conservation of axial and radial momentum are rearranged into the form:

$$\frac{\partial P}{\partial x} = P_1(u,v,w,x,r) \tag{3.37}$$

$$\frac{\partial P}{\partial r} = P_2(u,v,w,x,r) \tag{3.38}$$

Then, a spatial-marching integration is propagated along the coordinate directions (using Equation (3.14) along the axial direction or Equation (3.15) along the radial direction) and continued until all desired values are obtained. It should be noted here that this approach requires prior knowledge of the pressure at one location only (typically at the inlet), and the integration is initiated using first-order forward differences followed by central-difference approximations once two values of P become available.

Closure

This chapter has presented the mathematical and physical model employed in the calculation of axisymmetric incompressible turbulent swirling flows. The time-averaged equations which govern the conservation of mass and momentum have been given in stream function-vorticity variable form. A two-equation (k-ϵ) turbulence model has been introduced which closes the system of equations. The model involves solution of two additional equations for the transport of turbulence kinetic energy, k, and its rate of dissipation, ϵ. Wall-functions have been described for the treatment of

near-wall regions, together with appropriate modifications to account for the effect of swirl and wall inclination. Finally, two PDEs for the recovery of pressure have been described.

CHAPTER IV

NUMERICAL SOLUTION PROCEDURE

Introduction

In Chapter 3, the PDEs (partial differential equations) which govern axisymmetric incompressible turbulent swirling flows were introduced. The primary task in this chapter is to derive a general solution procedure for these equations, so as to attain the local values of the flowfield variables at all positions within the flow domain.

The solution procedure is a finite difference one, in which the governing PDEs are replaced by a set of algebraic FDEs (finite difference equations) using upwind differences for the convection terms and centered differences for the diffusion terms. The relevant FDEs are derived at points of a general nonorthogonal mesh covering an irregular domain, using three different interpolation profiles.

The steady-state equation is solved using the Gauss-Siedel point iteration method with overrelaxation, and the time-dependent equations are solved via an explicit time-marching technique. Convergence and stability implications are discussed together with factors which may influence the overall accuracy and economy of the predictions.

The Grid System

Figure 2 illustrates a nonorthogonal mesh covering a typical domain in 2-D axisymmetric cylindrical coordinates (x,r), in which solution of the governing PDEs is sought. The 'vertical' gridlines (I = 1, 2, ...) are indeed vertical and nonuniformly spaced to cover the desired x-range, x_{max}. The 'horizontal' gridlines (J = 1, 2, ...) are skewed with respect to the x-axis, and the radial locations of the grid points are obtained at each x_i by dividing the specified vertical domain height, $r_{max,i}$, in some predetermined manner (perhaps uniformly, or gradually expanding or contracting). This is in essence an algebraic mesh generation technique, which is handled in a methodical way via the normalizing transformation relations:

$$\xi = x/x_{max} \tag{4.1}$$

$$\eta = r/r_{max,i} \tag{4.2}$$

where ξ and η are the normalized coordinates, which are easily obtainable for any given flow domain boundary.

The Finite Difference Equations

Preliminaries

Figure 3 illustrates a typical point P in the domain of integration together with the eight neighboring points (in compass notation) arrayed on a nonorthogonal grid in the x-r plane. Notice that all the small distances are available at

once from the x and r coordinates of the grid points. In particular, Δx_e and Δx_w represent horizontal distances from P to the next east and west vertical grid lines, and Δr_n and Δr_s represent vertical distances from P to its immediate north and south neighbors. The figure also displays the horizontal line (dashed) which locates the projected points E′ and W′ to the east and west of P, respectively.

If the grid lines through P were in fact horizontal, then E and W would coincide with E′ and W′ and the usual nonuniform rectangular grid FDE would result connecting the value of φ at P to its prevailing values at N, S, E, and W. However, in the case of the nonorthogonal grid of Figure 3, the following formula results:

$$a^{\varphi}_{P}\varphi_{P} = \Sigma\, a^{\varphi}_{j}\varphi_{j} + (S^{\varphi}_{P}\varphi_{P} + S^{\varphi}_{U}) \qquad (4.3)$$

where the sum is over N, S, E′ and W′, the a^{φ}_{j}'s are the so-called coupling coefficients, S^{φ}_{P} and S^{φ}_{U} are the linearized source term coefficients, and $a^{\varphi}_{P} = \Sigma\, a^{\varphi}_{j}$. Here, φ values at E′ and W′ must be known prior to using Equation (4.3) in an iterative solution scheme. Hence, it is required to assume a profile for the variation of φ with r, from which these values can be interpolated.

In the present work, consideration is given to three different interpolation profiles (Refs. 74 and 75):

1. Zeroth-order profile, where φ is assumed to have a uniform distribution with r over the east and west

surfaces of the integration cell, represented by its values at E and W, respectively.

2. First-order profile, where φ is assumed to have a linear variation with r over the east and west surfaces of the integration cell. This permits the value of φ at E′ to be expressed as a linear combination of its values at NE and E, or E and SE depending on the slope of gridline EP. Similarly, the value of φ at W′ can be expressed as a linear combination of its values at NW and W, or W and SW depending on the slope of gridline PW.
3. Second-order profile, where φ is assumed to have a quadratic variation with r over the east and west surfaces of the integration cell. This permits the value of φ at E′ to be expressed as a linear combination of its values at NE, E, and SE, and the value of φ at W′ to be expressed as a linear combination of its values at NW, W, and SW.

In this way, an FDE can be formulated connecting the value of φ at P directly to its values at the eight nearby points; the coupling coefficients remain geometry dependent and so can be found once and for all at the outset; and the FDE maintains its initial form and can be solved effectively using standard iterative techniques.

It is of course a simple matter to formulate a general FDE for the conservative form of the governing PDEs as given in Equation (3.4). However, for reasons which will become

apparent as we proceed, the formulation is carried out for the following variant of Equation (3.4):

$$b^{\varphi}\left[\frac{\partial}{\partial t}(\rho\varphi) + u\,\frac{\partial}{\partial x}(\rho\varphi) + v\,\frac{\partial}{\partial r}(\rho\varphi)\right]$$

$$= \frac{1}{r}\left[\frac{\partial}{\partial x}\left(r\Gamma^{\varphi}\frac{\partial\varphi}{\partial x}\right) - \frac{\partial}{\partial r}\left(r\Gamma^{\varphi}\frac{\partial\varphi}{\partial r}\right)\right] + S^{\varphi} \qquad (4.4)$$

This equation differs only in the way the convective terms are presented, and can be obtained by subtracting φ times the continuity equation from the left-hand-side of Equation (3.4).

The Interpolation Schemes

Figure 3 illustrates a typical point P in the domain of integration together with the eight neighboring points (in compass notation) arrayed on a nonorthogonal grid in the x-r plane. The values of φ at the projected points E′ and W′ may be expressed as linear combinations of values at nearby points through:

$$\varphi_{E'/W'} = \Sigma\, L^{(n)}{}_{j}\varphi_{j} \qquad (4.5)$$

where the sum is over NE, E, and SE for E′, and over NW, W, and SW for W′. The $L^{(n)}{}_{j}$′s are the nth-order fundamental Lagrange polynomials, also known as the cardinal functions for polynomial interpolation, which form a dual basis for the linear functionals of point evaluation. These are given by:

$$L^{(0)}_{NE} = 0 \tag{4.6}$$

$$L^{(0)}_{E} = 1 \tag{4.7}$$

$$L^{(0)}_{SE} = 0 \tag{4.8}$$

$$L^{(0)}_{NW} = 0 \tag{4.9}$$

$$L^{(0)}_{W} = 1 \tag{4.10}$$

$$L^{(0)}_{SW} = 0 \tag{4.11}$$

for the zeroth-order interpolation profile, or by:

if $r_P \geq r_E$, then

$$L^{(1)}_{NE} = (r_P - r_E)/(r_{NE} - r_E) \tag{4.12}$$

$$L^{(1)}_{E} = (r_P - r_{NE})/(r_E - r_{NE}) \tag{4.13}$$

$$L^{(1)}_{SE} = 0 \tag{4.14}$$

else if $r_P < r_E$, then

$$L^{(1)}_{NE} = 0 \tag{4.15}$$

$$L^{(1)}_{E} = (r_P - r_{SE})/(r_E - r_{SE}) \tag{4.16}$$

$$L^{(1)}_{SE} = (r_P - r_E)/(r_{SE} - r_E) \tag{4.17}$$

if $r_P \geq r_W$, then

$$L^{(1)}_{NW} = (r_P - r_W)/(r_{NW} - r_W) \tag{4.18}$$

$$L^{(1)}_{W} = (r_P - r_{NW})/(r_W - r_{NW}) \tag{4.19}$$

$$L^{(1)}_{SW} = 0 \tag{4.20}$$

else if $r_P < r_W$, then

$$L^{(1)}_{NW} = 0 \tag{4.21}$$

$$L^{(1)}_{W} = (r_P - r_{SW})/(r_W - r_{SW}) \tag{4.22}$$

$$L^{(1)}_{SW} = (r_P - r_W)/(r_{SW} - r_W) \tag{4.23}$$

for the first-order interpolation profile, or by:

$$L^{(2)}_{NE} = [(r_P - r_E)(r_P - r_{SE})]/[(r_{NE} - r_E)(r_{NE} - r_{SE})] \quad (4.24)$$

$$L^{(2)}_{E} = [(r_P - r_{NE})(r_P - r_{SE})]/[(r_E - r_{NE})(r_E - r_{SE})] \quad (4.25)$$

$$L^{(2)}_{SE} = [(r_P - r_{NE})(r_P - r_E)]/[(r_{SE} - r_{NE})(r_{SE} - r_E)] \quad (4.26)$$

$$L^{(2)}_{NW} = [(r_P - r_W)(r_P - r_{SW})]/[(r_{NW} - r_W)(r_{NW} - r_{SW})] \quad (4.27)$$

$$L^{(2)}_{W} = [(r_P - r_{NW})(r_P - r_{SW})]/[(r_W - r_{NW})(r_W - r_{SW})] \quad (4.28)$$

$$L^{(2)}_{SW} = [(r_P - r_{NW})(r_P - r_W)]/[(r_{SW} - r_{NW})(r_{SW} - r_W)] \quad (4.29)$$

for the second-order interpolation profile. Notice that both the linear and quadratic functions would reduce to their expected values of zero and unity should the grid distribution be rectangular indeed.

The Convection Terms

These are evaluated using the upwind differencing scheme, giving:

$$u\frac{\partial\varphi}{\partial x} = |u_P|\left[\frac{\varphi_P}{\beta_e\Delta x_e+\beta_w\Delta x_w} - \frac{\beta_e\varphi_{E'}}{\Delta x_e} - \frac{\beta_w\varphi_{W'}}{\Delta x_w}\right] \quad (4.30)$$

$$v\frac{\partial\varphi}{\partial v} = |v_P|\left[\frac{\varphi_P}{\beta_n\Delta r_n+\beta_s\Delta r_s} - \frac{\beta_n\varphi_N}{\Delta r_n} - \frac{\beta_s\varphi_S}{\Delta r_s}\right] \quad (4.31)$$

The values of the coefficients β_e, β_w, β_n, and β_s are related to the directions of the velocities at point P according to:

$$u_P > 0: \quad \beta_e = 0, \ \beta_w = 1 \quad (4.32)$$

$$u_P < 0: \quad \beta_e = 1, \ \beta_w = 0 \quad (4.33)$$

$$v_P > 0: \quad \beta_n = 0, \ \beta_s = 1 \quad (4.34)$$

$$v_P < 0: \quad \beta_n = 1, \ \beta_s = 0 \quad (4.35)$$

Using the interpolation functions given in Equations (4.6) trough (4.29), the net convective contributions to the overall coupling coefficients become:

$$C_{NE} = \beta_e L^{(n)}_{NE} |u_P| / \Delta x_e \tag{4.36}$$

$$C_E = \beta_e L^{(n)}_E |u_P| / \Delta x_e \tag{4.37}$$

$$C_{SE} = \beta_e L^{(n)}_{SE} |u_P| / \Delta x_e \tag{4.38}$$

$$C_{NW} = \beta_w L^{(n)}_{NW} |u_P| / \Delta x_w \tag{4.39}$$

$$C_W = \beta_w L^{(n)}_W |u_P| / \Delta x_w \tag{4.40}$$

$$C_{SW} = \beta_w L^{(n)}_{SW} |u_P| / \Delta x_w \tag{4.41}$$

$$C_N = \beta_n |v_P| / \Delta r_n \tag{4.42}$$

$$C_S = \beta_s |v_P| / \Delta r_s \tag{4.43}$$

$$C_P = C_E / L^{(n)}_E + C_W / L^{(n)}_W + C_N + C_S \tag{4.44}$$

The Diffusion terms

These are evaluated in the usual central difference fashion, giving:

$$\frac{1}{r}\frac{\partial}{\partial x}\left(r\Gamma^{\varphi}\frac{\partial \varphi}{\partial x}\right) = \left(\frac{2r_P}{r_P \Delta x_e \Delta x_P}\right)\left(\frac{\Gamma^{\varphi}_{E'}+\Gamma^{\varphi}_P}{2}\right)\varphi_{E'} + \left(\frac{2r_P}{r_P \Delta x_w \Delta x_P}\right)\left(\frac{\Gamma^{\varphi}_{W'}+\Gamma^{\varphi}_P}{2}\right)\varphi_{W'}$$
$$+ \left[\left(\frac{2r_P}{r_P \Delta x_e \Delta x_P}\right)\left(\frac{\Gamma^{\varphi}_{E'}+\Gamma^{\varphi}_P}{2}\right) + \left(\frac{2r_P}{r_P \Delta x_w \Delta x_P}\right)\left(\frac{\Gamma^{\varphi}_{W'}+\Gamma^{\varphi}_P}{2}\right)\right]\varphi_P \tag{4.45}$$

$$\frac{1}{r}\frac{\partial}{\partial r}\left(r\Gamma^{\varphi}\frac{\partial \varphi}{\partial r}\right) = \left(\frac{r_N+r_P}{r_P \Delta r_n \Delta r_P}\right)\left(\frac{\Gamma^{\varphi}_N+\Gamma^{\varphi}_P}{2}\right)\varphi_N + \left(\frac{r_S+r_P}{r_P \Delta r_s \Delta r_P}\right)\left(\frac{\Gamma^{\varphi}_S+\Gamma^{\varphi}_P}{2}\right)\varphi_S$$
$$+ \left[\left(\frac{r_N+r_P}{r_P \Delta r_n \Delta r_P}\right)\left(\frac{\Gamma^{\varphi}_N+\Gamma^{\varphi}_P}{2}\right) + \left(\frac{r_S+r_P}{r_P \Delta r_s \Delta r_P}\right)\left(\frac{\Gamma^{\varphi}_S+\Gamma^{\varphi}_P}{2}\right)\right]\varphi_P \tag{4.46}$$

Using the interpolation functions given in Equations (4.6) trough (4.29), the net diffusive contributions to the overall coupling coefficients become:

$$D_{NE} = \left(\frac{2r_P}{r_P\Delta x_e\Delta x_P}\right)\left(\frac{\Gamma^{\varphi}_{E'}+\Gamma^{\varphi}_{P}}{2}\right) L^{(n)}_{NE} \tag{4.47}$$

$$D_{E} = \left(\frac{2r_P}{r_P\Delta x_e\Delta x_P}\right)\left(\frac{\Gamma^{\varphi}_{E'}+\Gamma^{\varphi}_{P}}{2}\right) L^{(n)}_{E} \tag{4.48}$$

$$D_{SE} = \left(\frac{2r_P}{r_P\Delta x_e\Delta x_P}\right)\left(\frac{\Gamma^{\varphi}_{E'}+\Gamma^{\varphi}_{P}}{2}\right) L^{(n)}_{SE} \tag{4.49}$$

$$D_{NW} = \left(\frac{2r_P}{r_P\Delta x_w\Delta x_P}\right)\left(\frac{\Gamma^{\varphi}_{W'}+\Gamma^{\varphi}_{P}}{2}\right) L^{(n)}_{NW} \tag{4.50}$$

$$D_{W} = \left(\frac{2r_P}{r_P\Delta x_w\Delta x_P}\right)\left(\frac{\Gamma^{\varphi}_{W'}+\Gamma^{\varphi}_{P}}{2}\right) L^{(n)}_{W} \tag{4.51}$$

$$D_{SW} = \left(\frac{2r_P}{r_P\Delta x_w\Delta x_P}\right)\left(\frac{\Gamma^{\varphi}_{W'}+\Gamma^{\varphi}_{P}}{2}\right) L^{(n)}_{SW} \tag{4.52}$$

$$D_{N} = \left(\frac{r_N+r_P}{r_P\Delta r_n\Delta r_P}\right)\left(\frac{\Gamma^{\varphi}_{N}+\Gamma^{\varphi}_{P}}{2}\right) \tag{4.53}$$

$$D_{S} = \left(\frac{r_S+r_P}{r_P\Delta r_s\Delta r_P}\right)\left(\frac{\Gamma^{\varphi}_{S}+\Gamma^{\varphi}_{P}}{2}\right) \tag{4.54}$$

$$D_P = D_E/L^{(n)}_E + D_W/L^{(n)}_W + D_N + D_S \tag{4.55}$$

The Source Terms

These are handled via the source term linearization technique, giving:

$$S^{\varphi} = S^{\varphi}_P\varphi_P + S^{\varphi}_U \tag{4.56}$$

The specific expressions for S^{φ} are given in Table I, and expressions for S^{φ}_P and S^{φ}_U are decided according to the stability criterion presented in the following section.

The Time-Dependent FDE

Amalgamation of the expressions for the convective, diffusive, and source terms, together with an explicit time-dependent term, yields the following FDE for ω, w, k, and ϵ:

$$\rho(\varphi_P' - \varphi_P)/\Delta t = \Sigma(\rho C_j + D_j)\varphi_j - (\rho C_P + D_P)\varphi_P + (S^{\varphi}_P\varphi_P + S^{\varphi}_U) \quad (4.57)$$

where the sum is over all eight neighboring points, and the prime indicates values at the new time level, t + Δt. If the second bracketed term on the right-hand-side of Equation (4.57) is denoted by $R_P\rho/\Delta t$, then the following formula results:

$$\varphi_P' = \varphi_P + R_P(\varphi_{P,o} - \varphi_P) + \Delta t(S^{\varphi}_P\varphi_P + S^{\varphi}_U)/\rho \quad (4.58)$$

where $\varphi_{P,o}$ is the steady state expression for φ, obtained from Equation (4.57) by omitting both the time-derivative and the source term. In this way, it is readily seen that values of R_P less than or equal to unity form a sufficient condition for stability provided that the source terms are carefully handled.

The approach adopted here to guarantee this condition involves calculating a new Δt at each time step, such that $R_{P,max}$, which is invariably positive, is kept smaller than or equal to unity, and any opposing effect resulting from a negative source term is nullified by treating it implicitly. Following these guidelines, the update formula can be cast into its final form:

$$\varphi_P' = [\varphi_P + R_P(\varphi_{P,o} - \varphi_P) + \Delta t S^{\varphi}_U/\rho]/[1 - \Delta t S^{\varphi}_P/\rho] \quad (4.59)$$

where S^{φ}_P is allowed to have only negative coefficients. Notice that Equation (4.59) offers the added advantage of being easily adaptable to a vectorized solution technique

(Jacobi-type iterations) should the computations be carried out on a parallel-processing computer.

The Steady-State FDE

According to Equation (4.4) and Table I, the FDE for ψ is a specific case of Equation (4.57), in which the time-derivative and the convective terms are set to zero and the diffusion coefficient, Γ^{φ}, is set to unity. This results in the following FDE:

$$D_P\psi_P = \Sigma\ D_j\psi_j + [S^{\psi}_P\psi_P + S^{\psi}_U] \qquad (4.60)$$

where the sum is over all eight neighboring points. This equation can be effectively solved using standard iterative techniques. However, a certain degree of overrelaxation may be employed in order to promote convergence rates. This can be handled directly via:

$$\psi_P = (1 - f)\ \psi_P + f\ \Sigma\ [D_j/D_P]\psi_j + f\ [S^{\psi}_P\psi_P + S^{\psi}_U]/D_P \qquad (4.61)$$

where f is the overrelaxation factor normally taken between 1 and 2. In the present work, a value of 1.5 seemed to be appropriate for all the cases investigated. However, this is not necessarily the optimal value, which can only be determined by exploratory computations.

Boundary and Initial Conditions

Before the mathematical problem can be regarded as complete, it is necessary to provide additional relations

which embody the boundary conditions of the problem. Since the governing PDEs are elliptic, their solution is a strong function of the boundary conditions and utilization of the correct values is, therefore, crucial in order to mimic the experimental flowfield correctly.

Boundary conditions are generally classified according to whether the value of a variable (Dirichlet boundary) or the value of its gradient (Neumann boundary) is prescribed.

Inflow Boundary

At the inlet, the distributions of mean velocities and the turbulence quantities are stipulated to correspond to experimental data whenever possible. The stream function and vorticity profiles are then deduced from the specified velocity distribution using Equations (3.1) through (3.3).

In the absence of data pertaining to inlet turbulence quantities, the turbulence intensity is specified as some fraction of the axial velocity and the dissipation rate is estimated using the standard length scale assumption of 3 percent of the inlet diameter.

Axis of Symmetry

At the centerline, the time-mean radial and tangential velocities, the stream function, and the vorticity are set to zero whereas the gradient of all other variables is set to zero. An exception to this has been proposed by Lilley (Ref. 63), in which the swirl velocity is given an implied

zero value assuming that solid-body rotation is operative at the centerline. The near-centerline node is then assigned a value by linear interpolation between its north neighbor and the centerline zero value.

Outflow Boundary

In most cases, there is a lack of information about the distribution of the flowfield variables along this boundary. Here, the axial gradient of the stream function is assigned a zero value (i.e., zero radial velocity) while the radial gradient is subject to continuity constraints. The other variables are assumed to be sufficiently smooth to allow outlet values to be determined by linear extrapolation from nodes immediately upstream.

No-Slip Wall

Along a no-slip boundary, the stream function is given a constant value while the three velocity components are set to zero. As for vorticity, it is estimated from a second-order approximation to Equation (4.4), with the assumption that gradients parallel to the wall are negligible compared to those in the normal direction.

These conditions are valid for laminar flow cases only. Turbulent flows require additional relations which provide linkages for the velocity components, the vorticity, and the turbulence parameters in the 'logarithmic' region near the

wall to their intrinsic wall values. A complete discussion concerning this issue has been presented in Chapter 3.

Initial Conditions

To be able to initiate the numerical computations, it is necessary to specify initial values for all the dependent variables concerned. During the course of this work, it has been found that any crude approximation can be made provided that it does not critically violate continuity and boundary conditions. However, initial values that are closer to the final solution would, of course, lead to faster convergence. Therefore, if a series of parametric calculations is to be carried out, it would be beneficial to use the solution of a previous calculation as the initial estimate for a new one.

The Calculation Sequence

At this point, the mathematical problem can be regarded as complete. It remains now to outline the general solution procedure.

1. Specify input parameters such as flow geometry, boundary conditions, mesh size, etc.
2. Calculate and store frequently used geometric coefficients.
3. Specify initial values for all the dependent variables at t = 0.

4. Calculate the coupling coefficients according to Equations (4.30) through (4.55). Note that these are identical for all five equations.
5. Determine new values of ω along the no-slip solid boundary.
6. Solve the vorticity transport equation for ω at each interior point at the new time level using Equation (4.59).
7. Iterate for new values of ψ at all interior points using Equation (4.61).
8. Solve the swirl equation for new values of w at each interior point at the new time level using Equation (4.59).
9. Solve the k and ϵ equations for new values of turbulence properties at each interior point at the new time level using Equation (4.59).
10. Calculate the velocity components u and v using Equations (3.1) and (3.2).
11. Calculate a new time-step, Δt, to satisfy the stability constraint.
12. Return to Step (4) and repeat the process until convergence is reached.

The calculation procedure has been embodied in a newly developed computer code, which has been employed in all the computations presented in this thesis. The computer code is a general and flexible one and can be easily applied to a wide range of practical flow problems.

Convergence and Accuracy

The time-marching solution procedure is said to have converged when the sum of the absolute residuals becomes smaller than a reference value. This value is chosen on the basis that the relative change in the value of the dependent variable φ between two successive steps at any point P does not exceed 0.01%. This has proven to be sufficient for all the cases considered here.

It should be further noted that while the uniform and linear interpolation schemes are both bounded, the quadratic scheme, which is presumably more accurate, involves negative coefficients that may or may not cause divergence problems. Therefore, the superiority of a certain scheme is a function of the given problem and can only be asserted by exploratory computations.

Closure

This chapter has presented the numerical solution procedure in which the governing PDEs have been replaced by a set of algebraic FDEs, using upwind differences for the convection terms and centered differences for the diffusion terms. The relevant FDEs have been derived at points of a nonorthogonal mesh covering an irregularly-shaped domain, using three different interpolation profiles. The solution technique involved a point Gauss-Siedel method with over-relaxation for the steady-state equation, and an explicit time-marching method for the time-dependent equations.

Convergence and stability implications have been discussed together with factors which may influence the accuracy and economy of the solution.

CHAPTER V

MODEL EVALUATION

Introduction

The purpose of this chapter is to assess the predictive capability of the computer model via comparison of predicted results with available experimental data for six data cases of varying degrees of complexity. Laminar cases are used to confirm numerical accuracy, and turbulent cases are examined to establish the workability of the solution procedure in complex flow situations.

The specific test cases were selected from the general literature on the basis of their completeness, availability of tabular results, accuracy of the instrumentation, and complexity of the enclosure geometry. A summary of the selected cases is provided in Table II, and a schematic illustration of the test chambers and inlet geometries is shown in Figure 5.

Preliminary Assessment

Prior to applying the computer model to practical flow situations, it is essential to make an impartial comparison (based on idealized test cases) between the newly developed grid technique and the conventional stair-step approach for

handling irregularly-shaped boundaries. For this purpose, consider the 2-D field problem shown in Figure 6, which is governed by Laplace's equation in both cartesian (x,y) and axisymmetric (x,r) coordinates. The exact solution is:

$$\varphi = \varphi_o \frac{\sin (y\pi/H)}{\sin (2L\pi/H)} \sinh [\pi(2L - x)/H] \qquad (6.1)$$

for cartesian coordinates, with boundary conditions $\varphi = 0$ on the north, south, and east boundaries and $\varphi = \varphi_o \sin (y\pi/H)$ on the west boundary; it is:

$$\varphi = \varphi_o \frac{\sinh [2.4048 (2L - x)/H]}{\sinh [2.4048 (2L)/H]} J_o [2.4048 r/H] \qquad (6.2)$$

for axisymmetric coordinates, with boundary conditions $\varphi = 0$ on the north and east boundaries, $\partial\varphi/\partial r = 0$ on the south axisymmetric boundary, and $\varphi = \varphi_o J_o (2.4048 r/H)$ on the west boundary, where J_o is the zeroth-order Bessel function of the first kind.

The test section for which predictions were made and compared with the analytic solution is shown in Figure 7. The newly introduced boundaries were given values according to Equations (6.1) and (6.2). Results were obtained for four different H/L values: 0.5, 1.0, 2.0, and 4.0; these correspond to top-wall angles of 14.0, 26.6, 45.0, and 63.4 degrees, respectively. Moreover, grid-size dependency was established by solving the relevant FDEs for each H/L value using three different mesh sizes: 11 x 6 (coarse), 21 x 11 (intermediate), and 31 x 16 (fine). Here, the first value

represents the number of I-gridlines while the second value represents the number of J-gridlines. The I-gridlines are spaced uniformly and, for each x, the grid spacing in the y-direction is also uniform.

The average absolute errors and error percentages are given in Tables III and IV, respectively, for the cartesian problem. As the grid size is refined, accuracy is expected to improve. This was the case with the quadratic scheme (one order of magnitude improvement), only slightly with the stair-step approach (a factor of two), but definitely not the case with the uniform and linear schemes.

The skewness attained by increasing the value of H/L is seen to reduce accuracy significantly with the uniform and linear schemes (a factor of 10 and 20, respectively). Only a factor of four is seen with the stair-step approach, but the quadratic scheme shows no such effect at all.

For a given skewness and a given grid density, the choice of methods may be compared. For example, for the 45 degree north boundary (H/L = 2) and the intermediate grid density (21 x 11), the quadratic scheme is better than the stair-step approach by a factor of 20 while it is better than the other schemes by about two orders of magnitude.

Tables V and VI show corresponding evidence for the accuracy of the interpolation methods for the axisymmetric problem. Again, the same trends as described with Tables III and IV are observed.

For a given set of I-gridlines, as more and more J-gridlines are used in a nonorthogonal manner, points E′ and W′ (see Figure 3) become outside the bounds of the compact nine-point computational cell. Thus, the 'interpolation' schemes are in fact forced to extrapolate. To study the trade-off between reduced truncation error (with finer mesh) and extrapolation required to obtain φ values at E′ and W′, a check was made with the number of J-gridlines increased for fixed H/L values.

The results are shown in Tables VII and VIII for the cartesian and axisymmetric problems. Notice that results only for the intermediate grid (with refined number of J-gridlines) of the quadratic scheme, and H/L values of 0.5 and 1.0 are given for ease of interpretation of the general trends. It is surprising that in general the error reduces and that the greater grid density more than offsets the greater extrapolation.

Test Case 1 (Bentz)

The Physical Flow

This test case corresponds to the hemodynamic flow in a stenotic region (see Figure 5a) studied by Bentz (Ref. 76). The stenosis is modelled by a bell-shaped constriction in a long circular tube, according to the following profile for the top-wall radius R as a function of axial position and initial tube diameter:

$$R(x)/D_o = 0.5 - 0.25 \exp[-16(x/D_o)^2] \qquad (6.3)$$

where D_o is the tube diameter far from the constriction and x is the axial distance from the narrowest cross-section in the tube. The test section has a length of 34 tube radii, with x/D_o ranging from -5 to 12. The constriction reduces the original tube area by a factor of four, with the major region of reduced area occupying the zone from x/D_o = -0.7 to 0.7.

LDV measurements of axial velocities were taken at several measuring stations upstream from, within, and downstream from the constriction, for values of Reynolds number (based on inlet mean flow velocity and diameter) ranging from 2 to 200.

The Computations

Because the upstream influence of the constriction by way of pressure is insignificant in this test case, it was sufficient to begin the computations at the axial location x/D_o = -2. The outflow boundary was located at x/D_o = 8. Fully-developed laminar tube flow (Hagen-Poiseuille) was assumed at the inlet, which is in good agreement with the measured data, and inlet conditions for ψ and ω were then deduced as described in Chapter 4.

Predictions have been made with the quadratic scheme for Reynolds numbers (based on inlet average velocity and diameter) of 2, 57, and 167, using a 51 x 16 coarse mesh and

a 101 x 31 fine mesh, with rectangular grid except in the region of constriction.

Comparisons of predicted axial velocity profiles (non-dimensionalized by the average inlet velocity) for the three Reynolds numbers in question, along with their corresponding measured data, are shown in Figures 8 through 11. The predictions are clearly mesh-size independent and display good agreement with the measured data as can be seen in Figures 9 through 11. The recirculation zone, the throat velocities, and the downstream development of the velocity profile (leading to a parabolic profile near the exit) are all predicted with reasonable accuracy.

Figure 8 shows a comparison of the predicted centerline velocities for the three Reynolds numbers considered. These conform reasonably well with their measured counterparts. Examination of these profiles reveals that at the narrowest cross-section ($x/D_o = 0$), the maximum velocity decreases as Reynolds number increases, which is indicative of flatter throat profiles at larger Reynolds numbers. Downstream from the throat ($x/D_o > 0$), it can be seen that the flow recovers very quickly for the lowest Reynolds number; however, this recovery is much slower for the two higher values indicating the presence of a near-wall recirculation zone.

Figures 9 through 11 show comparisons of predicted and measured radial profiles of the axial velocity at several axial locations. For $Re_D = 2$, Figure 9 reveals no regions of flow recirculation; however, the profiles at the axial

locations x/D_o = 0.2 and 0.325 indicate the presence of adverse pressure gradients near the tube wall, but are apparently too weak to reverse the flow.

For Re_D = 57 and 167, Figures 10 and 11 display reverse flow regions which extend a distance of about $0.1D_o$ from the tube wall. The predicted location of reattachment as a function of Reynolds number is presented in Figure 12, and comparisons with measured values were not possible due to the lack of sufficient experimental data.

Further exploratory computations revealed that the reverse flow region begins to develop as Reynolds number approaches 10. At Reynolds numbers larger than 50, the vorticity field becomes significantly altered; the peak values of boundary vorticity near the throat are seen to spread downstream and negative wall values begin to appear during the expansion indicating the presence of a reverse flow zone. As Reynolds number is progressively increased, the peak wall vorticity value and the separation point move slightly upstream from the throat while the reattachment point moves farther downstream.

Test Case 2 (Bornstein & Escudier)

The Physical Flow

This test case designates the laminar water experiment of Bornstein and Escudier (Ref. 42). Here, a single inlet stream flows through a radial inflow vane swirler with 32 adjustable guide vanes, into an expanded test chamber (see

Figure 5b). The inlet diameter is 0.04 m. The expansion chamber has a diameter of 0.055 m, and is 0.43 m long.

Inlet velocity profiles were not collected, and LDV measurements of axial and swirl velocities were taken at a selection of downstream measuring stations for an inlet Reynolds number of 612 and a swirl number of 0.337.

The Computations

Although the initiation of the calculation domain at the first downstream measuring station is feasible, it was felt that the lack of any experimental data concerning the radial velocities in this region of flowfield expansion, where gradients are evolving rapidly, might be detrimental to the predictions. Therefore, the calculation domain was bounded on the upstream end by the chamber expansion plane, and the inlet profiles were shaped from the measured axial and swirl velocities at the first measuring station.

Predicted axial and swirl velocity profiles (non-dimensionalized by the average inlet velocity), along with corresponding experimental data, are shown in Figures 13 through 15 for a 44 x 56 rectangular mesh.

Analysis of the experimental axial velocity profiles (see Figure 14) displays a very complex recirculation zone structure near the centerline. The reverse flow region is displaced from the symmetry axis, and adjoined by forward flow along the centerline.

Examination of the predicted axial velocity profiles (see Figures 13 and 14; solid lines) discloses the formation of a small central recirculation zone at the axial location $x/D_e = 0.5$. However, the measured data shows this zone to form at the axial location $x/D_e = 0.35$ in a much more abrupt manner than the computations can simulate. The predicted size and strength of this recirculation zone also display very poor agreement with their measured counterparts.

The experimental swirl velocities display a double hump near the outside edge of the recirculation zone as can be seen in Figure 15. The corresponding predicted profiles (see Figure 15; solid lines) are unable to simulate this behavior and their peaks are substantially larger in magnitude over most of the recirculation zone.

In an effort to understand this lack of agreement, a parallel prediction was made with a 65 x 83 fine mesh. The results (not shown) were very similar to those of the 44 x 56 mesh, which seems to indicate that the predictions are independent of the grid size.

This leaves boundary conditions as one of few remaining possible sources of error which should be further examined. To accomplish this, predictions were made using different wall vorticity formulas and different inlet profiles. While changes to wall vorticity calculations failed to produce any meaningful improvements, the predictions displayed a large sensitivity to variations in the inlet profiles as can be seen in Figures 13 through 15.

This case has been also predicted by Sloan (Ref. 61) using primitive-variable formulation. His predictions are qualitatively very similar to the present ones. The large disparity between the calculations and measurements may be attributed to the lack of adequate inlet profiles.

Test Case 3 (Deshpande & Giddens)

The Physical Flow

This case refers to the turbulent flow occurring in a modelled arterial stenosis (see Figure 5a) investigated by Deshpande and Giddens (Ref. 77). The stenosis is modelled by a bell-shaped constriction in a long circular tube. The constriction is described by the following equation for the top-wall radius R as a function of axial position and initial tube radius:

$$R(x)/D_o = 0.5 - 0.125\ [1 + \cos(z\pi/2)] \qquad (6.4)$$

where D_o is the tube diameter far from the constriction and x is the axial distance from the narrowest cross-section in the tube. The test section has a length of 15 tube radii, with x/D_o ranging from -2 to 5.5. The constriction reduces the original tube area by a factor of four, with the major region of reduced area occupying the zone from x/D_o = -1 to 1.

LDV measurements of time-mean axial velocities and RMS turbulence velocities were collected at several measuring stations upstream from, within, and downstream from the

constriction, for values of Reynolds number (based on the mean flow velocity and diameter at the inlet) ranging from 5000 to 15000.

The Computations

The calculation domain was taken to be 6 tube diameters in length, with x/D_o ranging from -2 to 4. Inlet velocities were shaped from the measured time-mean profile at the axial location $x/D_o = -2$, which matches the fully developed power-law profile. Inlet turbulence intensities were also shaped from measured RMS velocities while the characteristic length scale of turbulence (needed for estimation of inlet energy dissipation rates) was taken to be 3 percent of the inlet diameter.

Predictions have been made with the quadratic scheme for a Reynolds number of 15000 (based on the inlet average velocity and diameter) using a 91 x 31 mesh, with uniform rectangular grid except in the region of reduced area.

Comparisons of predicted time-mean axial velocity profiles (non-dimensionalized by the bulk inlet velocity), along with their corresponding measured data, are shown in Figures 16 and 17.

Figure 16 shows the variation of centerline velocity with the axial distance x/D_o. The maximum deviation from the measured profile is seen to occur at $x/D_o = 0$, with an overprediction of about 8 percent.

Considering Figure 17, the predicted time-mean axial velocity profile at the entrance plane to the constriction ($x/D_o = -1$) is very close to that at $x/D_o = -2$, as indicated by the measured data as well. A brisk acceleration in the converging section is demonstrated by the results for $x/D_o = -0.5$, and a rather blunt (plug-like) profile is seen at the throat. Interestingly, the measured maximum throat velocity does not occur at the centerline but occurs near the wall. This is not the case with the predictions.

Flow recirculation is distinctly apparent in the profiles from $x/D_o = 0.5$ to 2, with predicted negative velocities as high as 40 percent of the average inlet velocity, corresponding to measured values of about 50 percent.

Figure 18 shows the location of flow reattachment as a function of Reynolds number. The predicted value for the Reynolds number in question is $x/D_o = 2.15$, corresponding to a measured value of about 2.2. It can also be seen from the Figure that this value is independent of Reynolds number in the range of 5000 to 15000. Finally, examination of the downstream profiles reflects a gradual return toward the upstream conditions.

Test Case 4 (Yoon & Lilley)

The Physical Flow

This test case refers to the work of Yoon and Lilley (Ref. 47). A single air stream enters the test section

through a secondary annulus, passing through an adjustable vane swirler en route (see Figure 5c). The swirl generator is reminiscent of a propeller, with the central hub (0.0373 m diameter) functioning as a blocked-off primary tube. The exit plane of the swirler is positioned 0.032 m upstream of the 90 degree expansion block. The 0.1492 m inside-diameter secondary annulus expands into a 1.5 m long test chamber, whose inside diameter is 0.2984 m.

Five-hole pitot probe measurements of time-mean axial, radial, and swirl velocities were taken at the start of the expansion and at several downstream measuring stations. The measurements were taken for five different vane angles of 0, 38, 45, 60, and 70 degrees (0 degree vane angle refers to a non-swirling flow case with the swirl generator and central hub removed). The corresponding average inlet velocities are 15.7, 10.5, 12.6, 8.84, and 5.57 m/s, respectively.

The Computations

In this test case, the non-swirling flow study was considered, and is presented as a preface to the succeeding case. The swirl generator and central hub were removed, providing an essentially uniform axial velocity profile at the inlet. The inlet turbulence intensity was taken to be 4 percent of the average velocity, whereas the characteristic length scale of turbulence (needed for estimation of energy dissipation rates) was taken to be 3 percent of the chamber diameter.

Predictions have been made using a 46 x 31 mesh with uniform rectangular grid. Comparisons of predicted time-mean axial velocities (non-dimensionalized by the average inlet velocity), along with corresponding measured data, are shown in Figure 19.

The predicted axial velocities follow the experimental trends very closely. However, they fail to match the data points precisely because the integrated experimental mass flow rates vary by as much as 25 percent from the value at the inlet.

The predicted corner recirculation zone extends to the axial location $x/D_e = 2.125$ (a distance of 8.5 step sizes), with a maximum width of $0.19D_e$ occurring near the expansion plane. The measured recirculation zone extends to just beyond $x/D_e = 2.0$, with a maximum width of $0.17D_e$ occurring near the inlet as well. The predicted maximum reverse flow velocity is approximately 20 percent of the average inlet velocity, corresponding to a measured value of about 16 percent. This case has been also predicted by Abujelala and Lilley (Ref. 78), and Sloan (Ref. 61) using a primitive-variable code. Their computations are qualitatively very similar to the present ones.

Test Case 5 (Yoon & Lilley)

The Physical Flow

This case refers to the swirling flow system studied by Yoon and Lilley (Ref. 47), which is an extension of case 4.

Here, the air stream enters the expansion chamber through a secondary annulus, passing through a 38 degree vane angle swirler en route. The flow conditions and rig geometry are as described in case 4 and Figure 5c.

The Computations

The calculations were initiated at the expansion plane with inlet velocity profiles shaped from the measured data. The inlet turbulence intensity was taken to be 12 percent of the average inlet velocity, and the characteristic length scale of turbulence was taken to be 3 percent of the chamber diameter.

Predicted time-mean axial and swirl velocities (non-dimensionalized by the average inlet velocity), along with corresponding experimental data, are shown in Figures 20 through 22, for a 46 x 31 rectangular grid.

Examination of Figures 20 shows a reasonable agreement between the measured and predicted velocities along the axis of symmetry. However, the calculations demonstrate that the axial velocity recovers and progresses to uniformity at a much faster rate than that displayed by the measurements.

It is apparent from Figure 21 that the predictions also fail to reproduce the size and strength of the experimental recirculation zone. The experimental profiles maintain the recirculation zone farther downstream, and are skewed toward the wall relative to the predictions. The predictions decay to uniform axial velocity profiles, whereas the experimental

recirculation zone remains tangible even at the farthest downstream location. Figure 22 displays that the predicted swirl velocity also decays to a forced vortex (solid-body rotation) profile, whereas the experimental data maintain a combined vortex distribution.

In an effort to explain the lack of agreement between the predictions and measurements, the following issues were further examined: (a) effect of choice of inlet conditions on the predictions, (b) effect of choice of parameters in the k-ϵ turbulence model and its accuracy in swirling flows, and (c) correctness of the implementation of the swirl equation.

Recalling the predictions of case 2, it is apparent from Figures 13 through 15 that any slight variation in inlet conditions would have a significant influence on the resultant flowfield. For example, Figure 13 demonstrates the effect of varying the inlet swirl and axial velocities on the formation of the recirculation zone; and Figure 14 shows the effect of inlet swirl velocity on the downstream axial velocity profiles. It is clear that the recirculation zone, which is present in the cases of uniform swirl and combined vortex, is replaced by a forward flow region with axial velocities that match their peak values at each cross-section. The radial location of the maximum axial velocity is also shown to be a strong function of the inlet swirl profile.

As for the effect of choice of parameters in the k-ϵ turbulence and its accuracy in swirling flows, studies by other researchers, see for example Sloan (Ref. 61) and Abujelala and Lilley (Ref. 72), illustrate how k-ϵ model modifications have been utilized to effect more accurate predictions. Some of the inaccuracies in eddy-viscosity models, such as the k-ϵ model, arise from the assumption of isotropy, and swirling flows are highly anisotropic as has been confirmed experimentally, see for example Owen (Ref. 43).

Correctness of the implementation of the swirl equation was examined through a comparative study between the present predictions, previous predictions by Sloan (Ref. 61), and the experimental data. Tables IX and X give a summary of the rate of decay of maximum axial and swirl velocities, respectively. The predictions are qualitatively similar, and manifest a similar lack of agreement with the measured data. However, the measured data exhibit inconsistencies in mass flow rates (up to 50 percent error in cross-section calculations downstream versus at the inlet) and axial flux of angular momentum (up to 20 percent error). This may have been due to poor probe sensitivity in turbulent flow, and nonaxisymmetry of the flow. Additionally, these prediction studies suffer from inadequacies in the turbulence models used.

Test Case 6 (Weber et al.)

The Physical Flow

This test case refers to the highly confined swirling flow system studied by Weber et al. (Ref. 54). The flow configuration consists of a solid-body vortex generator, a 20 degree angle burner quarl, and a cylindrical furnace (see Figure 5d). The honeycomb swirl generator and the geometry of the rig were designed in such a way that the air flow had negligible radial velocity downstream from the generator. The furnace diameter D_f is 0.44 m, and is 2.5 m long. The confinement ratio D_f/A is 2.3, the quarl expansion ratio B/A is 2.0, and the furnace to quarl outlet diameter ratio D_f/B is 1.15. The axial locations of the entrance and exit of the quarl are $x/D_f = 0.341$ and $x/D_f = 0.938$, respectively.

The average inlet velocity is 4.8 m/s, and the inlet vortex of low turbulence (1%) has a solid-body rotation and its swirl number is 0.75. LDV measurements of time-mean axial and tangential velocities, together with their normal stresses, were taken at the inlet to the quarl and at many downstream measuring stations.

The Computations

The calculations were initiated at the entrance to the quarl ($x/D_f = 0.341$), which coincides with the location of the first measuring station, and terminated at $x/D_f = 5.0$. The inlet velocity profiles and turbulence intensities were

shaped from the measured data, whereas the characteristic length scale of turbulence was assumed to be 10 percent of the inlet diameter.

Predicted time-mean axial and swirl velocities (non-dimensionalized by the average inlet velocity), along with corresponding experimental data, are shown in Figures 23 through 25, for a 91 x 24 mesh and quadratic interpolation.

A comparison of the predicted and measured centerline velocity is shown in Figure 23. Again, as with case 5, the predicted recovery of the axial velocity occurs at a much faster rate than that displayed by the measurements. Thus, the size and strength of the central recirculation zone are underpredicted.

Considering the axial velocity profiles of Figure 24, it can be seen that the first stagnation point is properly predicted. However, at the quarl exit, the predicted radial displacement of the zero streamline is roughly 50 percent of the measured value. Hence, the rate with which the vortex loses its energy is too high and, consequently, the position of maximum reverse flow is predicted inside the quarl rather than in the furnace. The calculated maximum reverse flow velocity is 25 percent of the average inlet velocity. This corresponds to a measured value of about 44 percent, which is skewed toward the wall relative to the predictions.

As for the swirl velocity distribution, Figure 25 displays how the inlet forced-vortex is transformed into a combined-vortex near the axial location $x/D_f = 1.7$. It is

also apparent here that the surplus of tangential momentum near the centerline in the quarl results in negative axial velocities that are larger in magnitude than their measured counterparts.

This test case has been also predicted by Weber et al. (Ref. 54) using primitive-variable formulation and different turbulence models. Their predictions with the k-ϵ model are qualitatively very similar to the present ones and manifest a similar lack of agreement with the measurements, which may be attributed to poor k-ϵ turbulence model performance.

Closure

This chapter has presented an extensive evaluation of the numerical solution procedure. Computations made for a 2-D field problem confirmed the superiority of the quadratic interpolation scheme over the standard stair-step approach. Predictions of laminar and turbulent recirculating flows were found to be in reasonable agreement with corresponding measurements. However, predictions of turbulent swirling flows displayed a rapid decay (relative to the measurements) of the swirl velocity toward solid-body rotation, and failed to capture the experimental size and strength of the central recirculation zone.

CHAPTER VI

CONCLUDING REMARKS

Summary and Conclusions

Prior to case description and analysis, a review was provided of numerical methods in fluids and heat transfer, and experimental and theoretical investigations of elliptic swirling flows, in which the effects of incremental changes in swirl strength, flow rates, and confinement geometries were analyzed. To a large extent, existing computational methods are capable of qualitatively capturing the expected trends and characteristics. However, many of these methods require prohibitively fine grids in order to satisfactorily represent irregularly-shaped boundaries. As a Consequence, their application is limited to simple flow geometries. It was, therefore, the purpose of the present computer modeling effort to develop and evaluate a new differencing technique, which resolves the fundamental problem of irregular boundary representation, and leads to accurate results on moderate grids.

A summary of the main achievements of the present study and the conclusions thereof are presented in the following tabulation.

1. A boundary-fitted nonorthogonal grid technique has been developed and successfully applied to a stream function-vorticity simulation of axisymmetric incompressible turbulent swirling flows.
2. The grid technique employs a compact nine-point computational cell, and is compatible with SOLA- and TEACH-type codes. The formulation has been presented for displaced, linear, and quadratic interpolation functions.
3. A vorticity wall function has been formulated for the treatment of turbulent near-wall flows.
4. Comparisons between predictions and analytic solutions of 2-D field problems demonstrated the superiority of the quadratic interpolation scheme over the displaced scheme, the linear scheme, and the standard stair-step approach.
5. Predictions of laminar and turbulent recirculating flows were found to be in reasonable agreement with available experimental data.
6. Reliable predictions of elliptic swirling flows were heavily dependent upon the availability of accurate and complete inlet conditions; computed results exhibited considerable sensitivity to the inlet profiles as well as the axial location at which the computations were initiated.
8. The performance of the k-ϵ turbulence model for swirling flows was generally poor in the vicinity

of the CTRZ. In the recovery region, it performed satisfactorily for the time-mean axial velocity; however, it displayed a rapid decay of the swirl velocity to a forced-vortex profile.

9. Convergence difficulties were encountered with the quadratic scheme when extrapolation resulted as a consequence of the grid arrangement. This problem was circumvented by generating the grid in a way such that interpolation is always guaranteed.
10. Flowfield predictions exhibited large sensitivity to the manner in which vorticity at a protruding corner was calculated. It was observed that when the stream-wise gradient of the stream function was used for its calculation, the computations failed to capture the corner recirculation zone. However, calculations based on the cross-stream gradient were found to resolve this problem and compare well with experimental data.

Recommendations for Future Work

The present investigation has disclosed some areas which warrant further research in order to enhance the predictive capabilities of the current computer model. These are presented in the tabulation below.

1. Since all of the data cases considered here are categorized as elliptic recirculating flows, which are characterized by large cross-stream gradients

and velocity-to-gridline angles, it is recommended to replace the upwind scheme with a transportive scheme which preserves the directional properties exhibited by the fluid transport phenomena. The SUDS (Skew Upwind Differencing Scheme) and QUDS (Quadratic Upstream Differencing Scheme) are two recommended candidates for initial evaluation. Both have been proven to be more accurate than the upwind scheme, and fit easily within the framework of the present grid technique.

2. More experimental measurements with swirl should be sought. In particular, more reliable inlet conditions are required for experiments to be of sufficient caliber for turbulence and swirl model evaluation.

3. The present study has demonstrated that the k-ϵ turbulence model does not adequately represent the structure of turbulence when applied to confined swirling flows. Prominent amongst its limitations are the poor prediction of the size and strength of the recirculation zone, and the inability to reproduce the observed combined free and forced vortex distributions. This may be partly due to the isotropic nature of the k-ϵ turbulence model. Higher-order closure models, in which the stress components are obtained directly from solution of their modelled partial differential equations,

have been recently reported to overcome some of these limitations. Thus, It is suggested that a higher-order turbulence model, such as the ASM or RSM, be considered for future implementation.

REFERENCES

1. Gupta, A.K., Lilley, D.G., and Syred, N., Swirl Flows. Abacus Press, Tunbridge Wells, England, 1985.

2. Gupta, A.K. and Lilley, D.G., Flowfield Modeling and Diagnostics. Abacus Press, Tunbridge Wells, England, 1985.

3. Khalil, E.E., Modeling of Furnaces and Combustors. Abacus Press, Tunbridge Wells, England, 1982.

4. Beer, J.M. and Chigier, N.A., Combustion Aerodynamics. Applied Science, London and Halsted-Wiley, New York, 1972.

5. Anderson, D.A., Tannehill, J.C., and Pletcher, R.H., Computational Fluid Mechanics and Heat Transfer. Hemisphere Publishing Corp. and McGraw-Hill Book Co., New York, 1984.

6. Patankar, S.V., Numerical Heat Transfer and Fluid Flow. Hemisphere Publishing Corp., London, 1980.

7. Gosman, A.D., Pun, W.M., Runchal, A.K., Spalding, D.B., and Wolfshtein, M.W., Heat and Mass Transfer in Recirculating Flows. Department of Mechanical Engineering, Imperial College of Science and Technology, London, 1968.

8. Roache, P.J., Computational Fluid Mechanics. Hermosa Publishers, Albuquerque, New Mexico, 1972.

9. Wong, H.H. and Raithby, G.D., "Improved Finite Difference Methods Based on a Critical Evaluation of the Approximation Errors." Numerical Heat Transfer, Vol. 2, 1979, pp. 139-163.

10. Varejao, L.M.C., "Flux-Spline Method for Heat, Mass, and Momentum Transfer." Ph.D. Thesis, Department of Mechanical Engineering, University of Minnesota, 1979.

11. Raithby, G.D., "Skew-Upwind Differencing Schemes for Problems Involving Fluid Flow." Comput. Meths. Appl. Mech. Eng., 9, 1976, pp. 153-164.

12. Leonard, B.P., "A Survey of Finite Differences With Upwinding for Numerical Modeling of Incompressible Convective Diffusion Equations." In Recent Advances in Numerical Methods in Fluids, Vol. 2, C. Taylor, ed., Pineridge Press, 1981.

13. Runchal, A.K., "CONDIF: A Modified Central-Difference Scheme for Convective Flows." International Journal for Numerical Methods in Engineering, Vol. 24, 1987, pp 1593-1608.

14. Karki, K.C., Patankar, S.V., Runchal, A.K., and Mongia, H.C., " Improved Numerical Methods for Turbulent Viscous Recirculating Flows; Aerothermal Modeling Program Phase II." NASA CR-182169, June 1988.

15. Syed, S.A. and Chiappetta, L.M., "Finite Difference Methods for Reducing Numerical Diffusion in TEACH-Type Calculations." AIAA Paper No. 85-0057, 1985.

16. Syed, S.A., Gosman, A.D., and Peric, M. "Assessment of Discretization Schemes to reduce Numerical Diffusion in the Calculation of Complex Flows." AIAA Paper No. 85-0441, 1985.

17. Gupta, M.M., "A Survey of Some Second-Order Difference Schemes for the Steady-State Convection Diffusion Equations." Int. J. Numer. Meths. Fluids, Vol. 3, 1983, pp.319-331.

18. Huang, P.G., Launder, B.E., and Leschziner, M.A., "Discretization of Nonlinear Convection Processes: A Broad Range Comparison of Four Schemes." Comput. Meths. Appl. Mech. Eng., 48, 1985, pp. 1-24.

19. Shyy, W. and Correa, M., "A Systematic Comparison of Several Numerical Schemes for Complex Flow Calculations." AIAA Paper No. 85-0440, 1985.

20. Castro, I.P. and Jones, J.M., "Studies in Numerical Computations of Recirculating Flows." Int. J. Numer. Meths. Fluids, Vol. 7, 1987, pp.793-823.

21. Patankar, S.V., Karki, K.C., and Mongia, H.C., "Development and Evaluation of Improved Numerical Schemes for Recirculating Flows." AIAA paper No. 87-0061, 1987.

22. Karki, K.C., Patankar, S.V., and Mongia, H.C., "Solution of Three-Dimensional Flow Problems a Using Flux-Spline Method." AIAA Paper No. 89-0687, 1989.

23. Karki, K.C., Patankar, S.V., and Mongia, H.C., "Fluid Flow Calculations Using a Multigrid Method and an Improved Discretization Scheme." AIAA Paper No. 89-0483, 1989.

24. Rhode, D.L. and Lilley, D.G. "Selection of Irregular-Boundary Transformation Method for Gas Turbine Combustor Flowfield Simulation." School of Mechanical and Aerospace Engineering, Oklahoma State University, Stillwater, OK, May 1980.

25. Ives, D.C. and Siddons, W.D., "Orthogonal Grid Generation." AIAA Paper No. 84-1248, 1984.

26. Syed, S.A. and Siddons, W.D., "Development of a Multi-Region Orthogonal Curvilinear CFD Code for Gas Turbine Combustors." AIAA Paper No. 86-1664, 1986.

27. Syed, S.A. and Shabayek, A.E., "Development and validation of a Curvilinear Code for Gas Turbine Combustors." AIAA Paper No. 86-0217, 1986.

28. Vanka, S.P., "Block Implicit Calculation of Steady Turbulent Recirculating Flows." International Journal of Heat and Mass Transfer, Vol. 28, 1985, pp. 2093-2103.

29. Braaten, M.E., "Development and Evaluation of Iterative and Direct Methods for the Solution of the Equations Governing Recirculating Flows." Ph.D. Thesis, Department of Mechanical Engineering, University of Minnesota, 1985.

30. Brandt, A., "Multi-Level Adaptive Solutions to Boundary-Value Problems." Mathematics of Computation, Vol. 31, 1977, pp. 333-390.

31. Vanka, S.P., "Block-Implicit Multigrid Calculation of Two-Dimensional Recirculating Flows." Comput. Meths. Appl. Mech. Eng., 59, 1986, pp. 29-48.

32. Vanka, S.P., "Block-Implicit Multigrid Solution of Navier-Stokes Equations in Primitive Variables." Journal of Computational Physics, Vol.65, 1986, pp.138-158.

33. Gaskel, P.H. and Wright, N.G., "An Improved Multigrid Strategy for the Investigation of Highly Recirculating Fluid Flows." Paper No. AIAA-3651-CP, First National Fluid Dynamics Congress, Cincinnati, 1988.

34. Baker, D.W., "Decay of Swirling Turbulent Flow of Incompressible Fluids in Long Pipes." Ph.D. Thesis, University of Maryland, 1967.

35. Murakami, M., Kito, O., Katayama, Y., and Iida, Y., "An Experimental Study of Swirling Flow in Pipes." Bulletin of the JSME, Vol. 19, No. 128, 1976, pp. 118-126.

36. Sarpkaya, T., "On Stationary and Traveling Vortex Breakdowns." Journal of Fluid Mechanics, Vol. 45, 1971, pp. 545-559.

37. Sarpkaya, T., "Vortex Breakdown in Swirling Conical Flows." AIAA Journal, Vol. 9, No. 9, 1971, pp. 1792-1799.

38. Faler, J.H. and Leibovich, S., "Disrupted States of Vortex Flow and Vortex Breakdown." The Physics of Fluids, Vol. 20, No. 9, 1977, pp. 1385-1400.

39. Faler, J.H. and Leibovich, S., "An experimental Map of the Internal Structure of a vortex Breakdown." Journal of Fluid Mechanics, Vol. 86, 1978, pp.313-335.

40. So, K.L., "Vortex Phenomena in a Conical Diffuser." AIAA Journal, Vol. 5, No. 6, 1967, pp. 1072-1078.

41. Garg, A.K. and Leibovich, S., "Spectral Characteristics of Vortex Breakdown Flowfields." Physics of Fluids, Vol. 22, No. 11, 1979, pp. 2053-2064.

42. Bornstein, J. and Escudier, M.P., "LDA Measurements Within a Vortex-Breakdown Bubble." International Symposium on Application of Laser-Doppler Anemometry to Fluid Mechanics, Paper 10.3, July 5-7, 1982, Lisbon, Portugal.

43. Owen, F.K., "Measurements and Observations of Turbulent Recirculating Jet Flows." AIAA Journal, Vol. 14, No. 11, 1976, pp. 1556-1562.

44. Habib, M.A. and Whitelaw, J.H., "Velocity Characteristics of a Confined Coaxial Jet." Journal of Fluids Engineering, Vol. 102, 1979, pp. 521-529.

45. Habib, M.A. and Whitelaw, J.H., "Velocity Characteristics of Confined Coaxial Jet With and Without Swirl." Journal of Fluids Engineering, Vol. 102, 1980, pp. 45-53.

46. Vu, B.T. and Gouldin, F.C., "Flow Measurements in a Model Swirl Combustor." AIAA Journal, Vol. 20, No. 5, 1982, pp. 642-651.

47. Yoon, H.K. and Lilley, D.G., "Five-Hole Pitot Probe Time Mean Velocity Measurements in Confined Swirling Flows." AIAA Paper No. 83-0313, 1983.

48. Roback, R. and Johnson, B.V., "Mass and Momentum Turbulent Transport Experiments With Confined Coaxial Jets." NASA CR-168252, August, 1983.

49. Johnson, B.V. and Roback, R., "Mass and Momentum Turbulent Transport Experiments With Swirling Confined Coaxial Jets; Part I." AIAA paper No. 84-1380, 1984.

50. Roback, R. and Johnson, B.V., "Mass and Momentum Turbulent Transport Experiments With Swirling Confined Coaxial Jets; Part II." AIAA paper No. 86-1665, 1986.

51. Ramos, J.I. and Sommer, H.T., "Swirling Flow in a Research Combustor." AIAA Journal, Vol. 23, No. 2, 1985, pp. 241-248.

52. So, R.M., Ahmed, S.A., and Mongia, H.C., "An Experimental Investigation of Gas Jets in Confined Swirling Air Flow." NASA CR-3832, 1984.

53. Sommer, H.T., "Swirling Flow in a Research Combustor." AIAA Paper No. 83-0313, 1983.

54. Weber, R., Visser, B.M., and Boysan, F., "Assessment of Turbulence Modeling for Engineering Prediction of Swirling Vortices in the Near Burner Zone." International Journal of Heat and Fluid Flow, Vol. 11, No. 3, 1990, pp. 225-235.

55. Launder, B.E. and Spalding, D.B., Mathematical Models of Turbulence. Academic Press, New York, 1972.

56. Hinze, J.O., Turbulence. McGraw Hill Publishing Company, New York, 1959.

57. Lilley, D.G., "Modeling of Combustor Swirl Flows." Acta Astronautica, Vol. 1, No. 9-10, 1974, pp. 1129-1147.

58. Khalil, E.E., Spalding, D.B., and Whitelaw, J.H., "The Calculation of Local Flow Properties in Two-Dimensional Furnaces." International Journal of Heat and Mass Transfer, Vol. 18, 1975, pp. 775-791.

59. Baker, R.J., Hutchinson, P., Khalil , E.E., and Whitelaw, J.H., "Measurements of Three Velocity Components in a Model Furnace With and Without Combustion." 15th International Symposium on Combustion, The Combustion Institute, Pittsburgh, Pennsylvania, 1975, pp. 553-559.

60. Karasu, T., "Numerical Prediction of Incompressible Turbulent Swirling Flows in Circular-Sectioned Ducts and Annuli." Ph.D. Thesis, Department of Mechanical Engineering, University of London, 1980.

61. Sloan, D.G., "Modeling of Swirl in Turbulent Systems." Ph.D. Thesis, Department of Chemical Engineering, Bringham Young University, 1985.

62. Jones, W.P. and Pascau, A., "Calculation of Confined Swirling Flows With a Second Moment Closure." Journal of Fluids Engineering, Vol. 111, September 1989, pp. 248-255.

63. Lilley, D.G. and Rhode, D.L., "STARPIC: A Computer Code for Swirling Turbulent Axisymmetric Recirculating Flows in Practical Isothermal Combustor Geometries." NASA-CR-3442, June, 1981.

64. Lilley, D.G., "Investigation of Flowfields Found in Typical Combustor Geometries." Final Report on Grant NAG3-74, NASA CR-3869, February, 1985.

65. Ramos, J.I., "A Numerical Study of a Swirl Stabilized Combustor." Journal of Non-Equilibrium Thermodynamics, Vol. 10, 1985, pp. 263-286.

66. Sturgess, G.J., Syed, S.A., "Calculation of Confined Swirling Flows." AIAA Paper No. 85-0060, 1985.

67. Sloan, D.G., Smith, P.J., and Smoot, L.D., "Modeling of Swirl in Turbulent Flow Systems." Progress in Energy and Combustion Science, Vol. 12, 1986, pp. 163-250.

68. Brondum, D.C., Bennett, J.C., Weinberg, B.C., and McDonald, H., "Numerical and Experimental Investigation of Non-Swirling and Swirling Jets." AIAA Paper No. 86-0040, 1986.

69. Lilley, D.G. and Chigier, N.A., "Nonisotropic Turbulent Stress Distribution in Swirling Flows from Mean Value Distribution." International Journal of Heat and Mass Transfer, Vol. 14, 1971, pp. 573-585.

70. Rodi, W., "Influence of Buoyancy and Rotation on Equations for the Turbulent Length Scale." Second International Symposium on Turbulent Shear Flows, 10.37-10.42, 1979, Imperial College, London.

71. Sander, G.F. and Lilley, D.G., "The Performance of an Annular Vane Swirler." AIAA Paper No. 83-1326, 1983.

72. Abujelala, M.T. and Lilley, D.G., "Limitations and Empirical Extensions of the k-ϵ Model as Applied to Turbulent Confined Swirling Flows." AIAA paper No. 84-0441, 1984.

73. Kobayashi, T. and Yoda, M., "Modified k-ϵ Model for Turbulent Swirling Flow in a Straight Pipe." JSME International Journal, Vol. 30, No. 259, 1987, pp. 66-71.

74. Halal, A.S. and Lilley, D.G., "Flow Computations with a Body-Fitted Nonorthogonal Grid System." AIAA Paper No. 90-0154, 1990.

75. Halal, A.S. and Lilley, D.G., "Constricted Flow Predictions with a Nonorthogonal Grid Using Stream Function and Vorticity Variables." ASME International Computers in Engineering Conference, August 5-9, 1990, Boston, MA.

76. Bentz, J.C., "Hemodynamic Flow in the Region of a Simulated Stenosis." Ph.D. Thesis, University of Pennsylvania, University Park, Pennsylvania, 1974.

77. Deshpande, M.D. and Giddens, D.P., "Turbulent Measurements in a Constricted Tube." Journal of Fluid Mechanics, Vol. 97, No. 1, 1980, pp. 65-89.

78. Abujelala, M.T. and Lilley, D.G., "Confined Swirling Flow Predictions." AIAA Paper No. 83-.316, 1983.

APPENDIXES

APPENDIX A

TABLES

TABLE I

COEFFICIENTS AND SOURCE TERMS USED IN THE GOVERNING EQUATIONS FOR THE GENERAL VARIABLE φ

φ	b^{φ}	Γ^{φ}	S^{φ}
ψ	0	1	$-\frac{2}{r}\frac{\partial \psi}{\partial r} + r\omega$
ω	1	μ_{eff}	$-\rho \frac{\partial}{\partial x}\left(\frac{w^2}{r}\right) + S_{\omega}$
w	1	μ_{eff}	$-\frac{w}{r^2}\frac{\partial}{\partial r}(\mu r) - \rho \frac{vw}{r}$
k	1	μ_{eff}/σ_k	$G_k - \rho\epsilon$
ϵ	1	$\mu_{eff}/\sigma_{\epsilon}$	$C_1 G_k \epsilon/k - C_2 \rho \epsilon^2/k$

where

$$S_{\omega} = \omega\left[\frac{1}{r}\frac{\partial \mu}{\partial r} - \frac{\mu}{r^2} + \frac{\partial^2 \mu}{\partial r^2}\right] + \frac{\partial \omega}{\partial r}\frac{\partial \mu}{\partial r}$$

The turbulence generation term, G_k, and the turbulence model constants are as given in Chapter 3.

TABLE II

SELECTED TEST CASES

Case No.	Author(s)	Fluid	Flow Type	Properties Measured	Swirl
1	Bentz	Water	Laminar	u	No
2	Bornstein & Escudier	Water	Laminar	u, w	Yes
3	Deshpande & Giddens	Water	Turbulent	u, u′	No
4	Yoon & Lilley	Air	Turbulent	u, v, w	No
5	Yoon & Lilley	Air	Turbulent	u, v, w	Yes
6	Weber et al.	Air	Turbulent	u, w, u′ w′, u′w′	Yes

TABLE III

AVERAGE ABSOLUTE ERROR FOR 2-D FIELD PROBLEM
IN CARTESIAN COORDINATES

H/L	Grid Density	Stair-Steps	Displaced	Linear	Quadratic
0.5	11 x 6	0.228	0.343	0.267	0.277
	21 x 11	0.224	0.307	0.365	0.063
	31 x 16	0.171	0.305	0.372	0.027
1.0	11 x 6	0.801	0.996	2.021	0.195
	21 x 11	0.489	0.930	1.827	0.043
	31 x 16	0.347	0.904	1.754	0.018
2.0	11 x 6	1.245	2.365	5.340	0.175
	21 x 11	0.702	2.251	4.678	0.040
	31 x 16	0.490	2.186	4.466	0.017
4.0	11 x 6	1.472	4.000	8.110	0.240
	21 x 11	0.798	3.935	7.063	0.056
	31 x 16	0.550	3.844	6.736	0.024

TABLE IV

AVERAGE ABSOLUTE ERROR PERCENTAGE FOR 2-D FIELD PROBLEM IN CARTESIAN COORDINATES

H/L	Grid Density	Stair-Steps	Displaced	Linear	Quadratic
0.5	11 x 6	1.638	5.994	3.311	4.234
	21 x 11	1.961	3.674	4.944	0.980
	31 x 16	1.652	3.349	5.164	0.409
1.0	11 x 6	2.657	5.045	10.434	1.216
	21 x 11	1.955	4.549	10.005	0.286
	31 x 16	1.488	4.433	9.792	0.121
2.0	11 x 6	2.515	6.390	14.373	0.555
	21 x 11	1.627	6.382	13.286	0.139
	31 x 16	1.210	6.319	12.909	0.060
4.0	11 x 6	2.367	7.826	15.794	0.521
	21 x 11	1.473	8.814	14.420	0.132
	31 x 16	1.082	8.167	13.963	0.057

TABLE V

AVERAGE ABSOLUTE ERROR FOR 2-D FIELD PROBLEM
IN AXISYMMETRIC COORDINATES

H/L	Grid Density	Stair-Steps	Displaced	Linear	Quadratic
0.5	11 x 6	0.400	0.736	0.018	0.192
	21 x 11	0.275	0.852	0.112	0.044
	31 x 16	0.197	0.858	0.131	0.091
1.0	11 x 6	0.927	2.044	0.661	0.087
	21 x 11	0.556	2.064	0.661	0.019
	31 x 16	0.379	2.037	0.650	0.008
2.0	11 x 6	1.052	2.755	1.575	0.038
	21 x 11	0.699	2.759	1.480	0.009
	31 x 16	0.458	2.728	1.439	0.004
4.0	11 x 6	0.963	2.512	1.919	0.065
	21 x 11	0.707	2.707	1.849	0.017
	31 x 16	0.449	2.699	1.812	0.008

TABLE VI

AVERAGE ABSOLUTE ERROR PERCENTAGE FOR 2-D FIELD PROBLEM IN AXISYMMETRIC COORDINATES

H/L	Grid Density	Stair-Steps	Displaced	Linear	Quadratic
0.5	11 x 6	3.829	7.221	1.116	1.817
	21 x 11	2.018	8.275	1.132	0.419
	31 x 16	2.750	8.340	2.635	0.318
1.0	11 x 6	2.750	8.490	2.635	0.318
	21 x 11	2.685	8.779	2.656	0.072
	31 x 16	1.917	8.726	2.619	0.029
2.0	11 x 6	2.949	7.061	3.626	0.096
	21 x 11	2.282	7.358	3.442	0.024
	31 x 16	1.609	7.353	3.359	0.011
4.0	11 x 6	2.530	5.347	3.583	0.142
	21 x 11	2.095	6.283	3.469	0.038
	31 x 16	1.463	6.355	3.408	0.018

TABLE VII

AVERAGE ABSOLUTE ERROR FOR DIFFERENT DEGREES OF EXTRAPOLATION USING THE QUADRATIC SCHEME

H/L	Grid Density	Cartesian	Axisymmetric
0.5	21 x 11	0.063	0.044
	21 x 31	0.037	0.026
	21 x 61	0.032	0.021
1.0	21 x 11	0.043	0.019
	21 x 31	0.013	0.007
	21 x 61	0.014	0.005

TABLE VIII

AVERAGE ABSOLUTE ERROR PERCENTAGES FOR DIFFERENT DEGREES OF EXTRAPOLATION USING THE QUADRATIC SCHEME

H/L	Grid Density	Cartesian	Axisymmetric
0.5	21 x 11	0.980	0.419
	21 x 31	0.549	0.245
	21 x 61	0.376	0.149
1.0	21 x 11	0.286	0.072
	21 x 31	0.080	0.029
	21 x 61	0.185	0.018

TABLE IX

COMPARISON OF THE RATE OF DECAY OF MAXIMUM AXIAL VELOCITY Umax/Uin FOR CASE 5

x/D_c	Present Study	Sloan (Ref. 61) k-ϵ	Sloan (Ref. 61) LPS	Sloan (Ref. 61) Rich. No.	Sloan (Ref. 61) ASM	Yoon & Lilley (Ref. 47)
0.5	0.90	0.85	0.60		0.75	0.98
1.0	0.43	0.38	0.40		0.47	0.58
1.5	0.29	0.29	0.29		0.29	0.30
2.0	0.26	0.26	0.26		0.26	0.27

TABLE X

COMPARISON OF THE RATE OF DECAY OF MAXIMUM SWIRL VELOCITY Wmax/Uin FOR CASE 5

x/D_c	Present Study	Sloan (Ref. 61) k-ϵ	Sloan (Ref. 61) LPS	Sloan (Ref. 61) Rich. No.	Sloan (Ref. 61) ASM	Yoon & Lilley (Ref. 47)
0.5	0.48	0.46	0.42		0.32	0.30
1.0	0.35	0.40	0.40		0.40	0.48
1.5	0.32	0.37	0.35		0.37	0.52
2.0	0.30	0.35	0.35		0.35	0.51

APPENDIX B

FIGURES

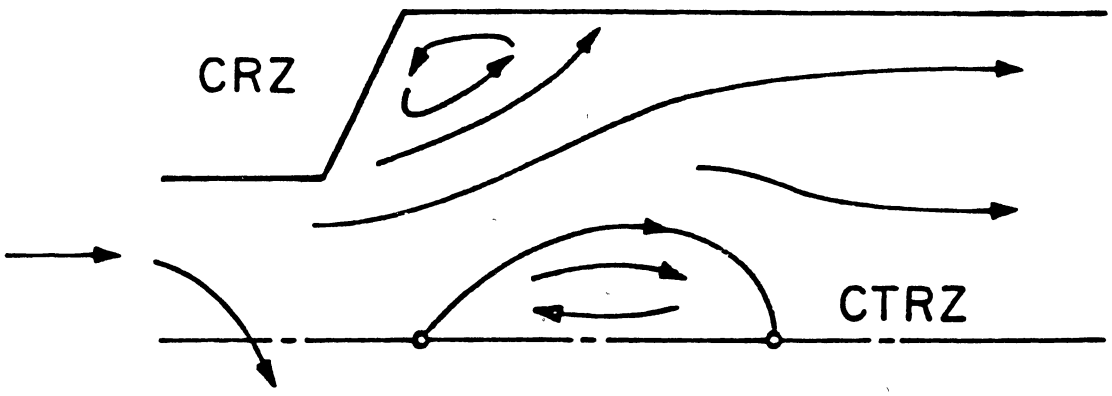

Figure 1. A Schematic Illustration of the Type of Flows Considered

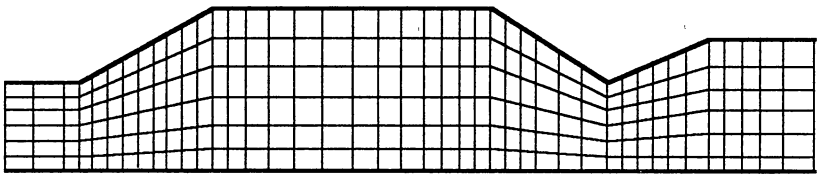

Figure 2. Nonorthogonal Mesh for Irregularly-Shaped Domain

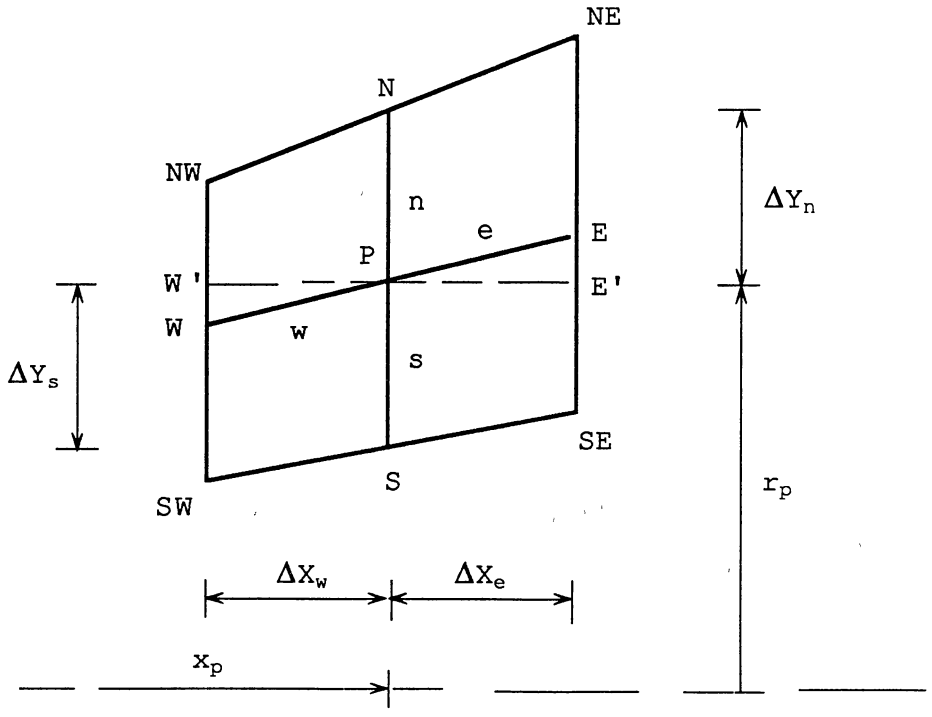

Figure 3. Typical Point in Nonorthogonal Grid

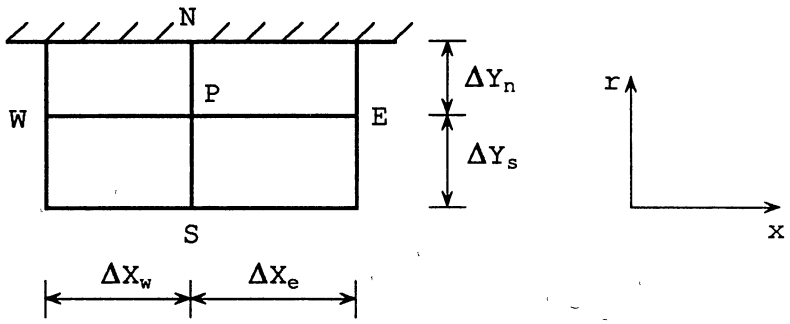

(a) Horizontal Wall

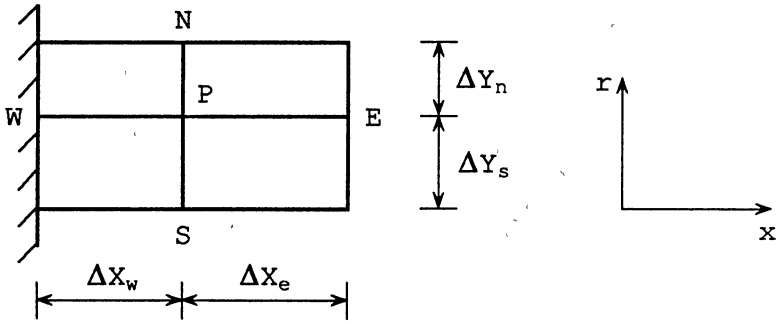

(b) Vertical Wall

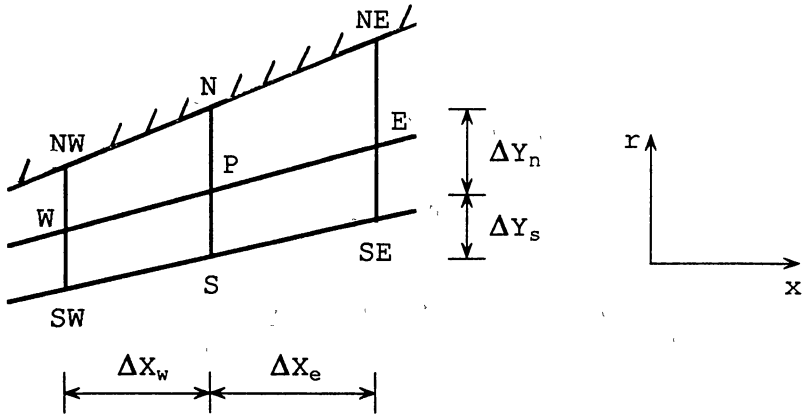

(c) Inclined Wall

Figure 4. Typical Near Wall Grid Point

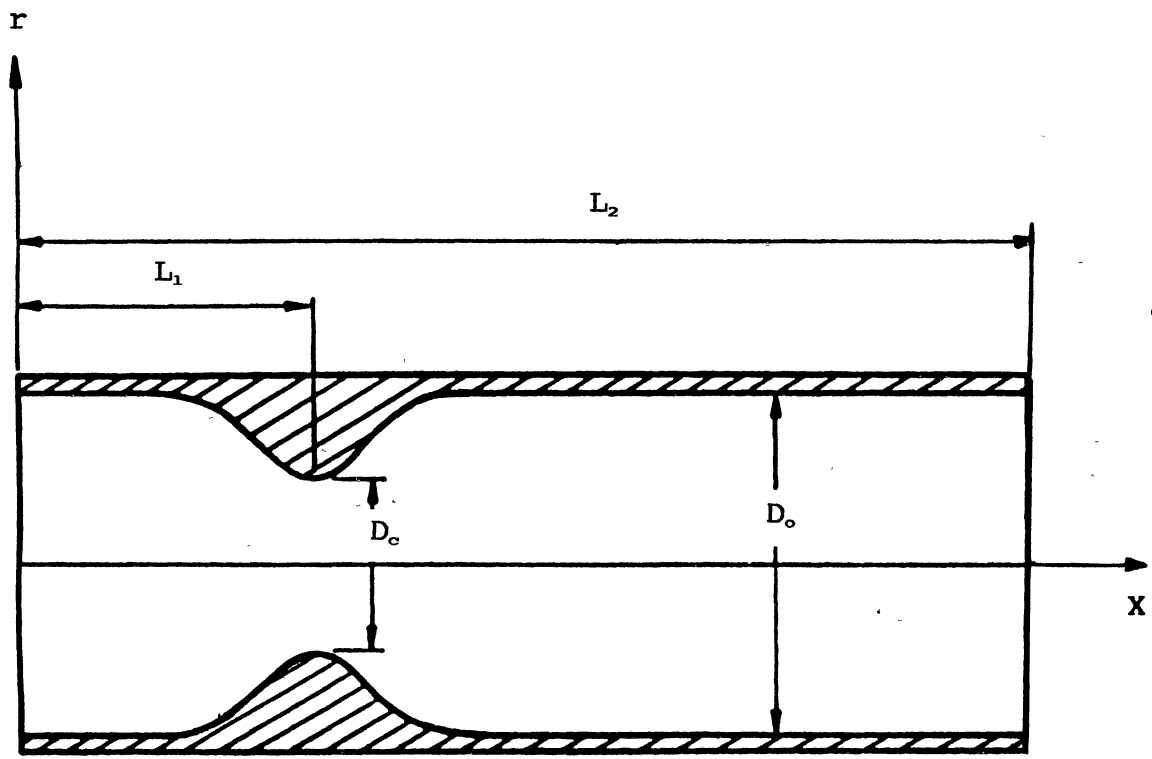

(a) Cases 1 and 3 [Bentz, Ref. 76; Deshpande & Giddens, Ref. 77]

Figure 5. Schematic Illustration of Test Cases

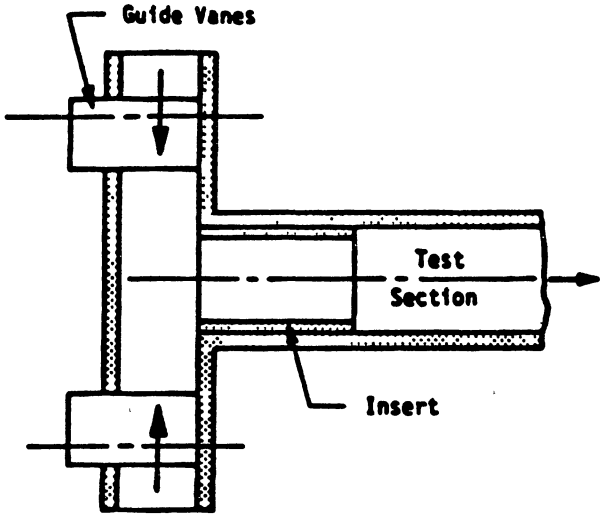

(b) Case 2 [Bornstein & Escudier, Ref. 42]

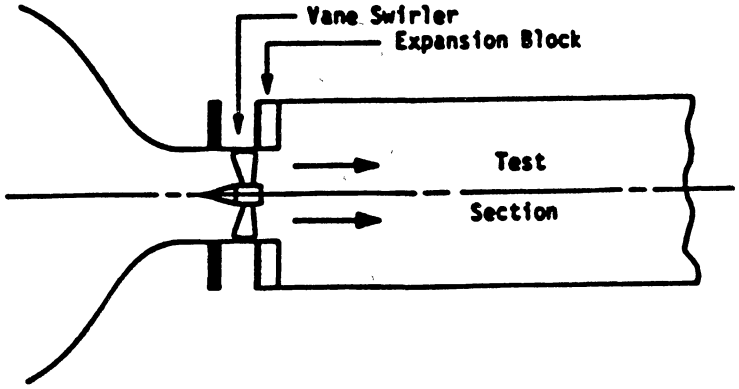

(c) Cases 4 and 5 [Yoon & Lilley, Ref. 47]

Figure 5 (Continued)

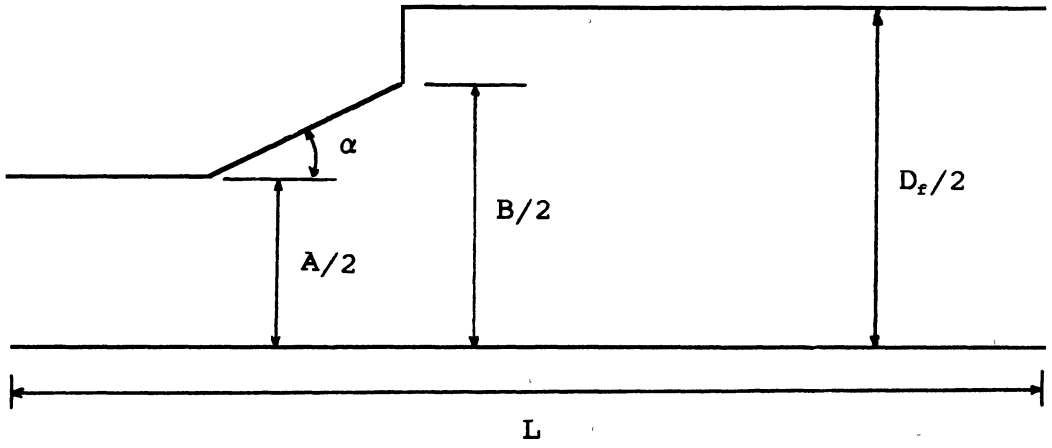

(d) Case 6 [Weber et al., Ref. 54]

Figure 5 (Continued)

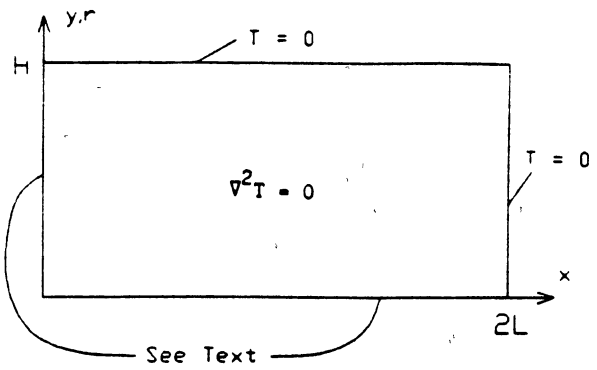

Figure 6. Two-Dimensional Field Problem

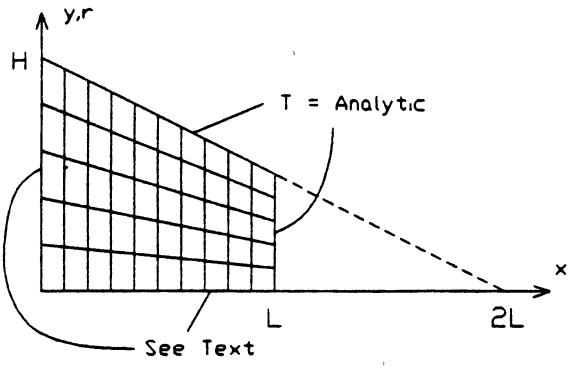

Figure 7. Test Section For Two-Dimensional Field Problem

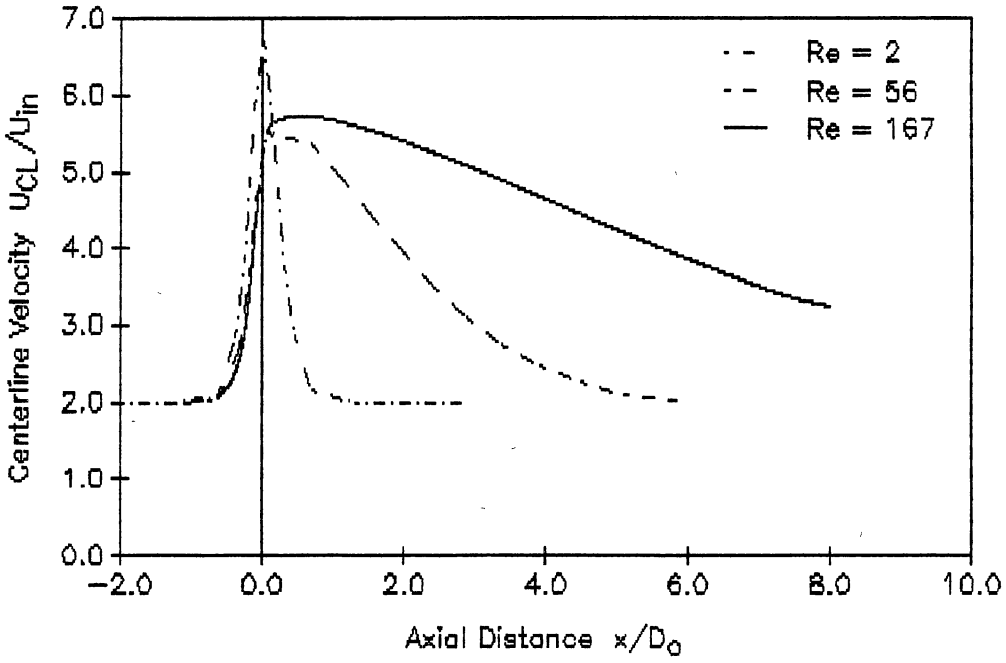

Figure 8. Case 1; Predicted Centerline Velocity for Various Reynolds Numbers [Bentz, Ref. 76]

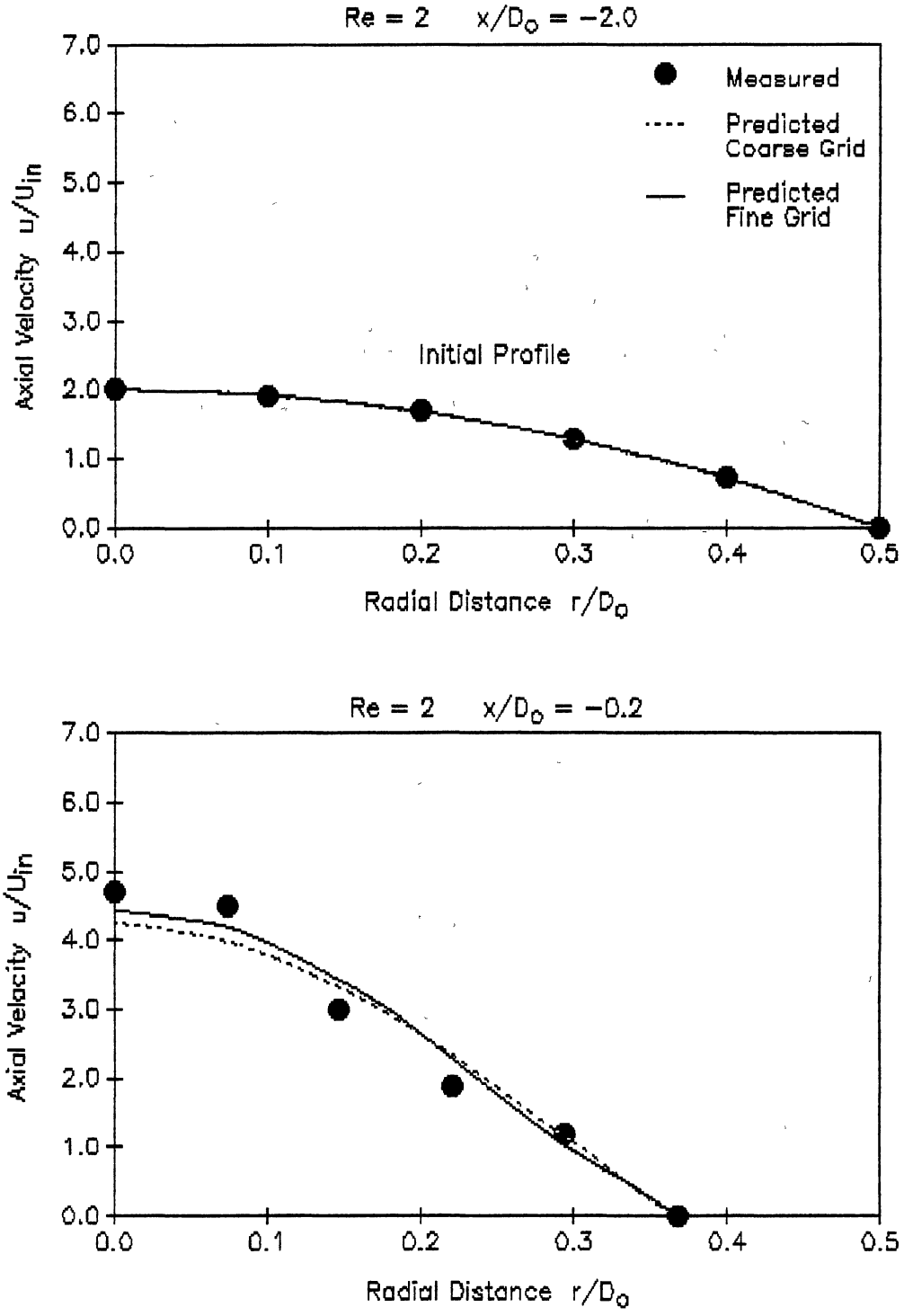

Figure 9. Case 1; Comparison of Predicted and Measured Axial Velocity Profiles for Re = 2 [Bentz, Ref. 76]

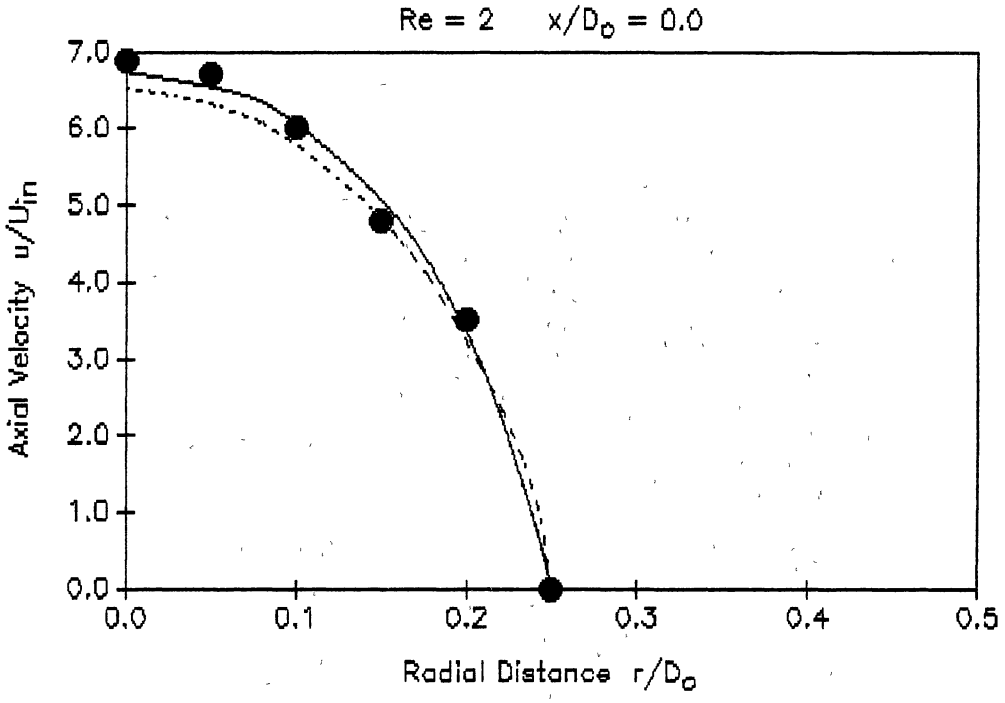

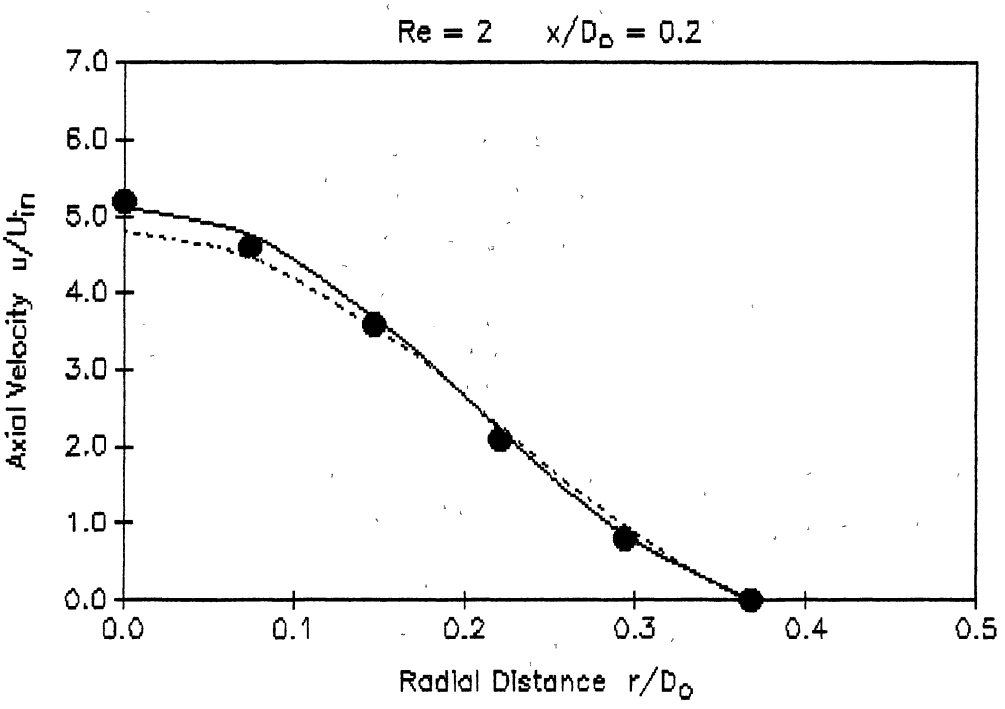

Figure 9 (Continued)

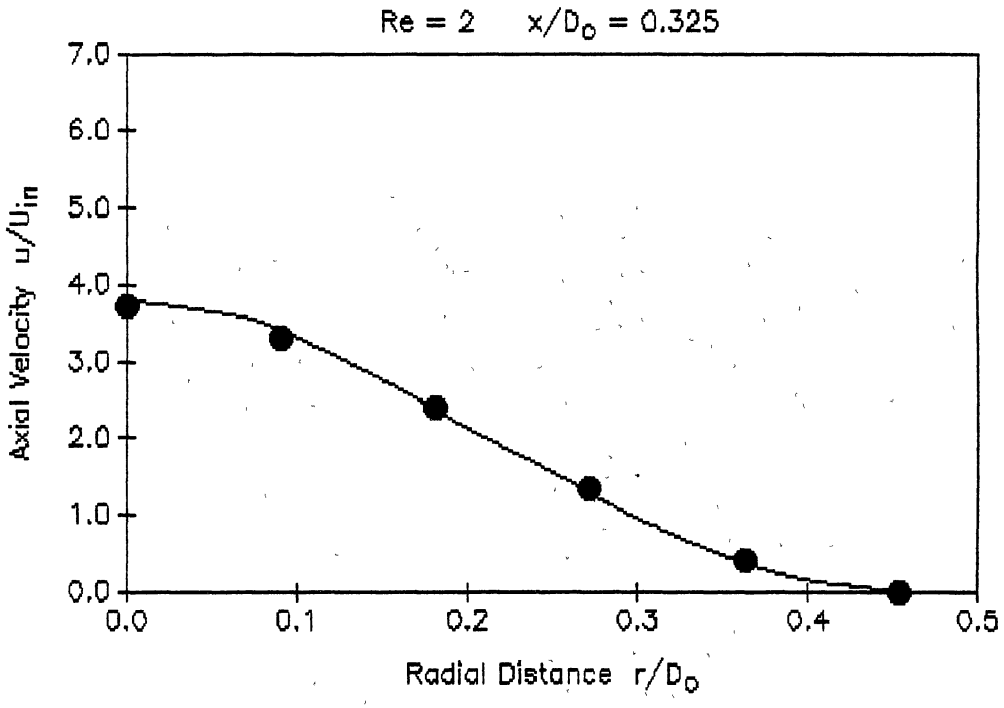

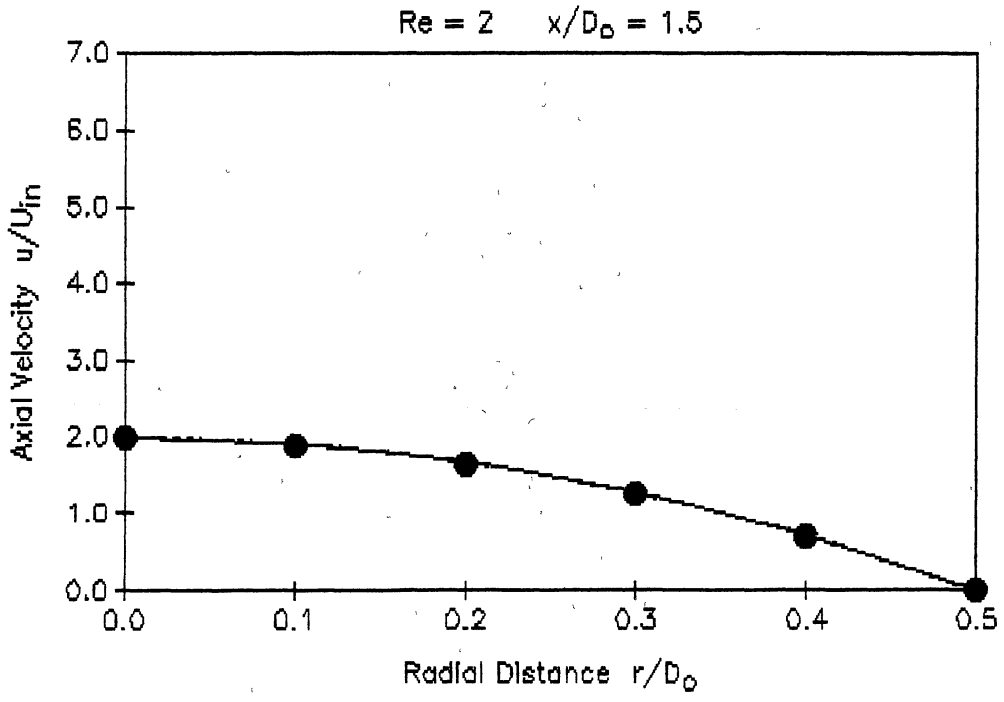

Figure 9 (Continued)

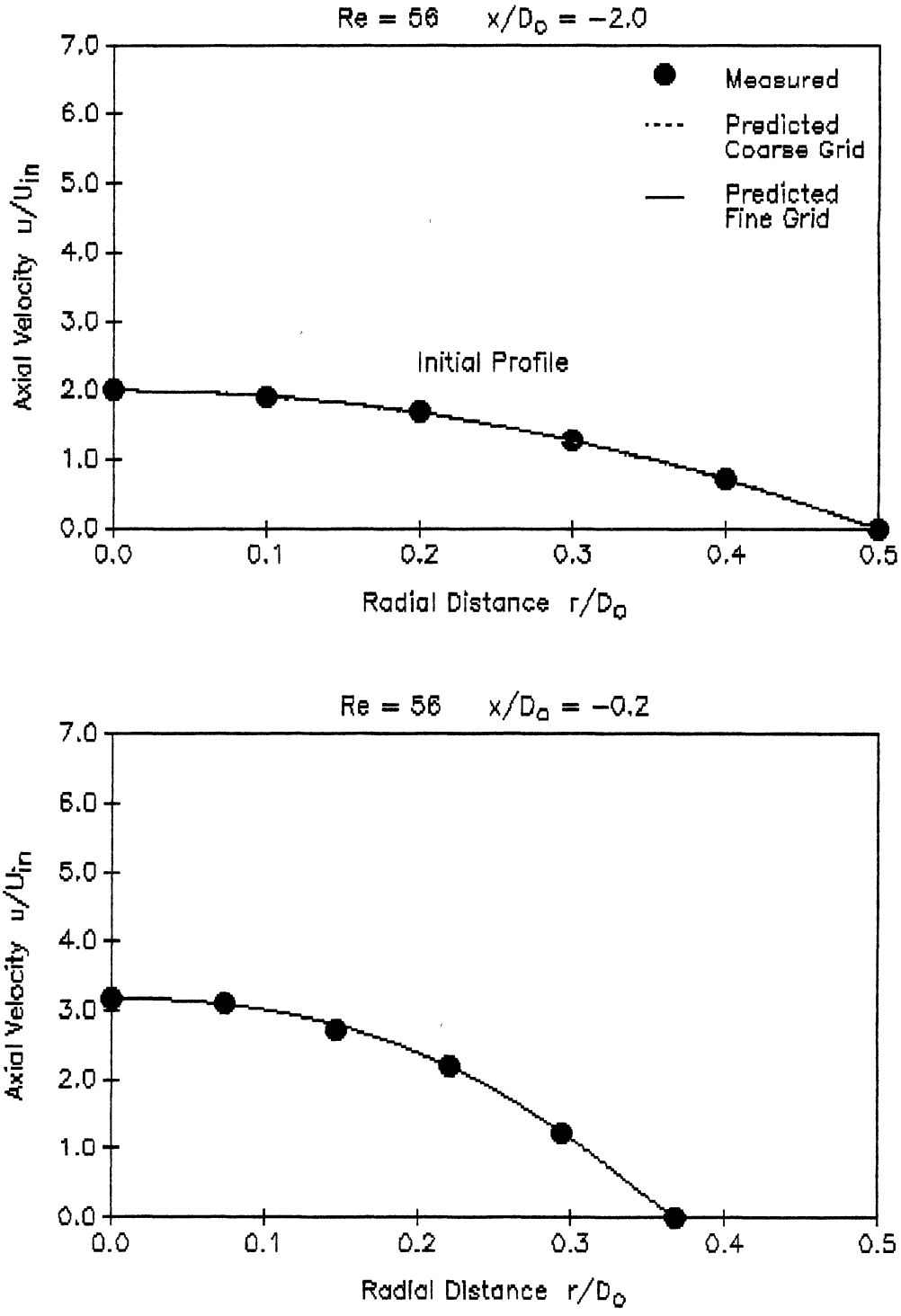

Figure 10. Case 1; Comparison of Predicted and Measured Axial Velocity Profiles for Re = 56 [Bentz, Ref. 76]

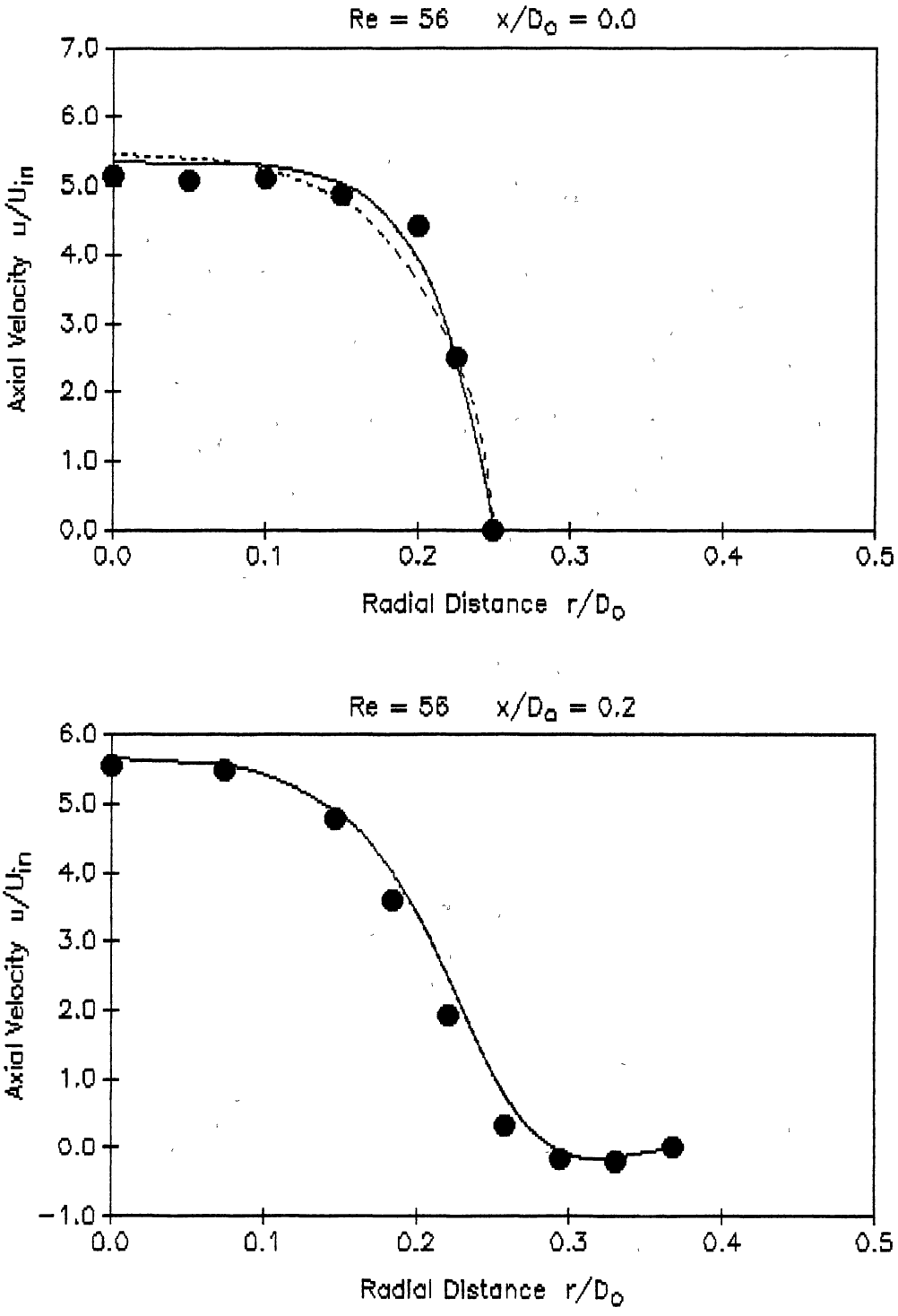

Figure 10 (Continued)

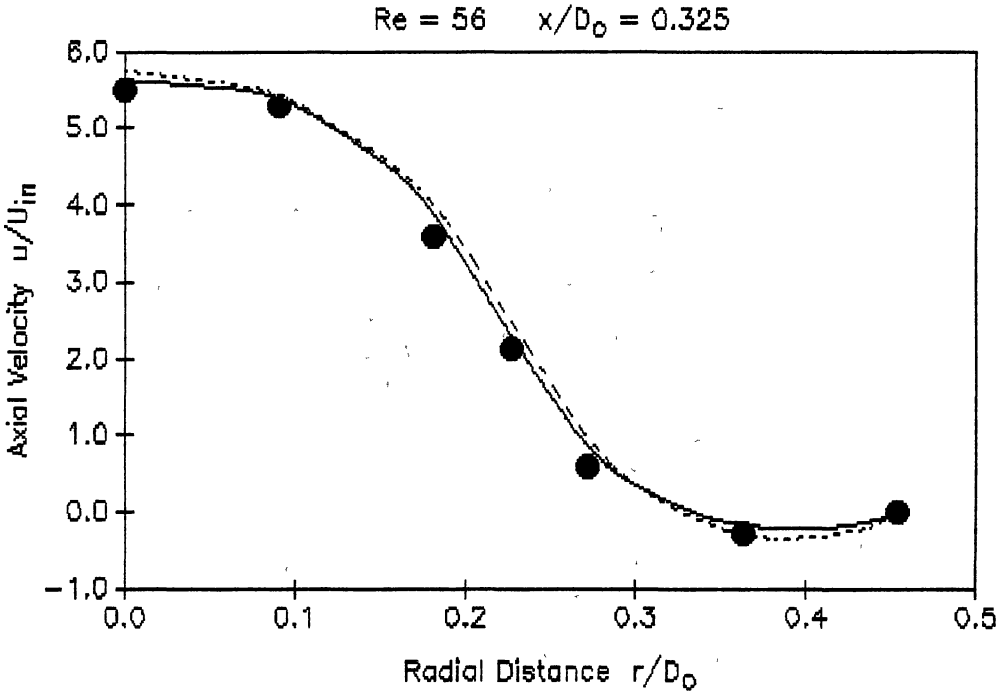

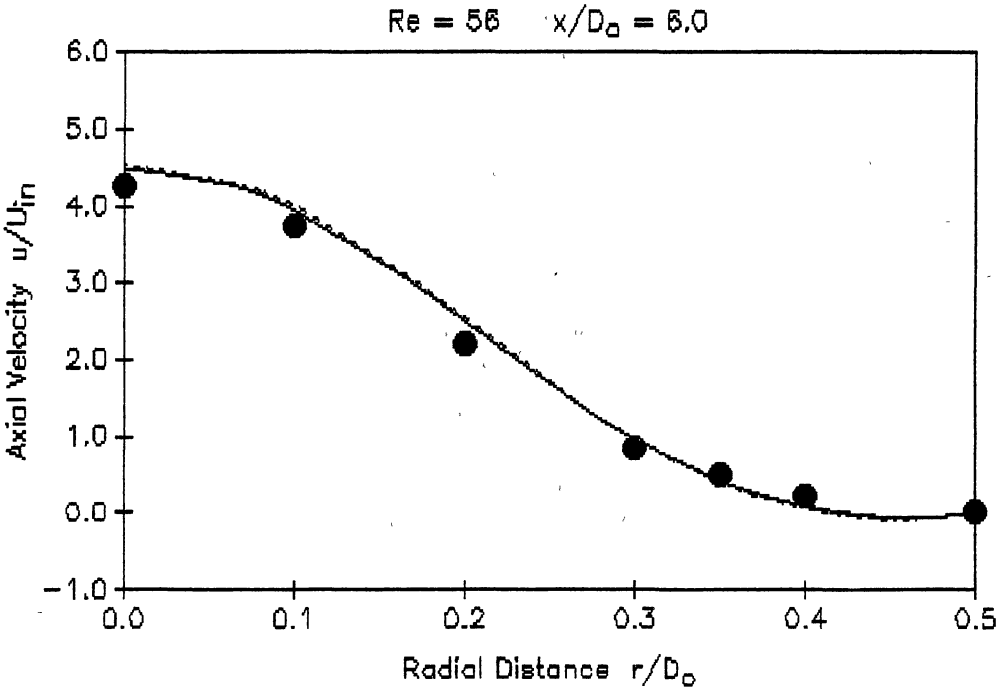

Figure 10 (Continued)

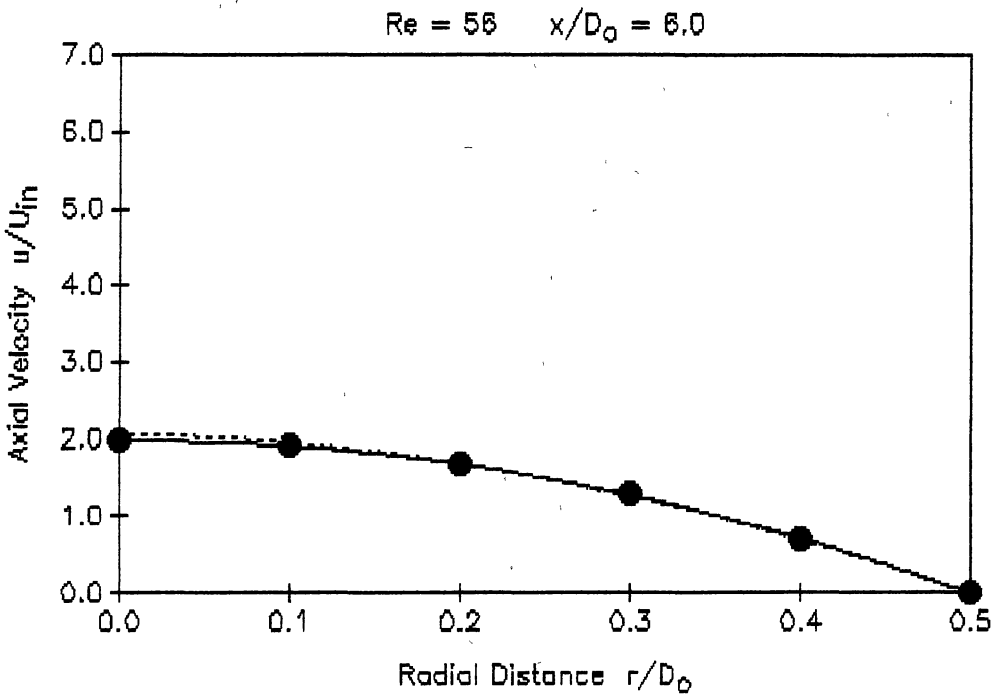

Figure 10 (Continued)

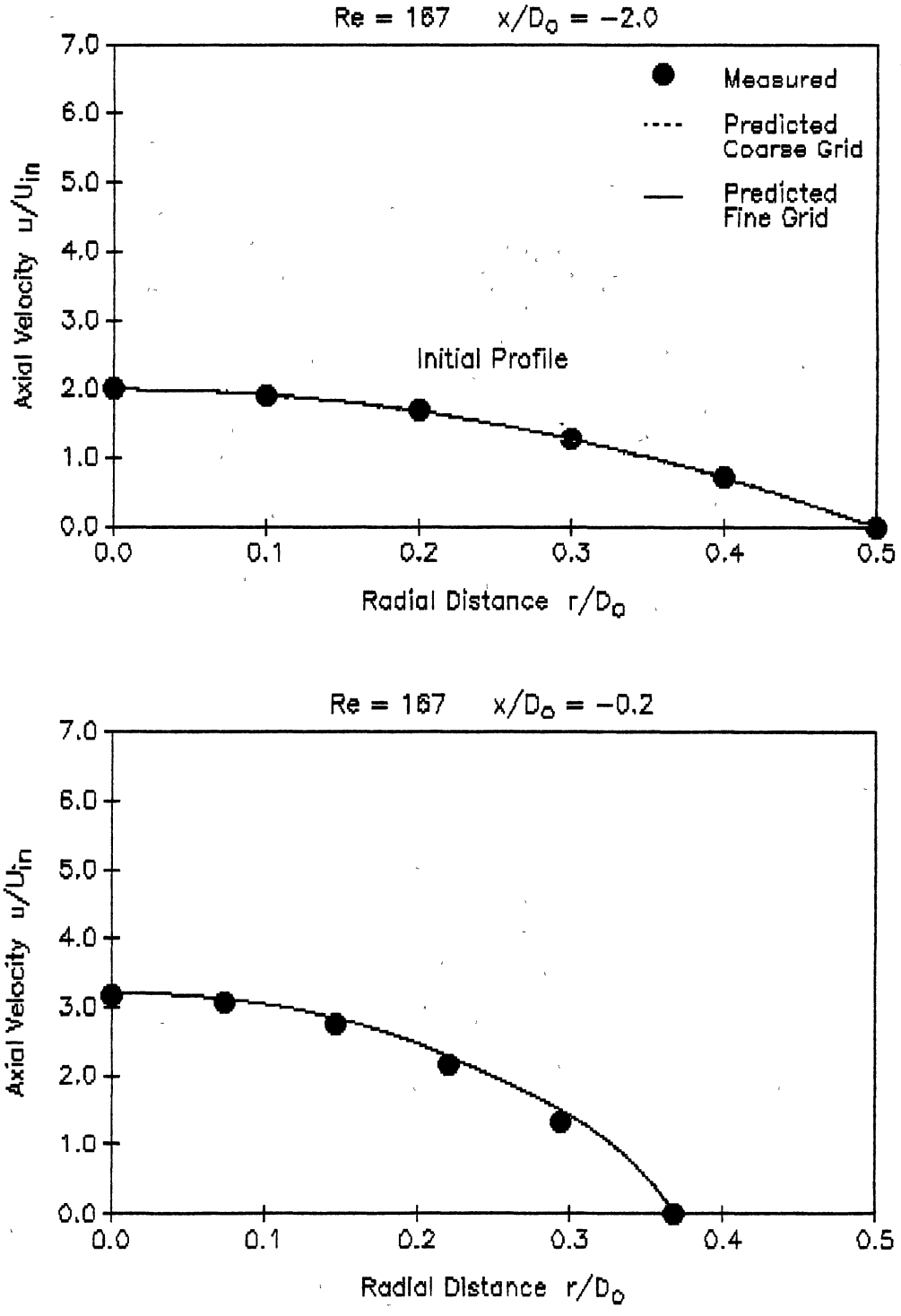

Figure 11. Case 1; Comparison of Predicted and Measured Axial Velocity Profiles for Re = 167 [Bentz, Ref. 76]

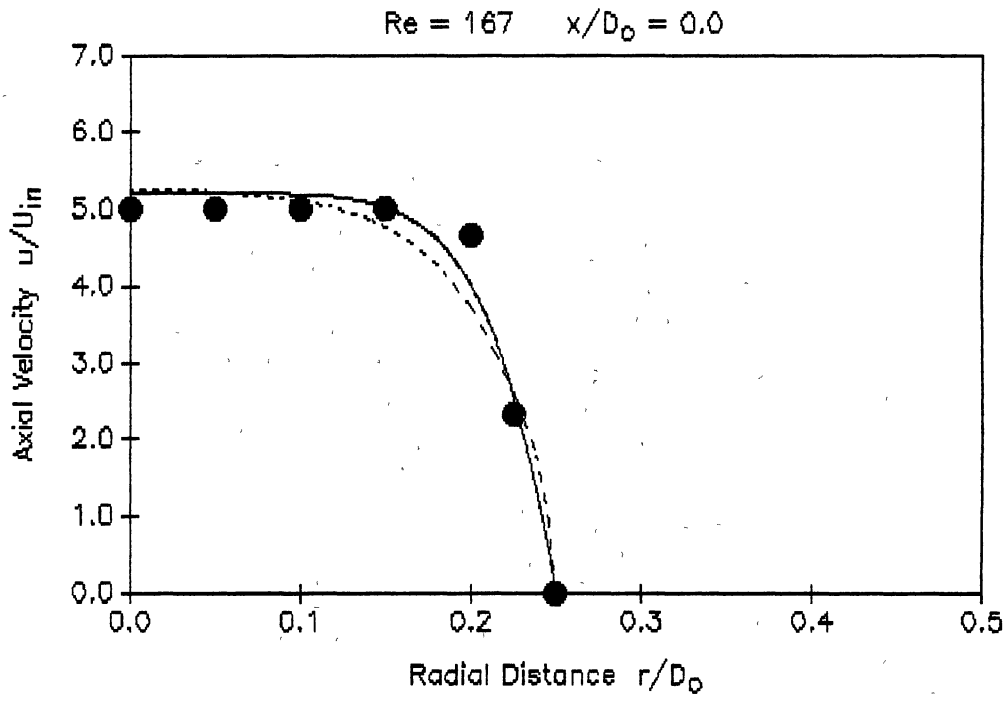

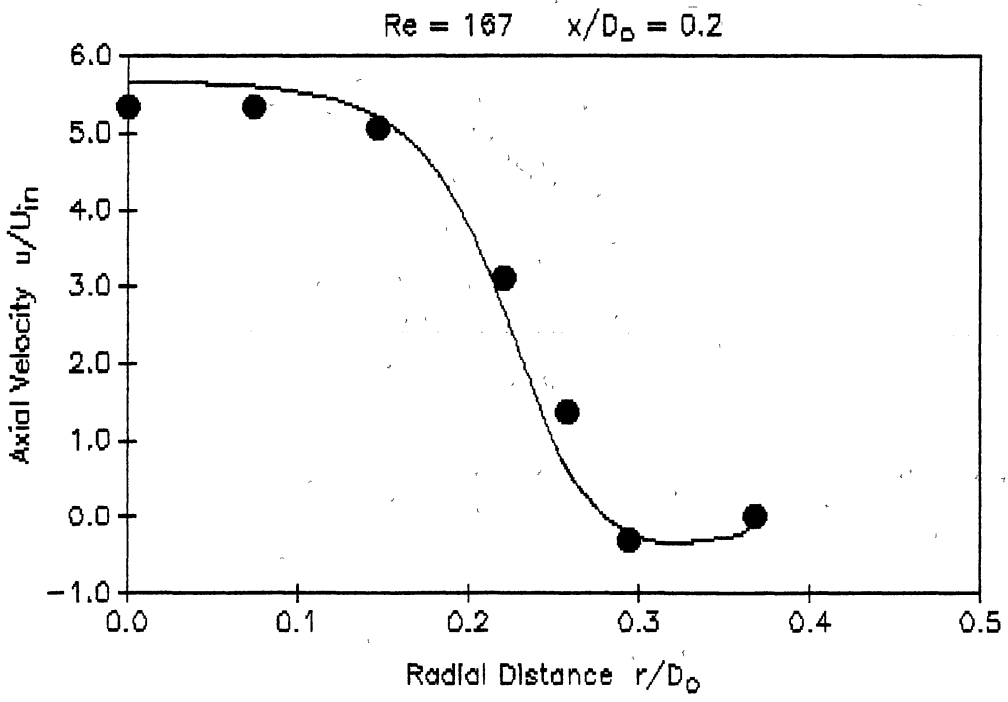

Figure 11 (Continued)

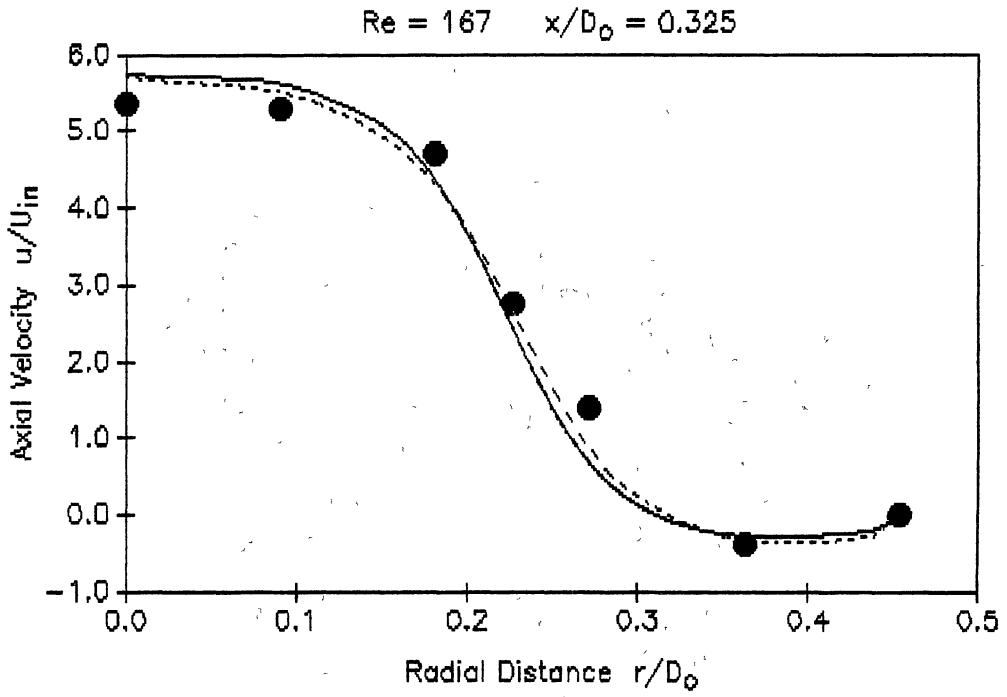

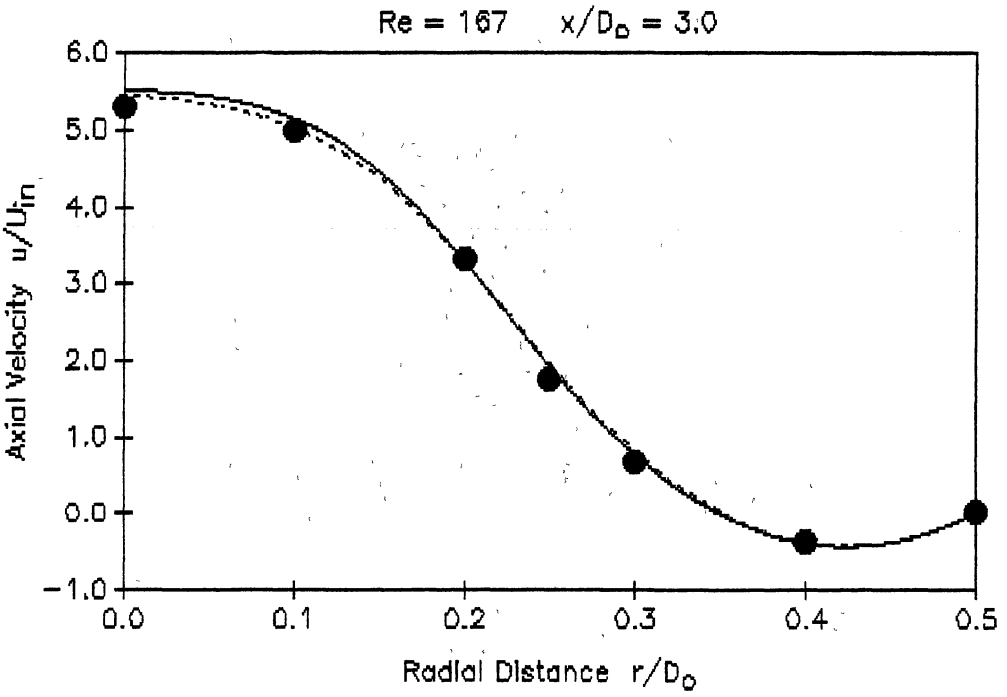

Figure 11 (Continued)

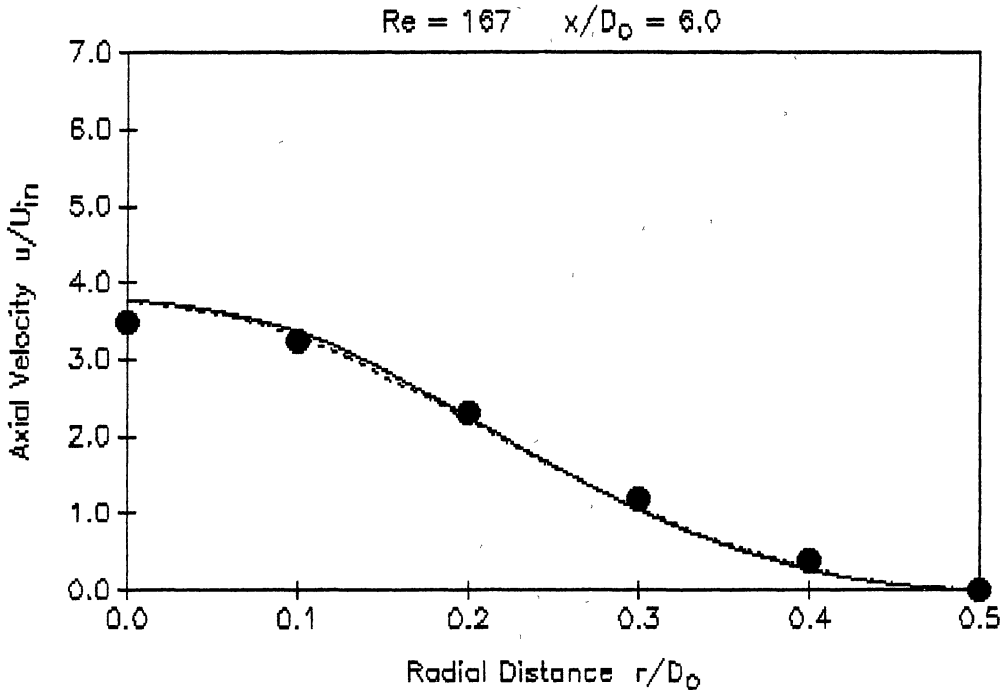

Figure 11 (Continued)

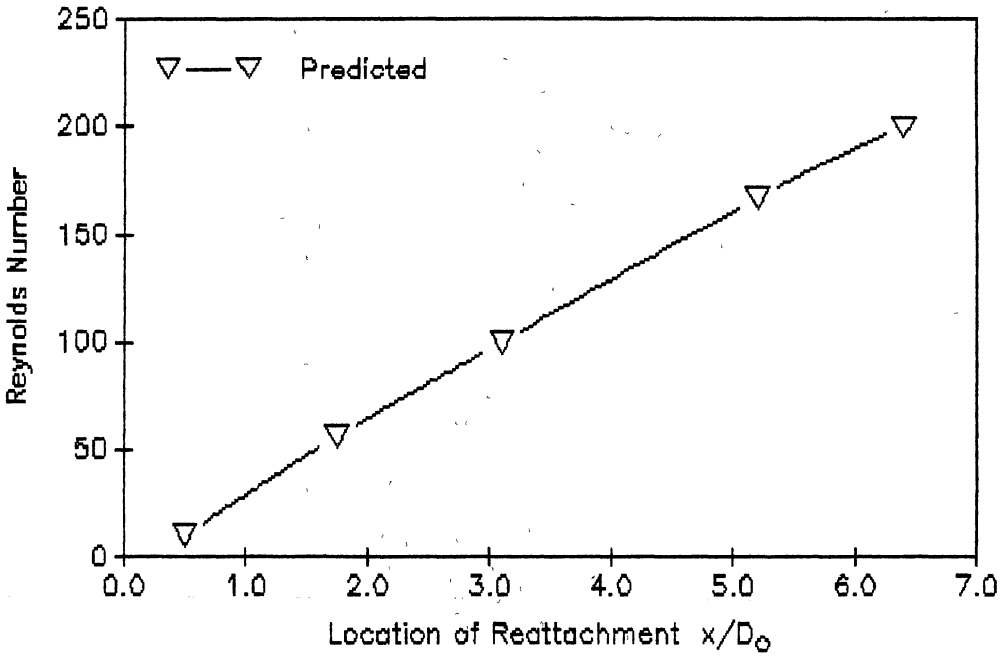

Figure 12. Case 1; Predicted Location of Reattachment for Various Reynolds Numbers [Bentz, Ref. 76]

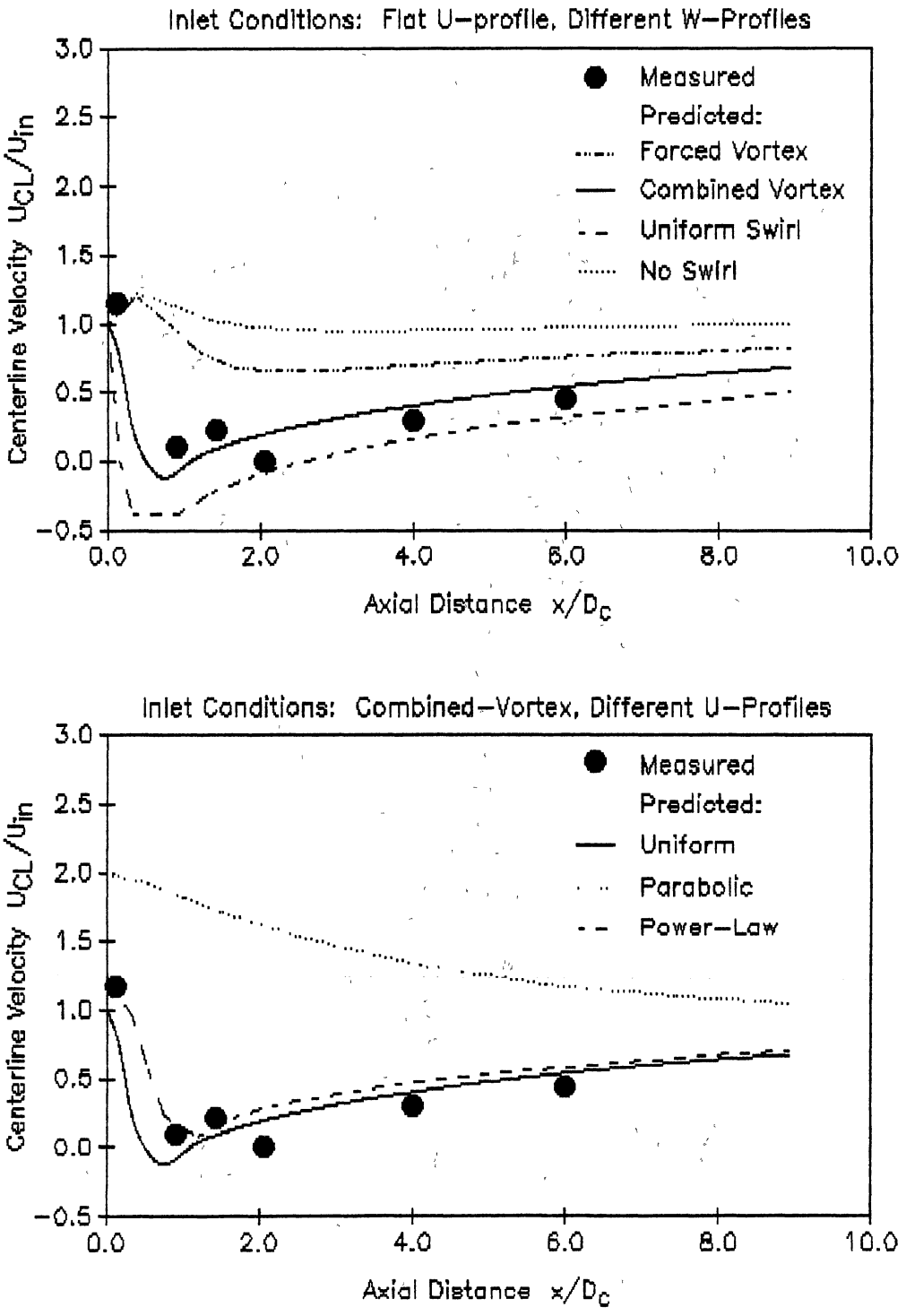

Figure 13. Case 2; Predicted Centerline Velocity for Different Inlet Conditions [Bornstein & Escudier, Ref. 42]

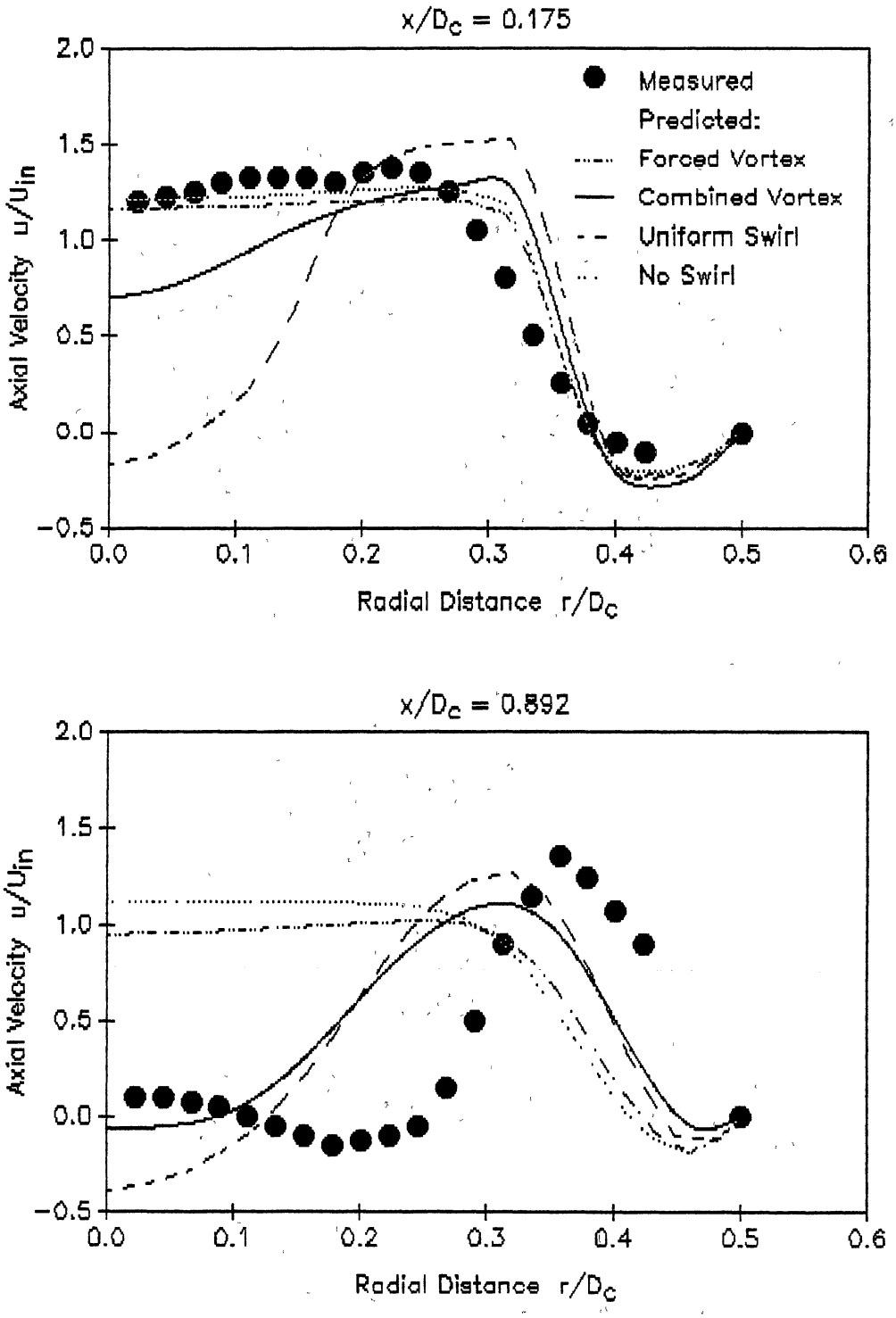

Figure 14. Case 2; Comparison of Predicted and Measured Axial Velocity Profiles [Bornstein & Escudier, Ref. 42]

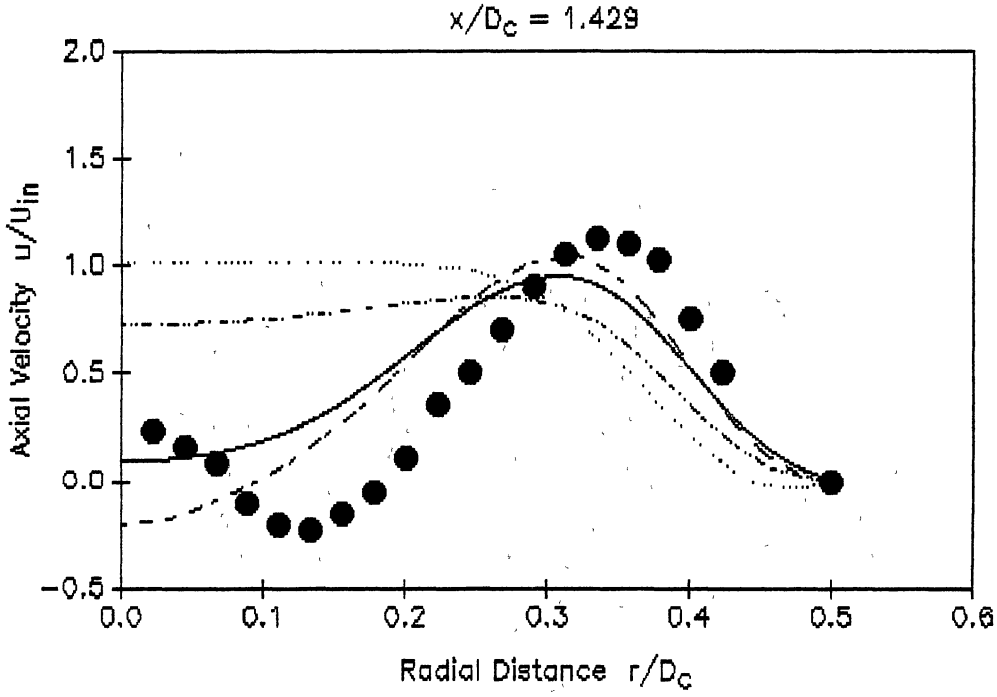

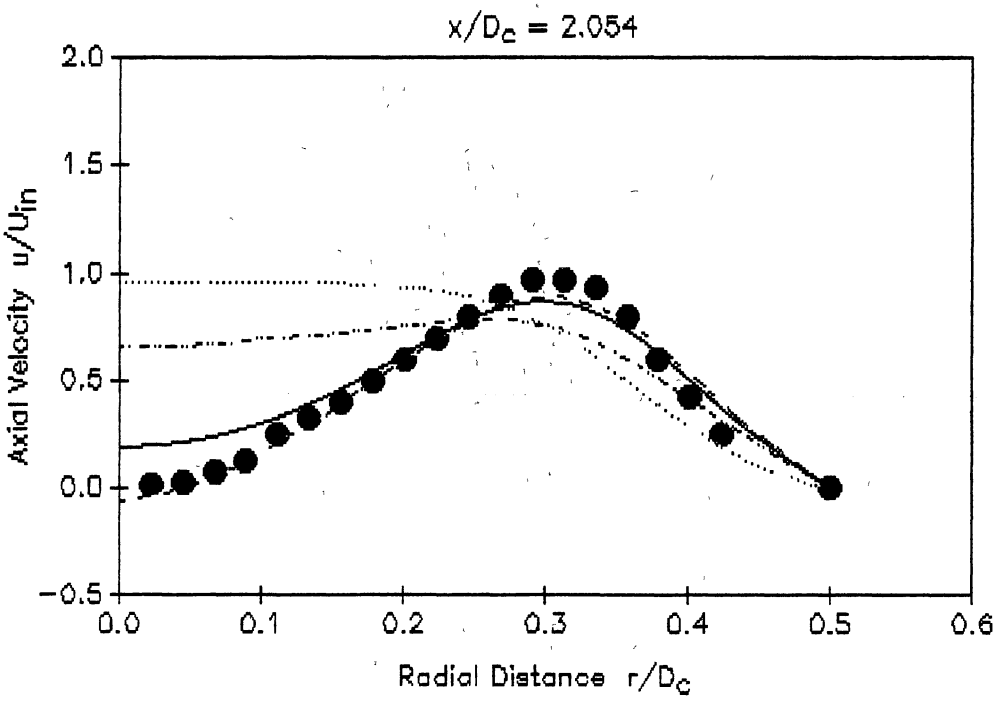

Figure 14 (Continued)

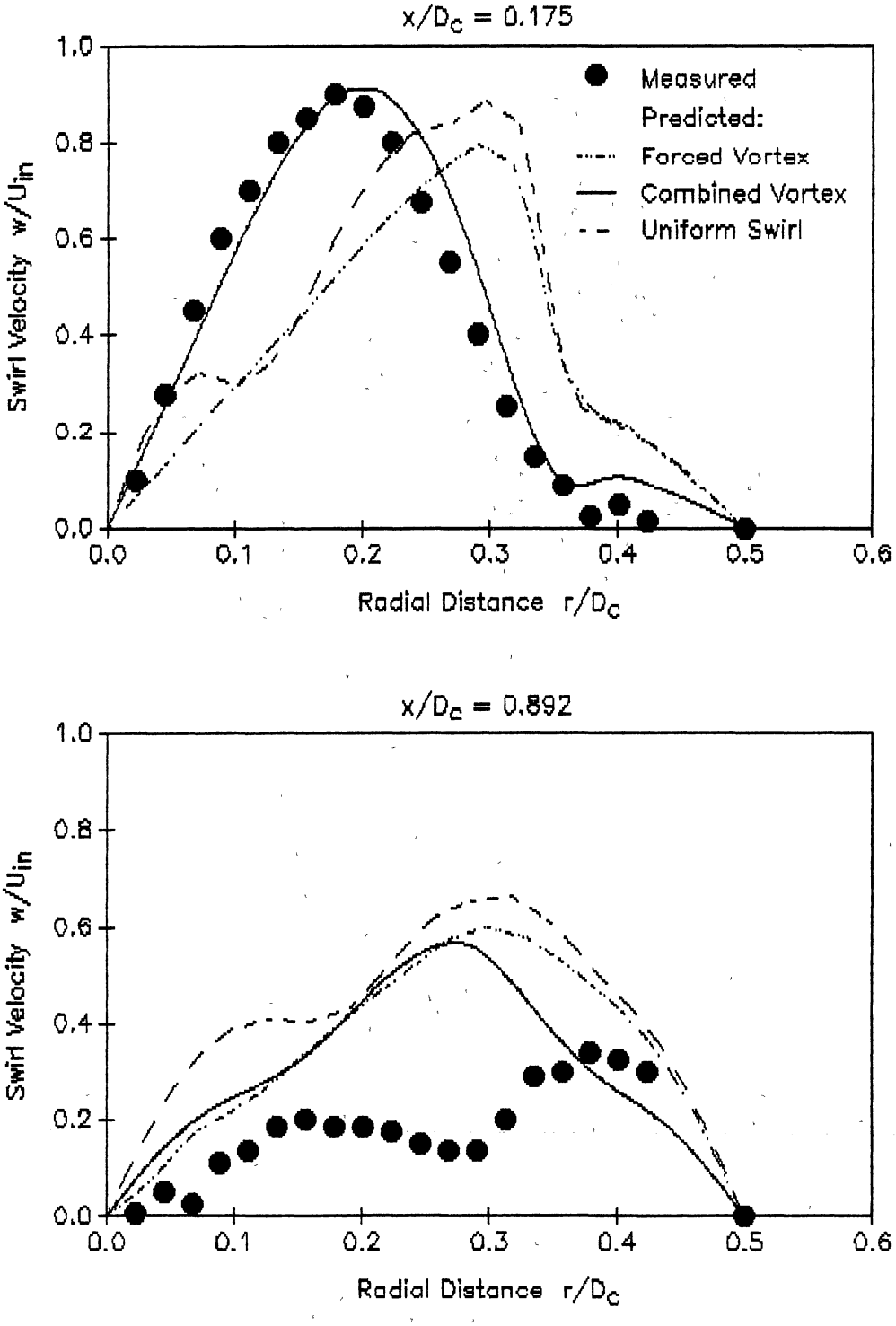

Figure 15. Case 2; Comparison of Predicted and Measured Swirl Velocity Profiles [Bornstein & Escudier, Ref. 42]

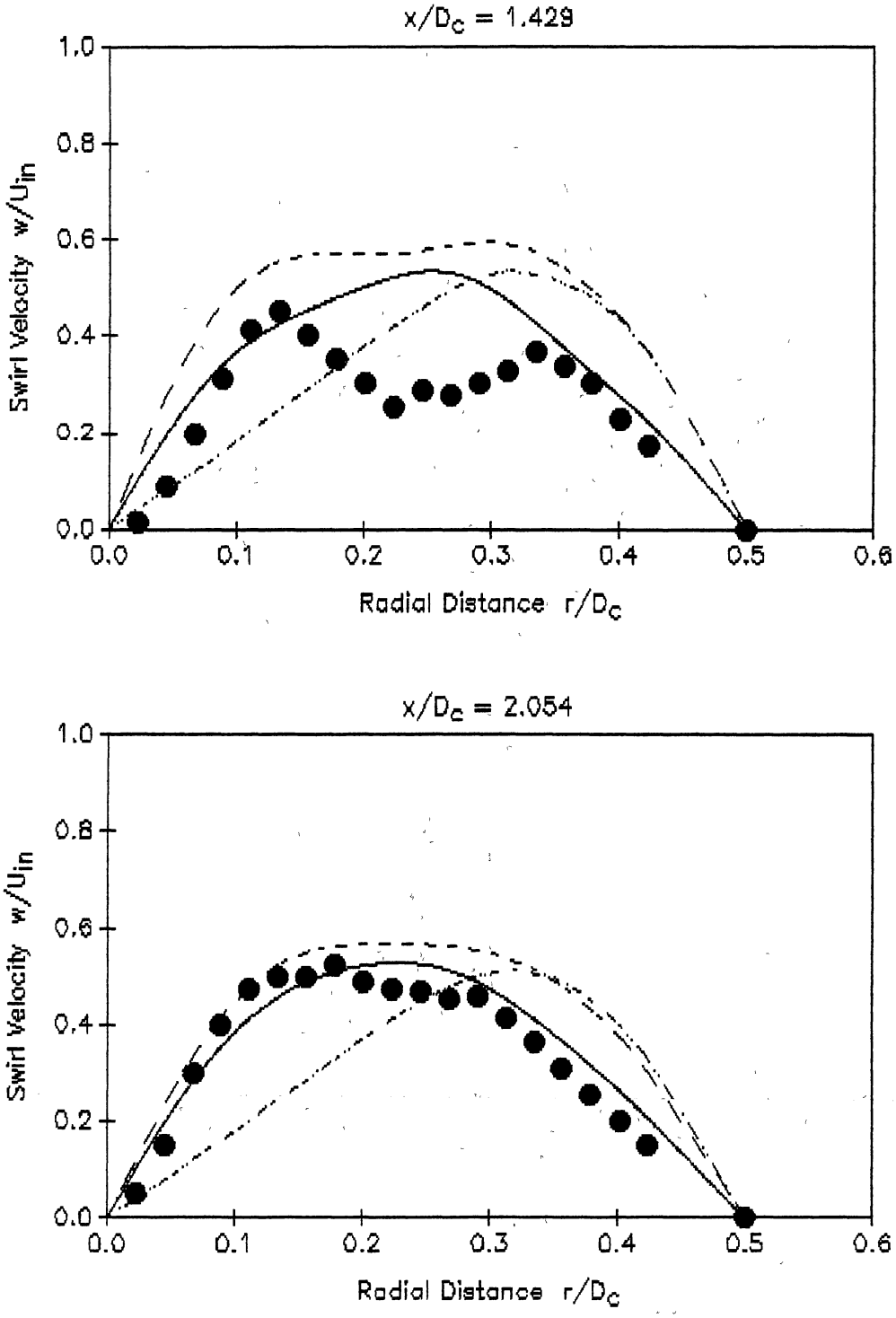

Figure 15 (Continued)

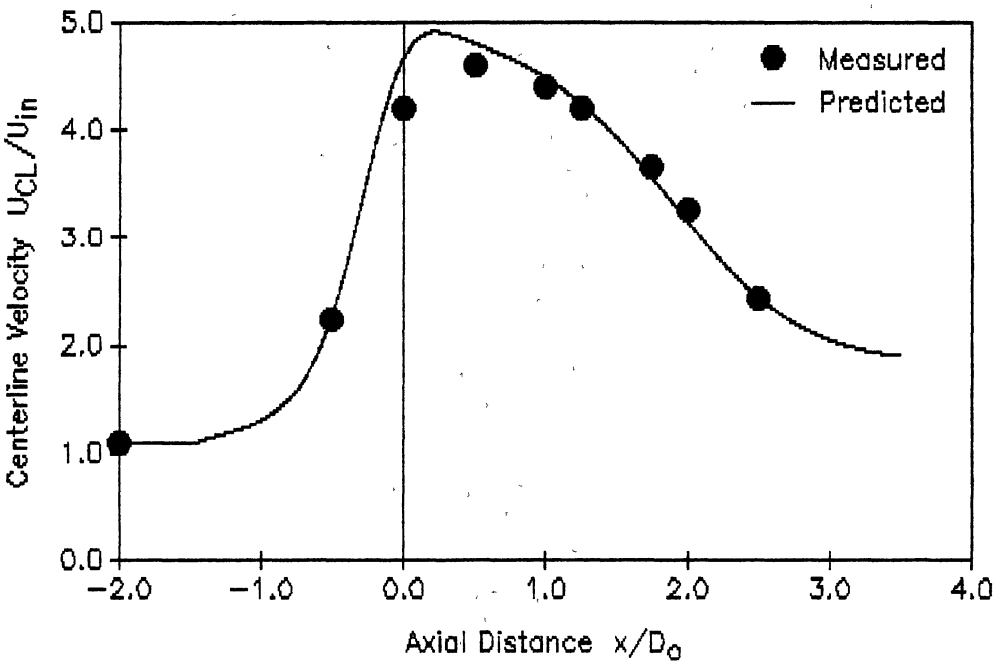

Figure 16. Case 3; Comparison of Predicted and Measured Centerline velocity [Deshpande & Giddens, Ref. 77]

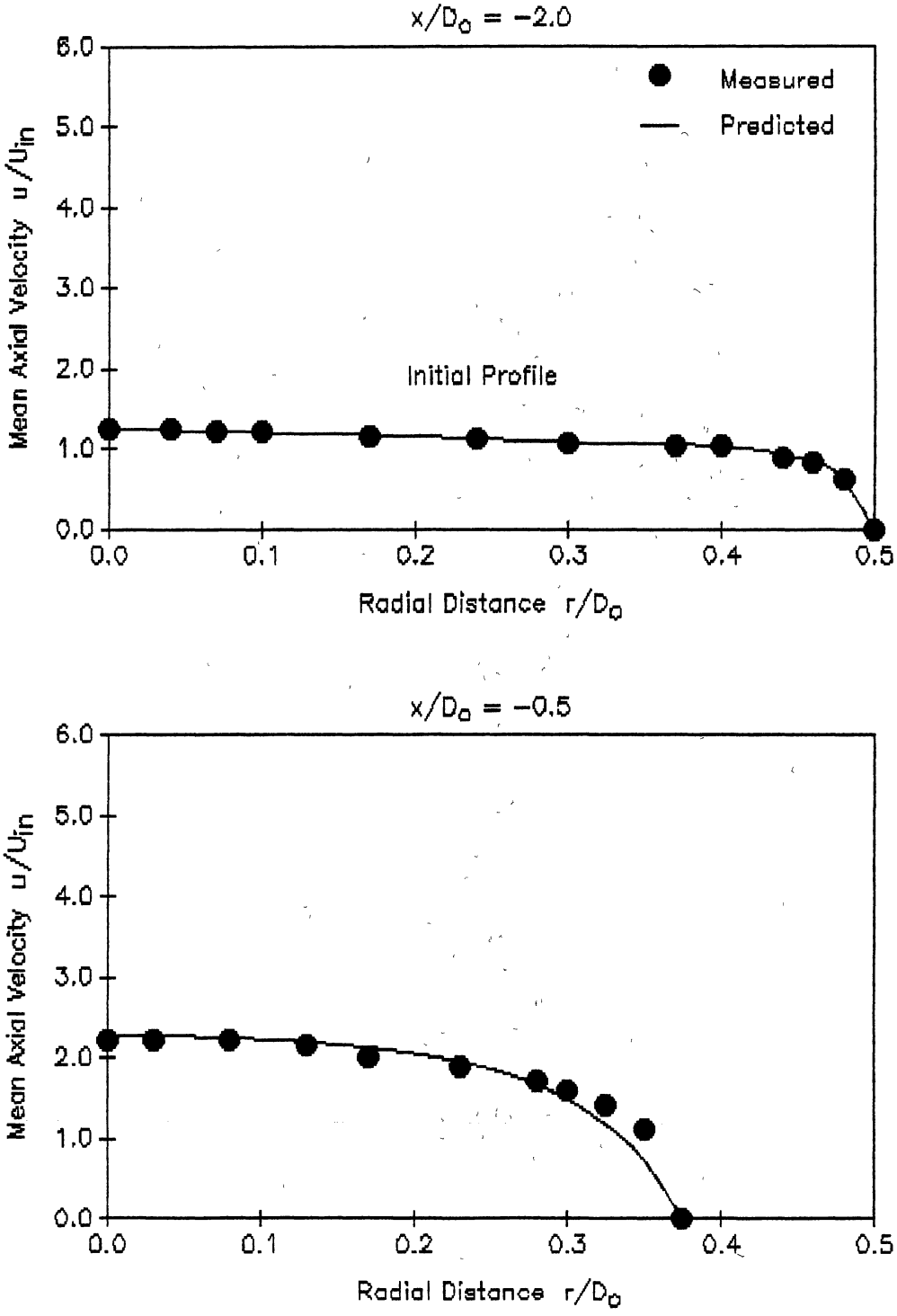

Figure 17. Case 3; Comparison of Predicted and Measured Axial Velocity Profiles [Deshpande & Giddens, Ref. 77]

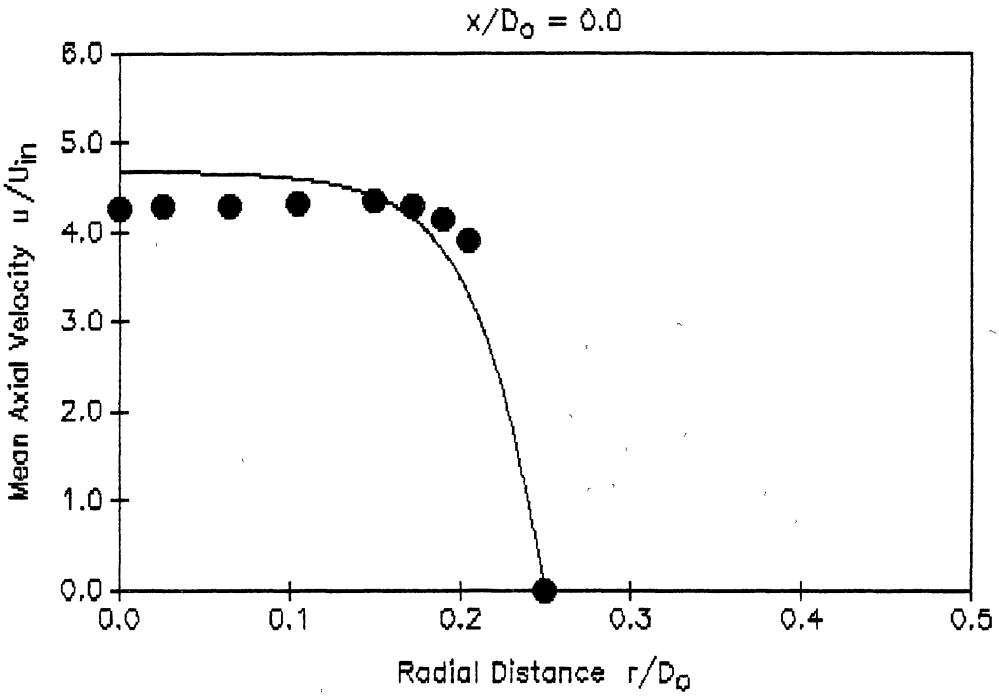

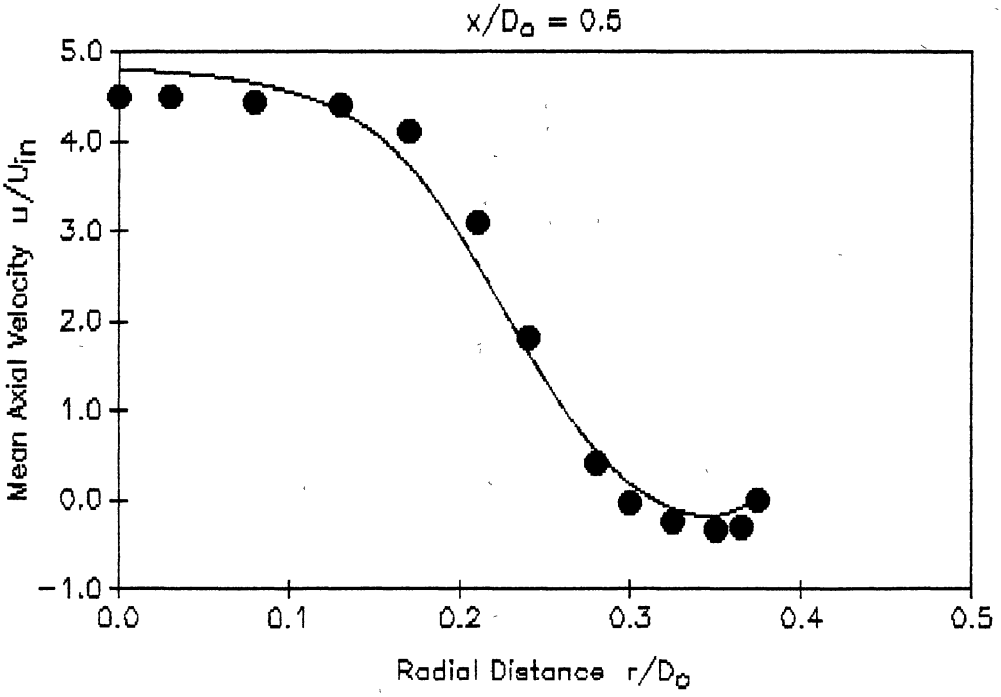

Figure 17 (Continued)

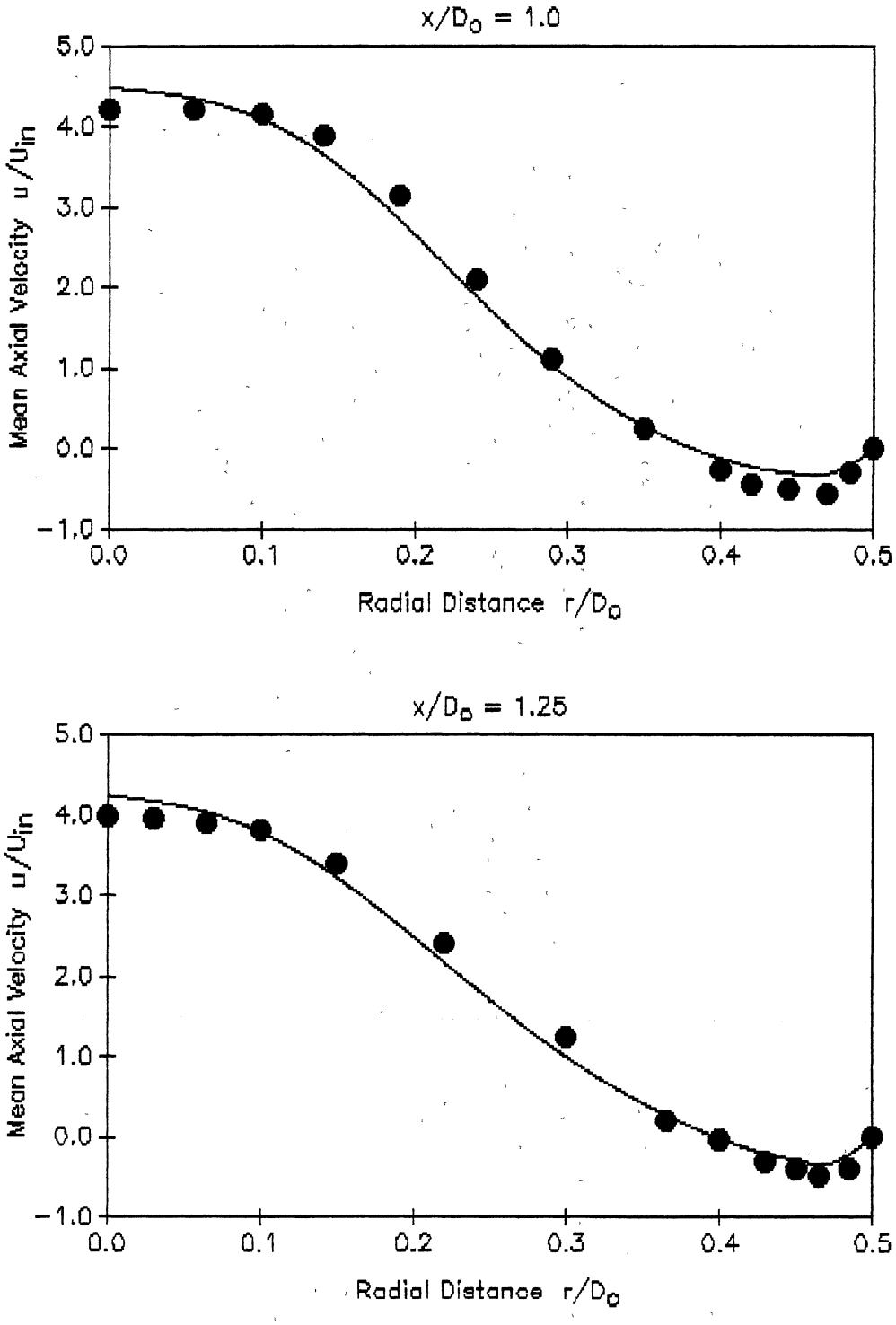

Figure 17 (Continued)

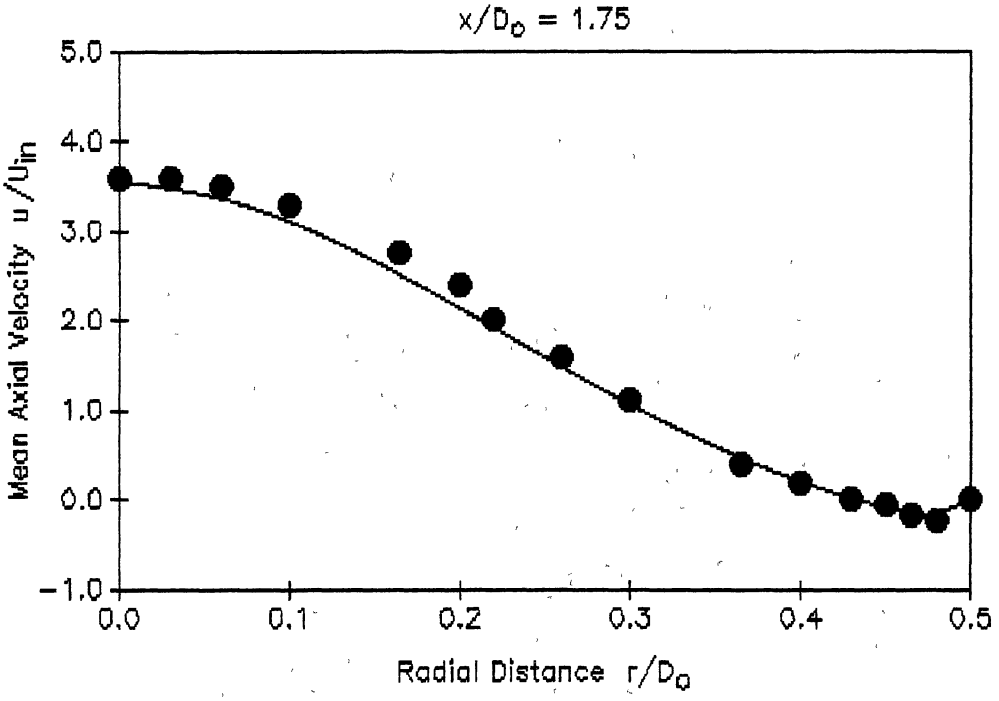

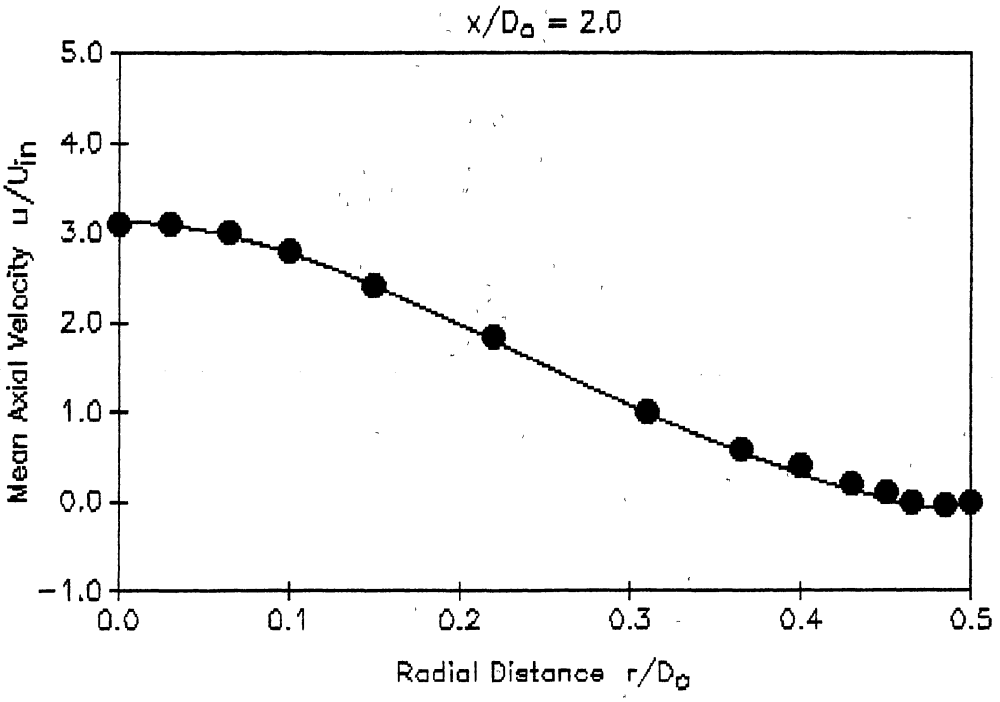

Figure 17 (Continued)

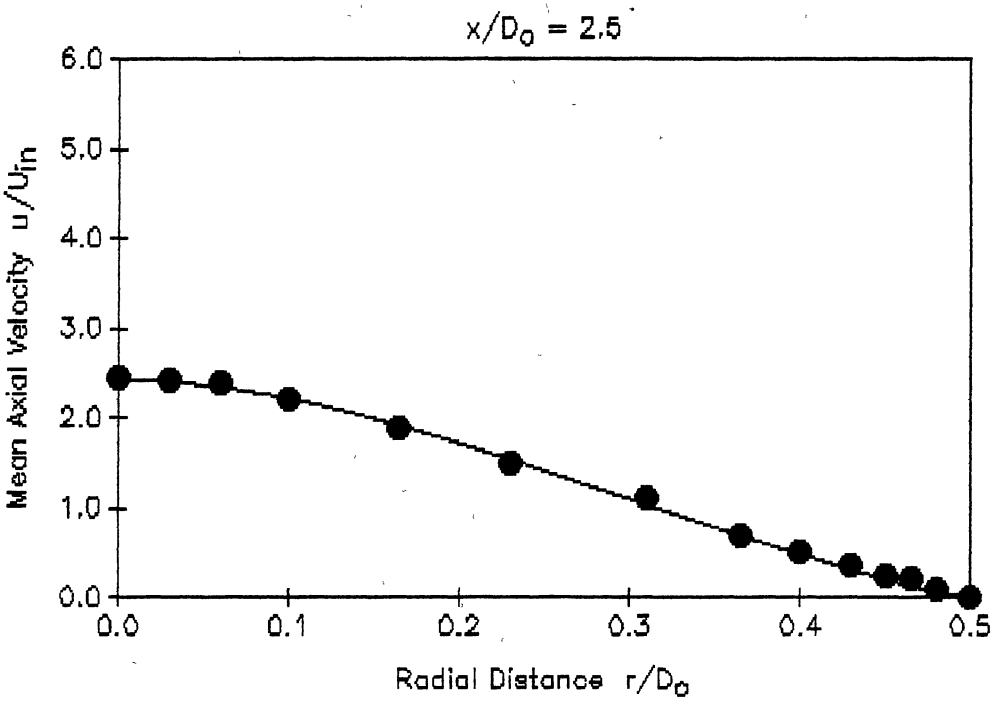

Figure 17 (Continued)

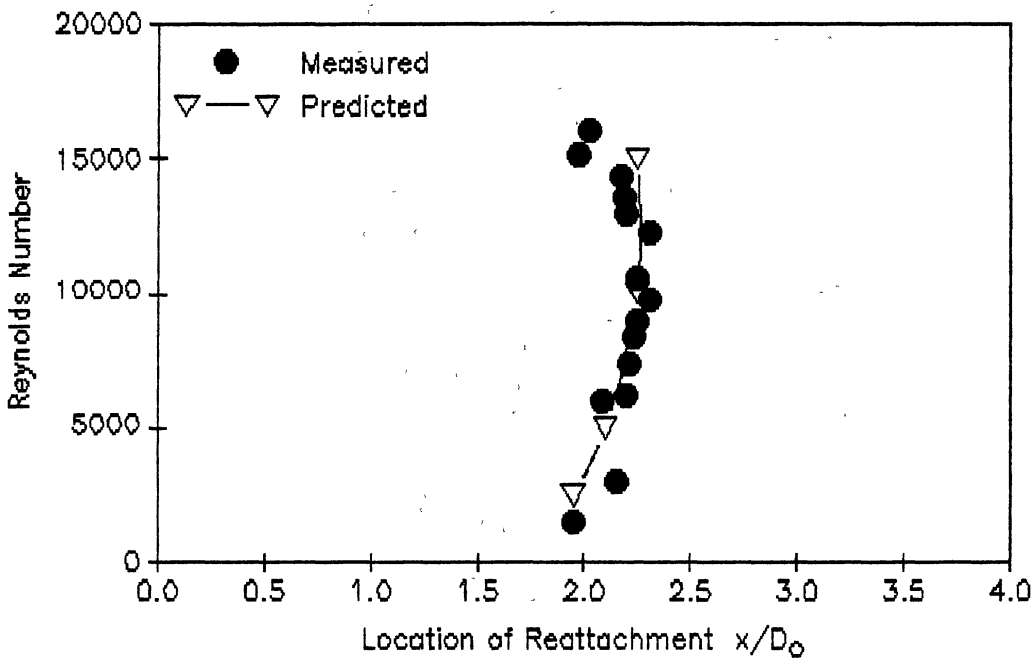

Figure 18. Case 3; Comparison of Predicted and Measured Location of Reattachment for Various Reynolds Numbers [Deshpande & Giddens, Ref. 77]

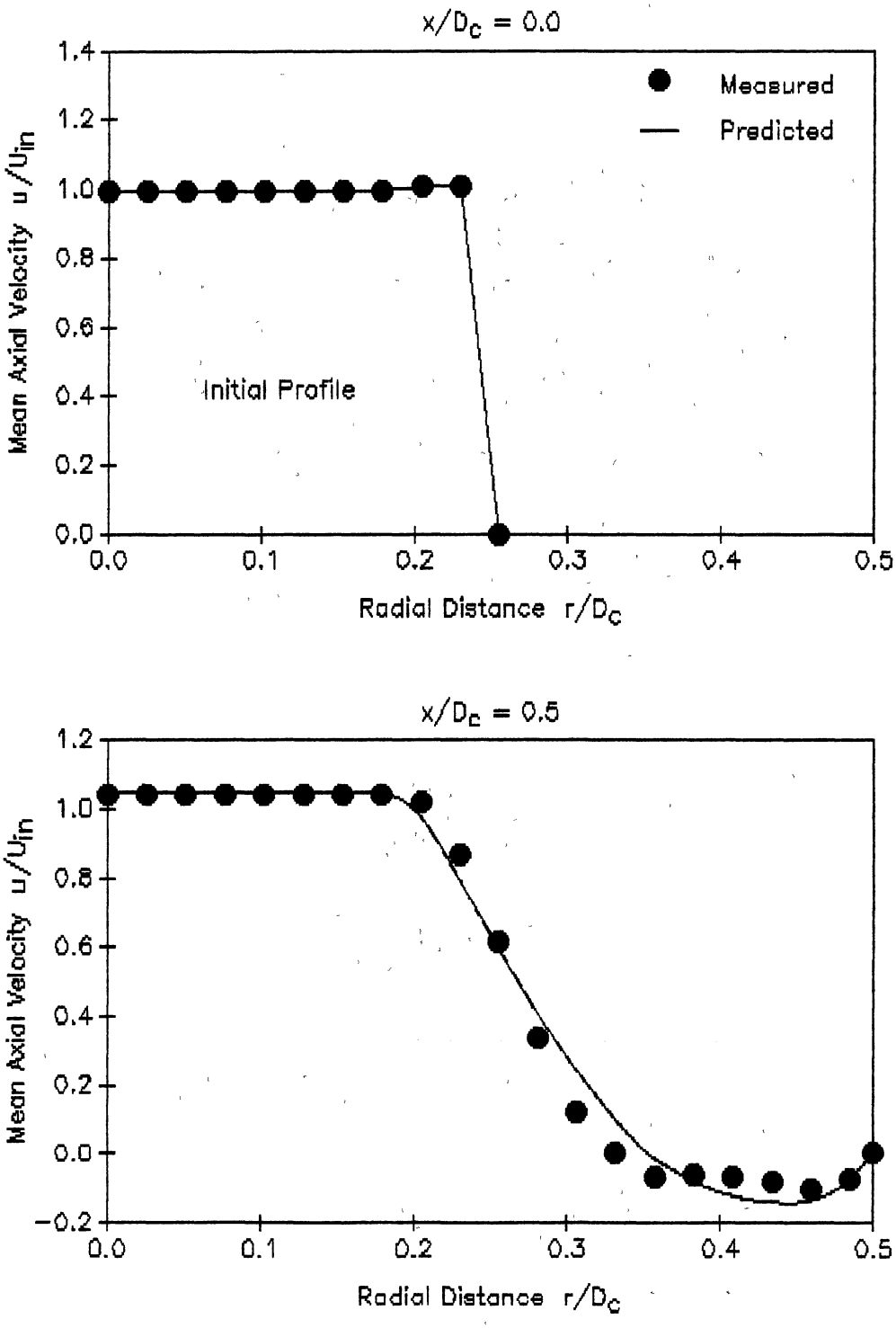

Figure 19. Case 4; Comparison of Predicted and Measured Axial Velocity Profiles [Yoon & Lilley, Ref. 47]

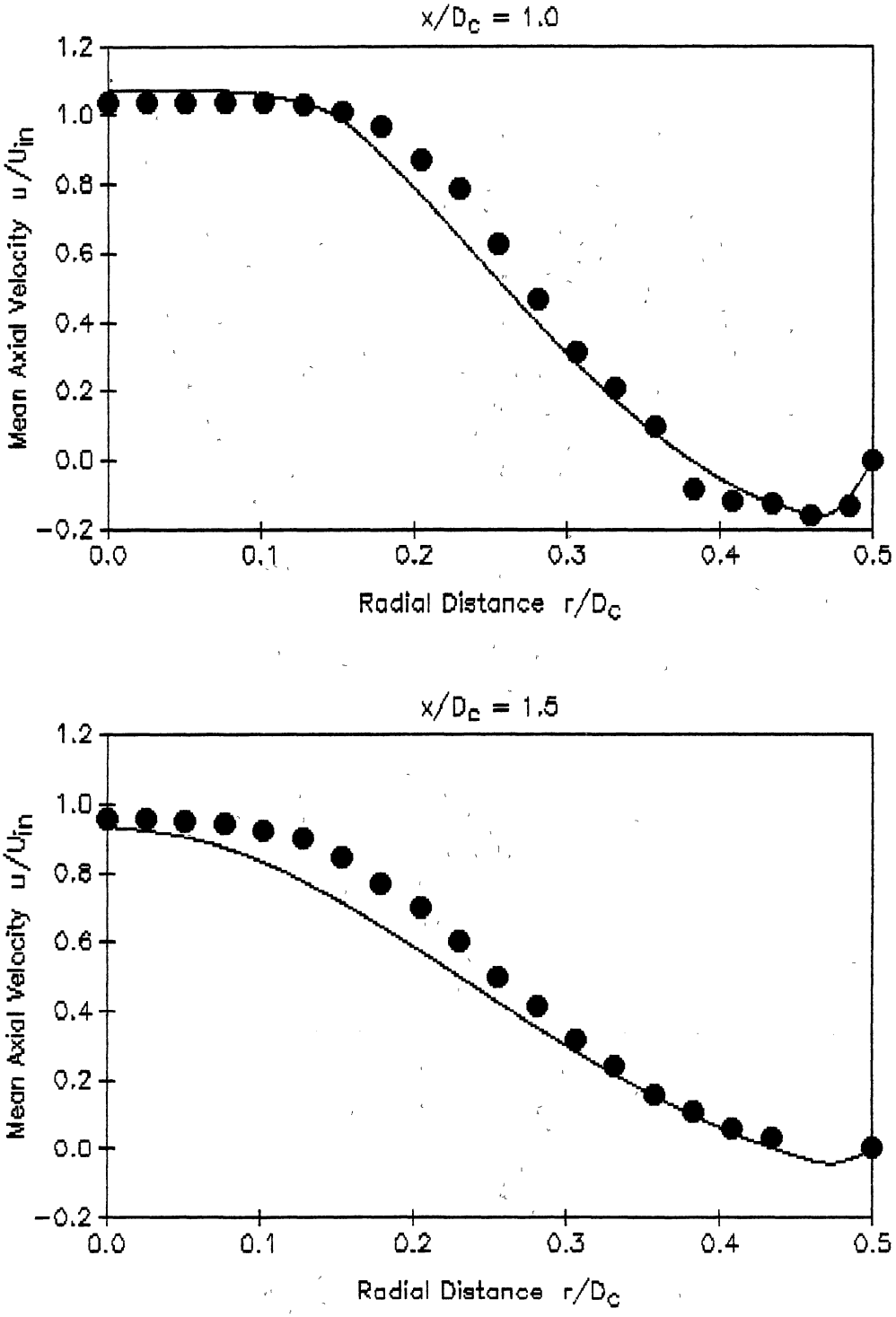

Figure 19 (Continued)

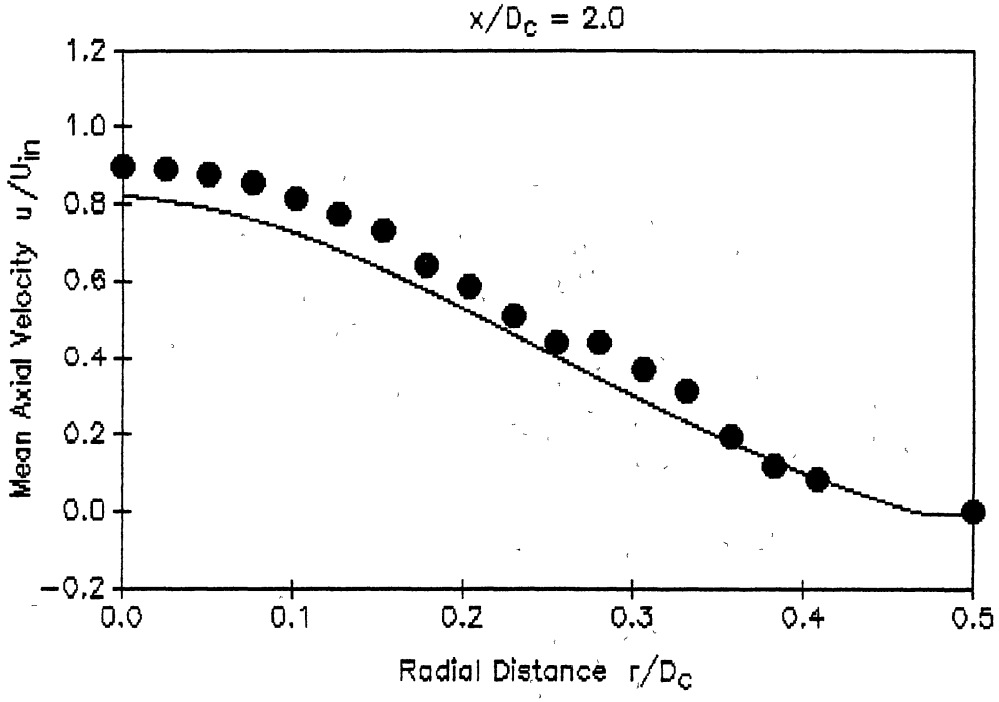

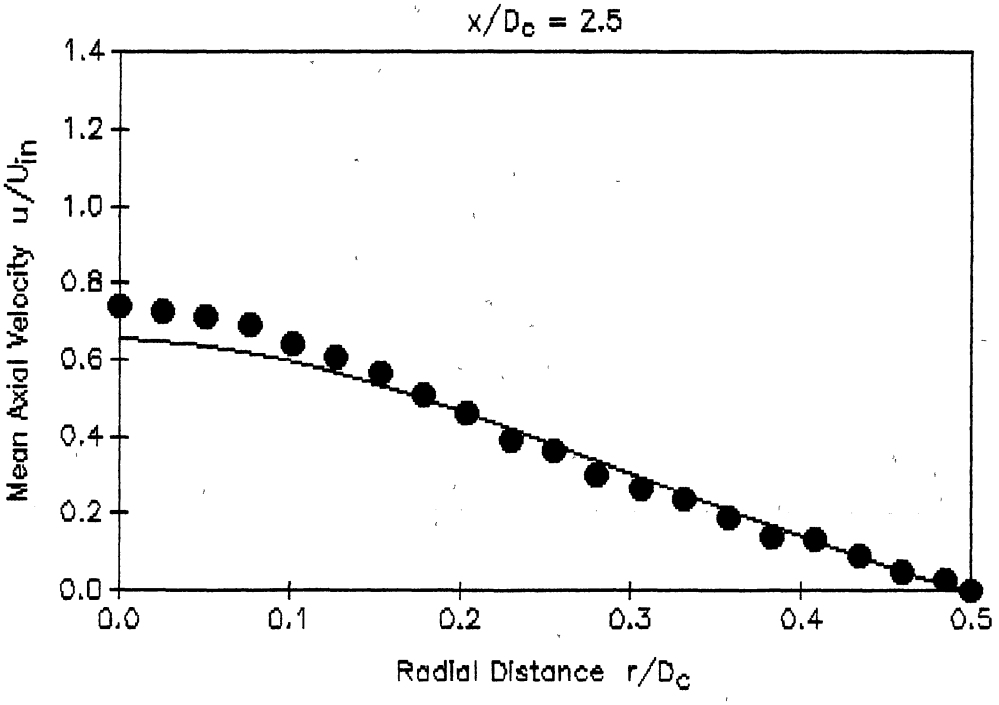

Figure 19 (Continued)

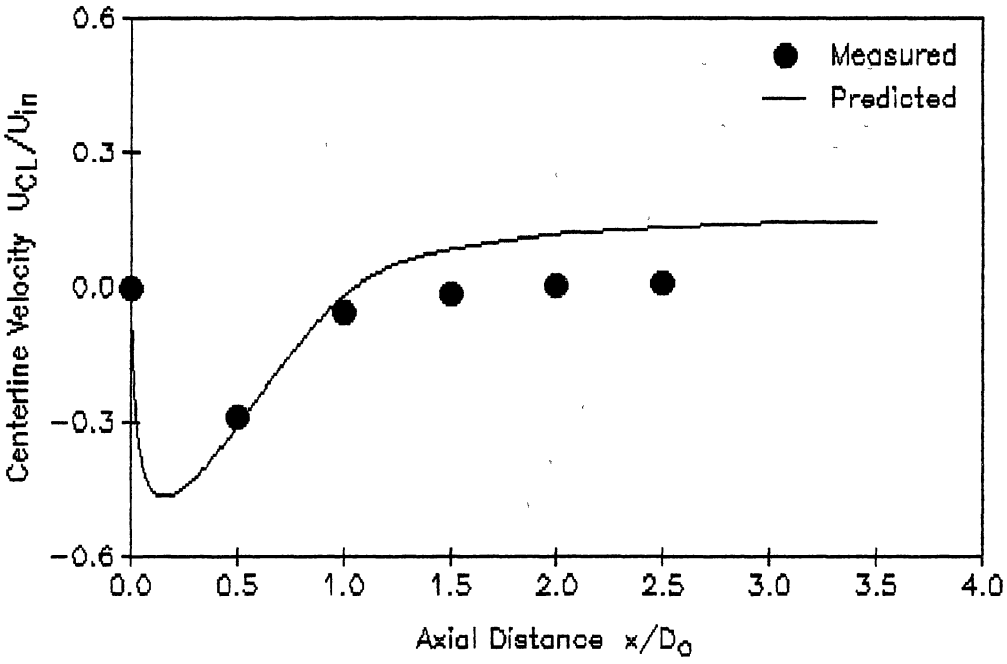

Figure 20. Case 5; Comparison of Predicted and Measured Centerline velocity [Yoon & Lilley, Ref. 47]

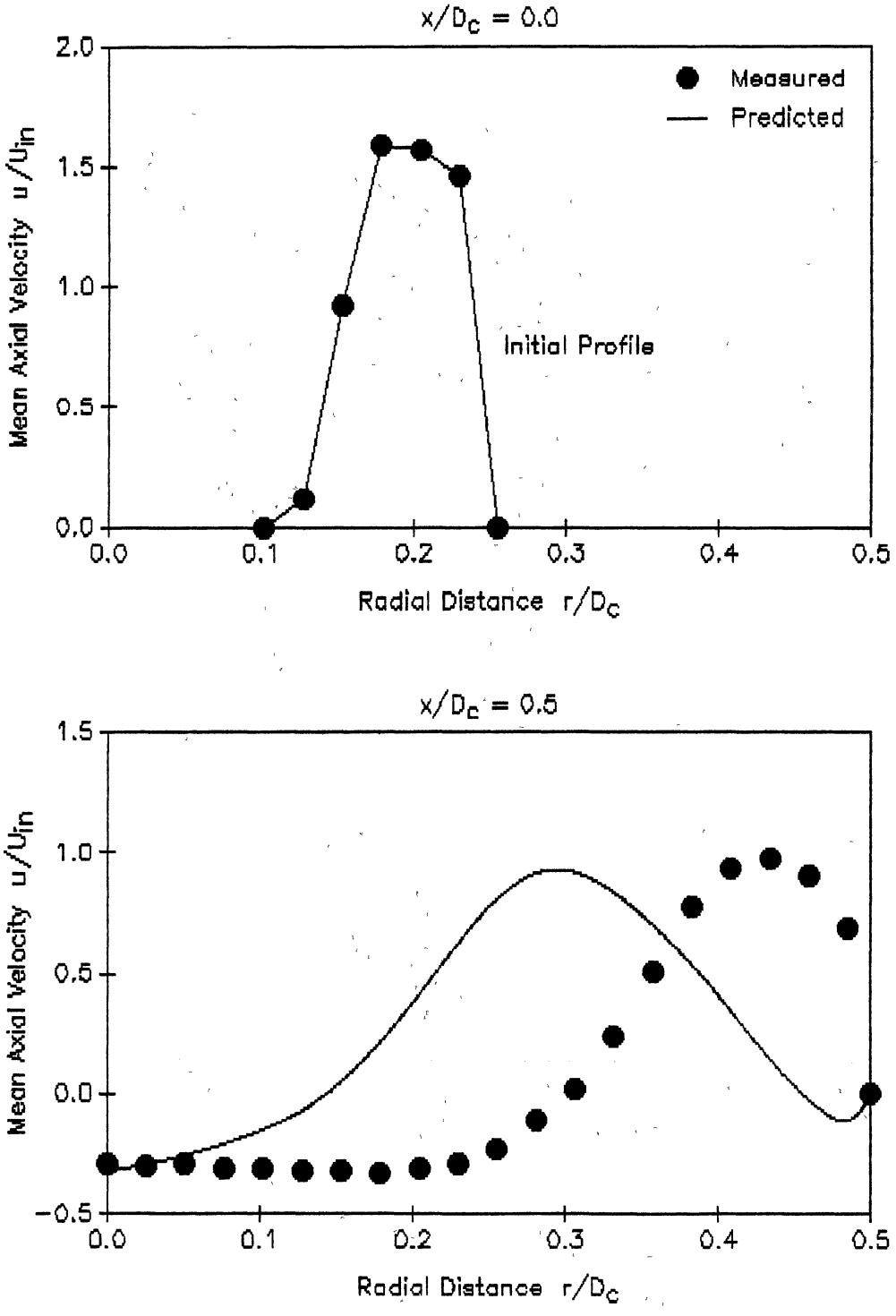

Figure 21. Case 5; Comparison of Predicted and Measured Axial Velocity Profiles [Yoon & Lilley, Ref. 47]

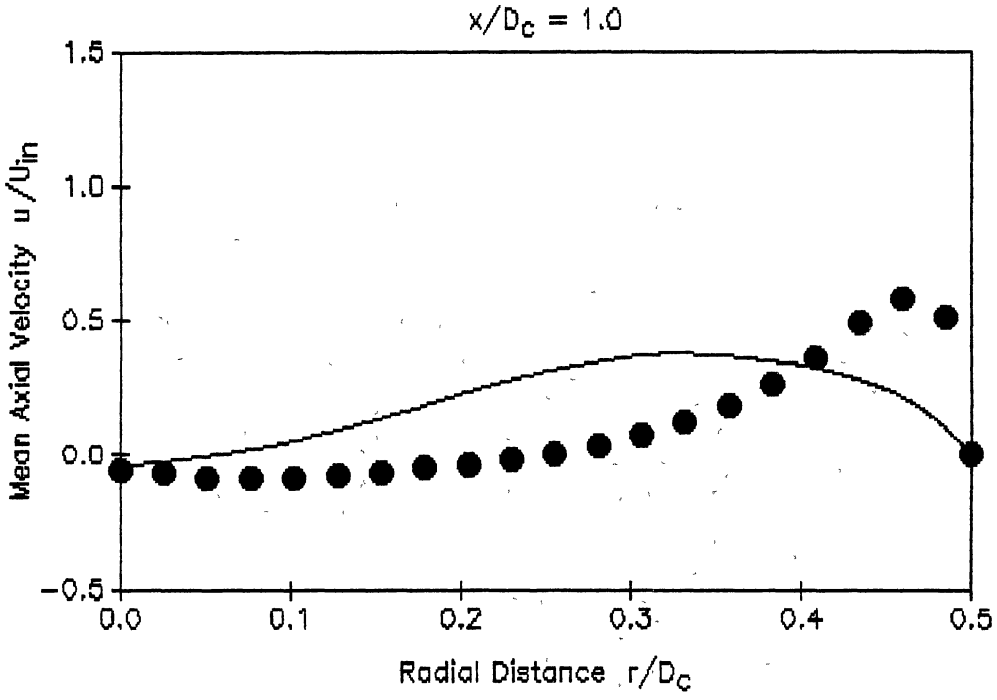

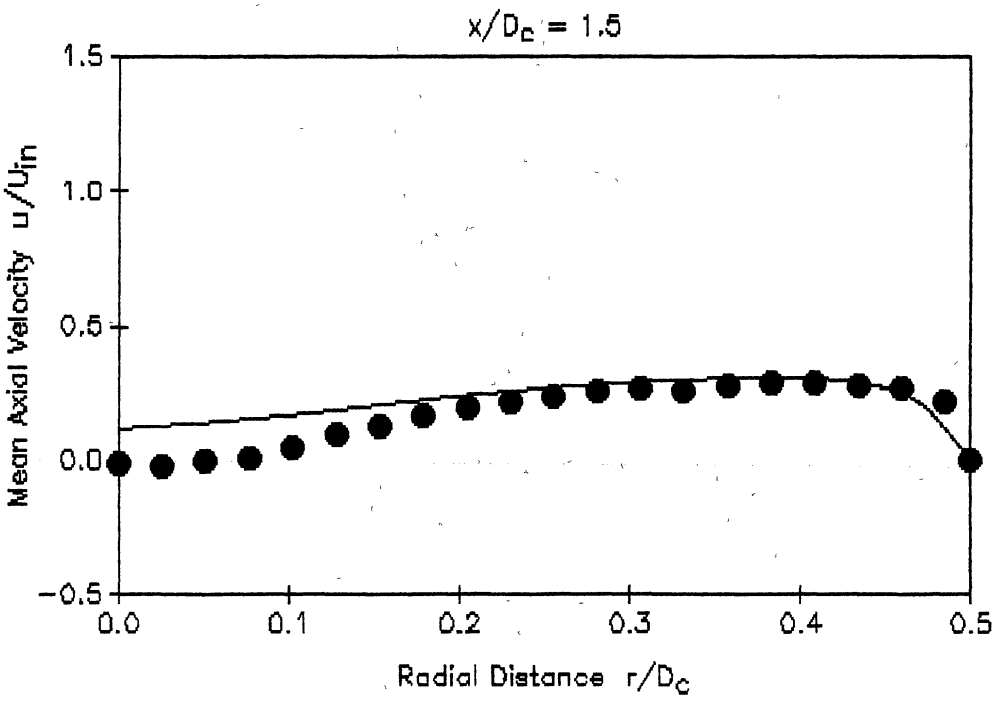

Figure 21 (Continued)

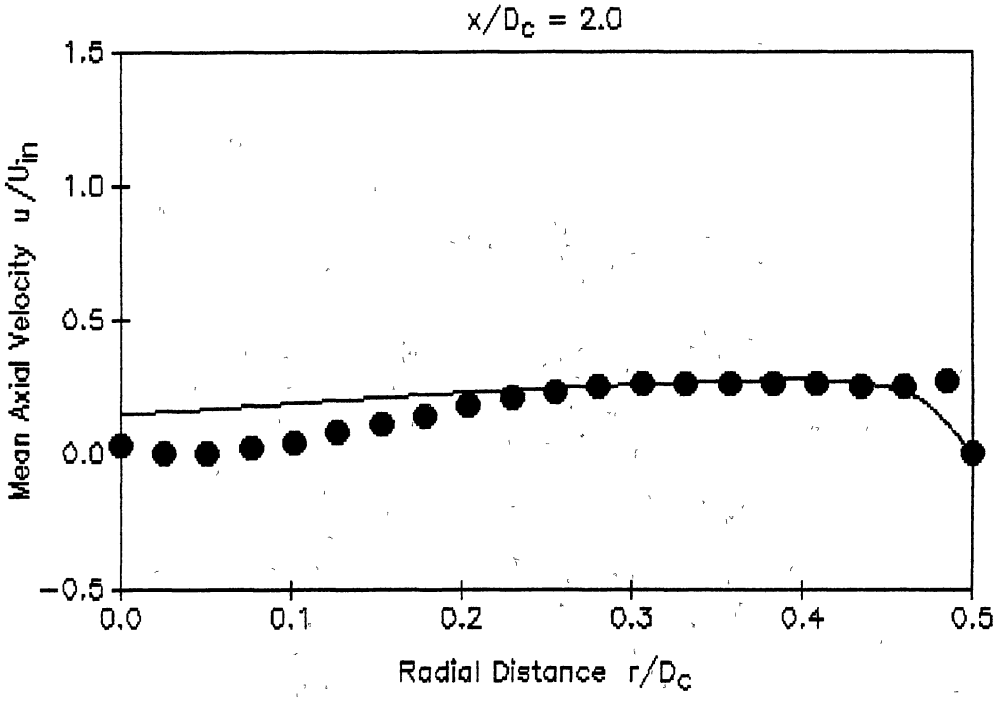

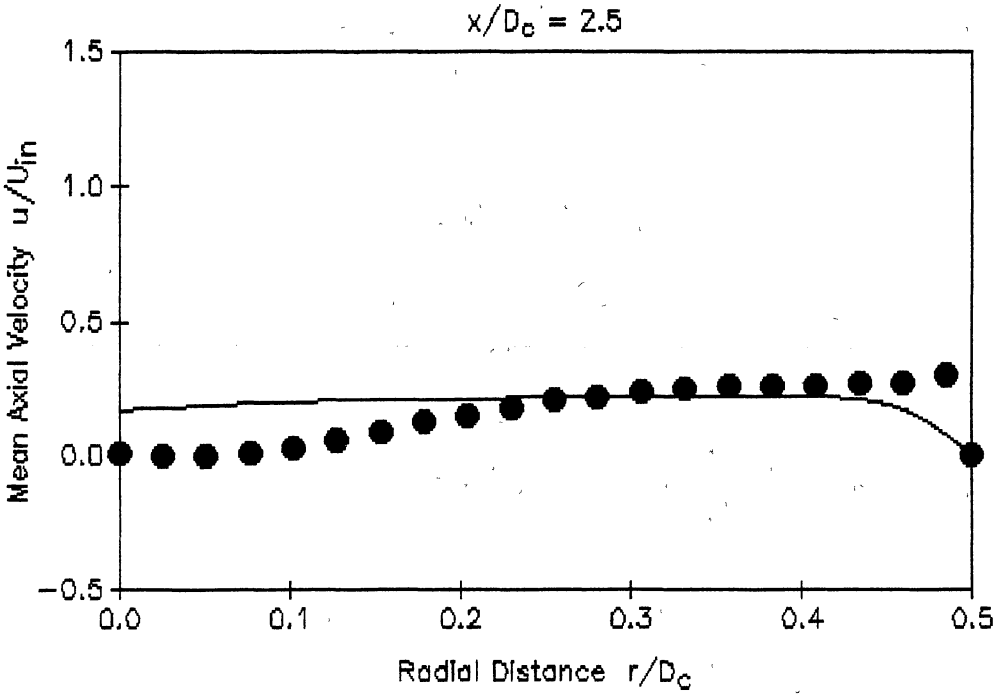

Figure 21 (Continued)

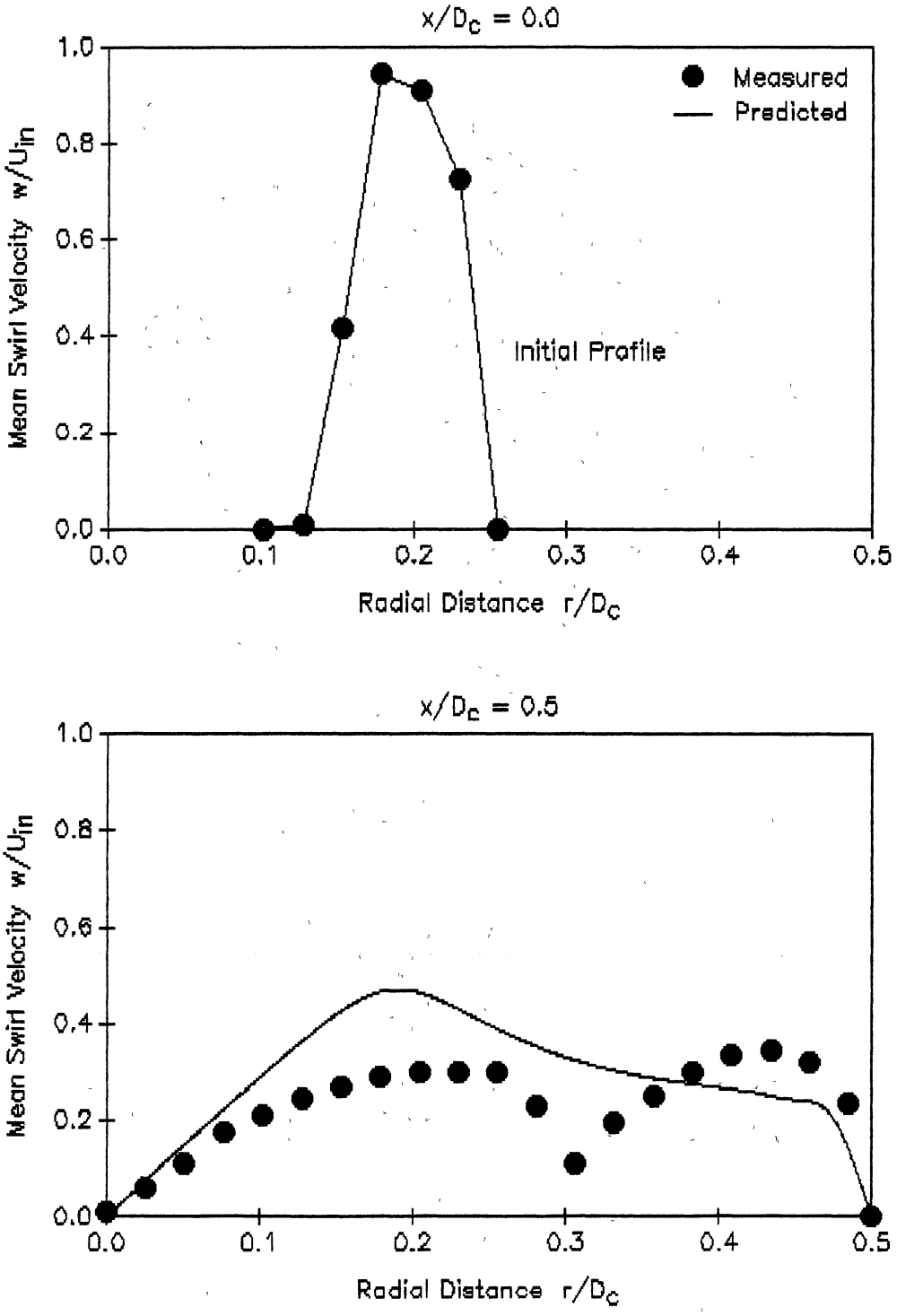

Figure 22. Case 5; Comparison of Predicted and Measured Swirl Velocity Profiles [Yoon & Lilley, Ref. 47]

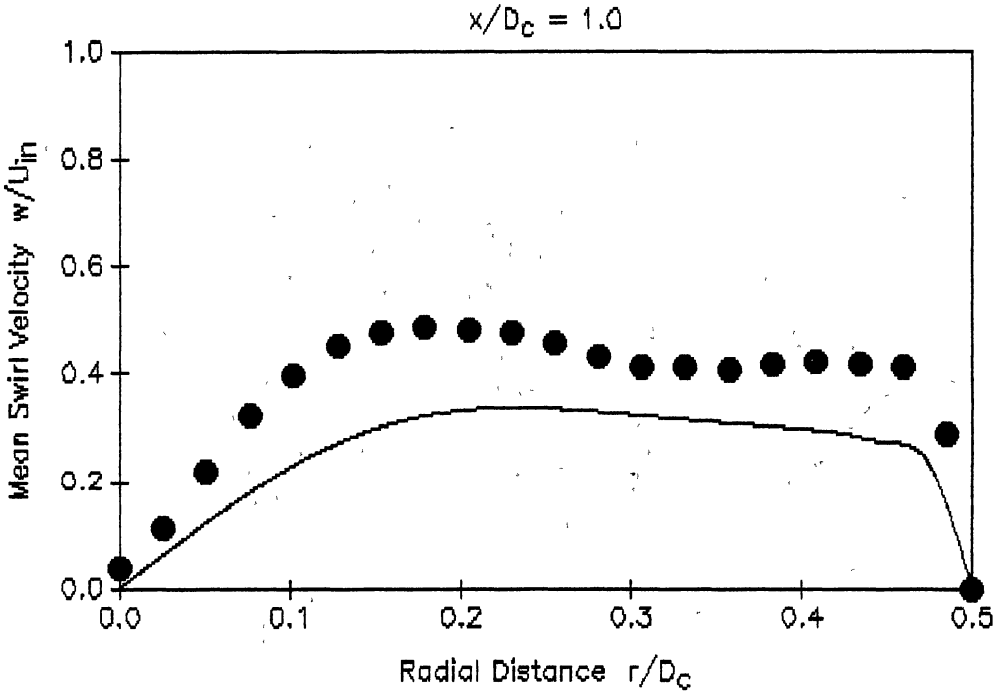

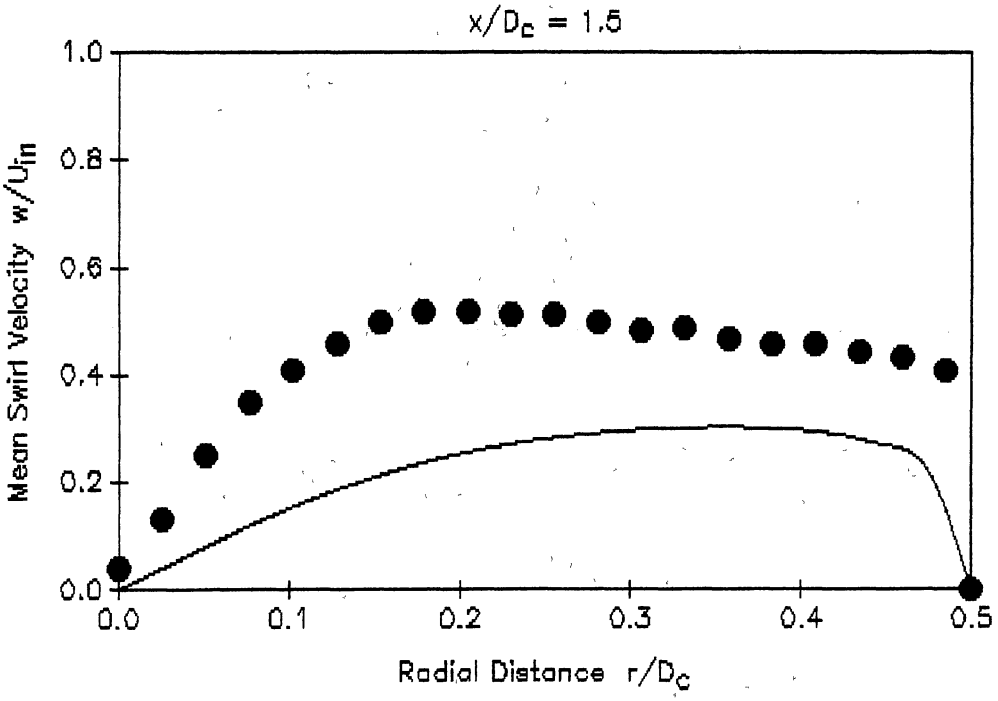

Figure 22 (Continued)

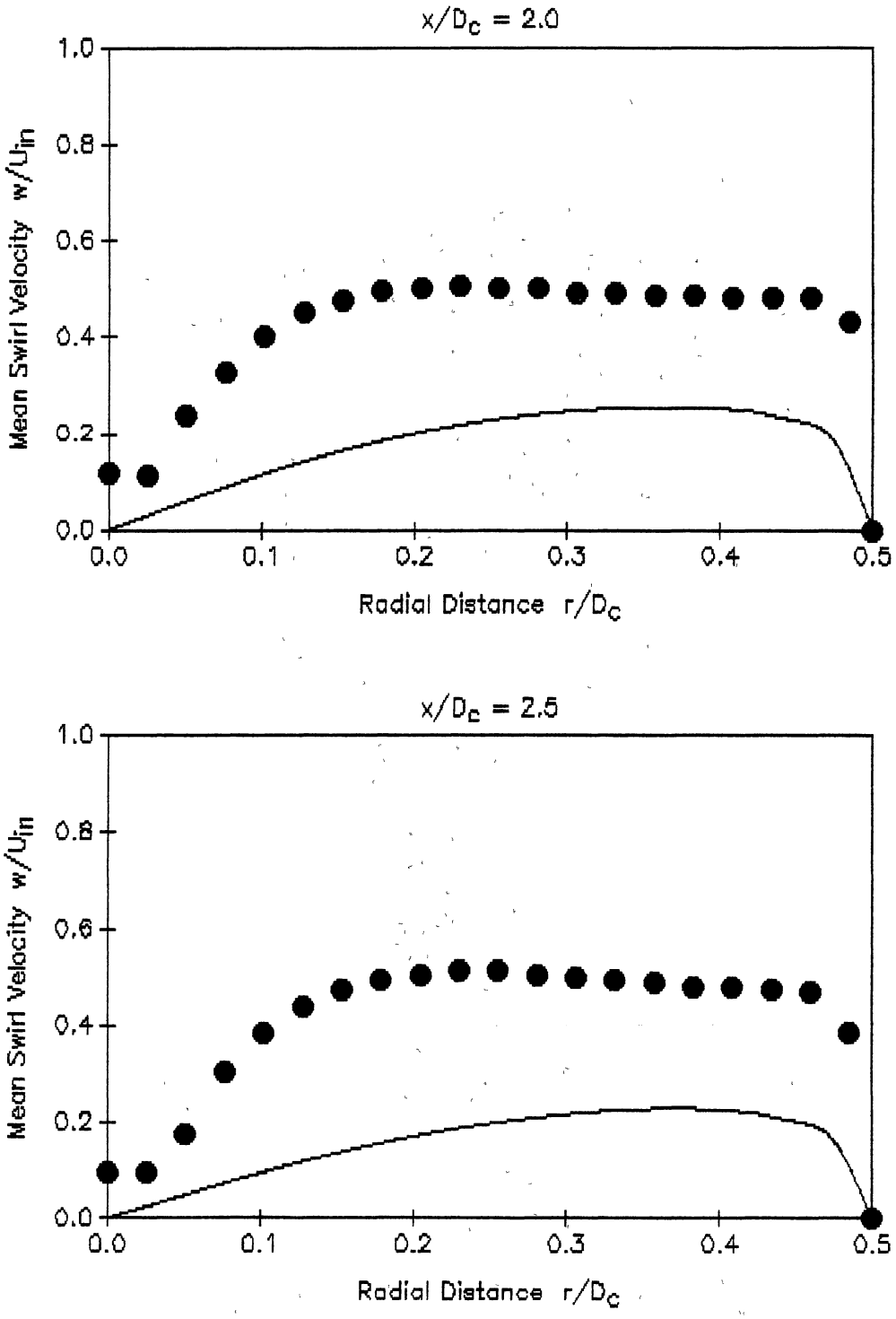

Figure 22 (Continued)

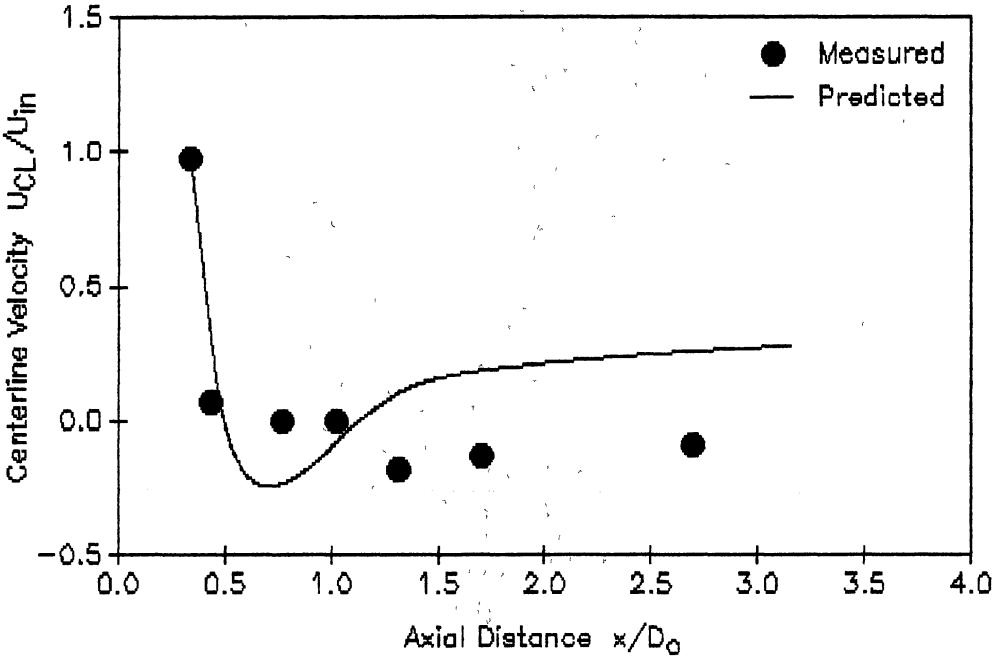

Figure 23. Case 6; Comparison of Predicted and Measured Centerline velocity [Weber et al., Ref. 54]

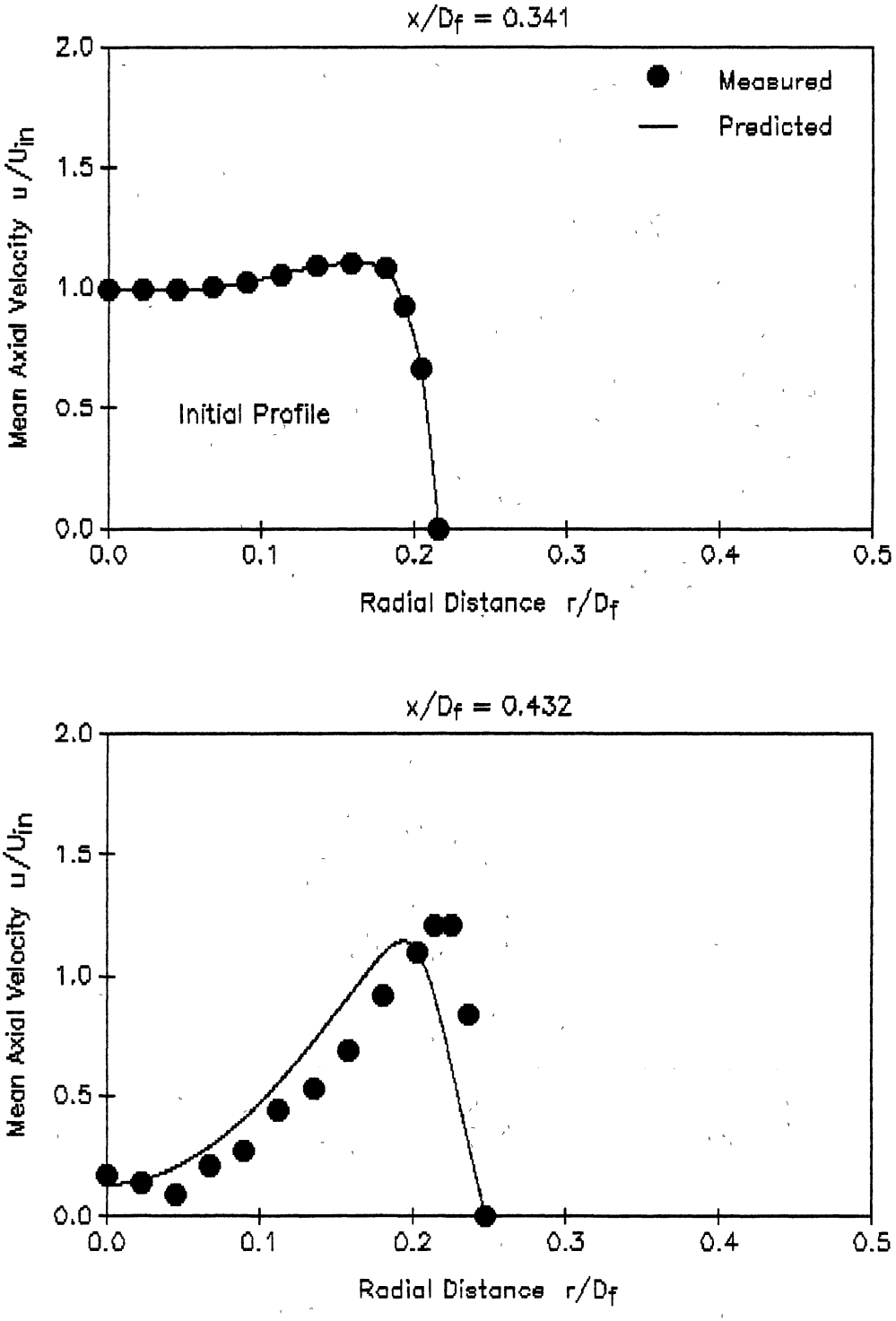

Figure 24. Case 6; Comparison of Predicted and Measured Axial Velocity Profiles [Weber et al., Ref. 54]

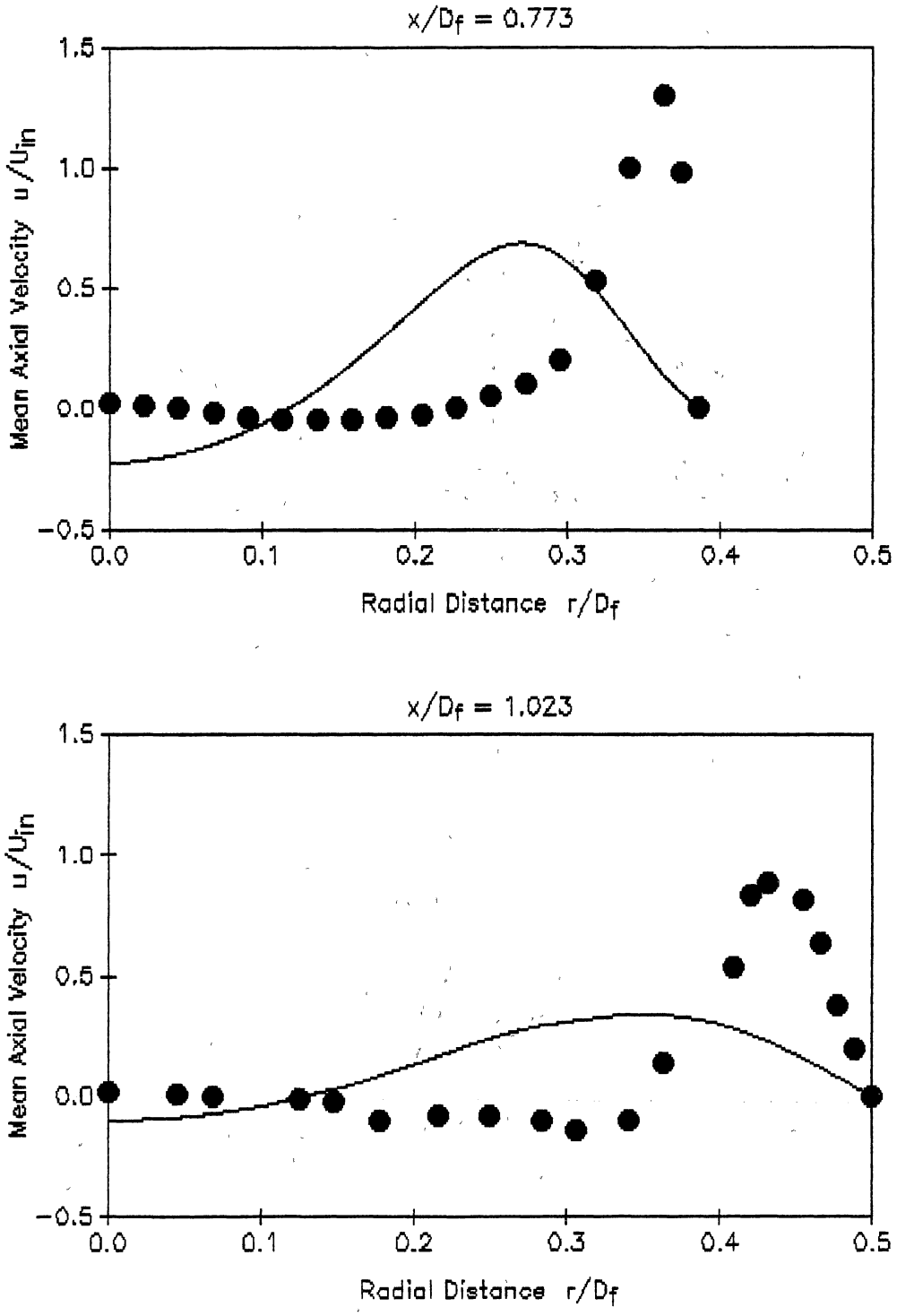

Figure 24 (Continued)

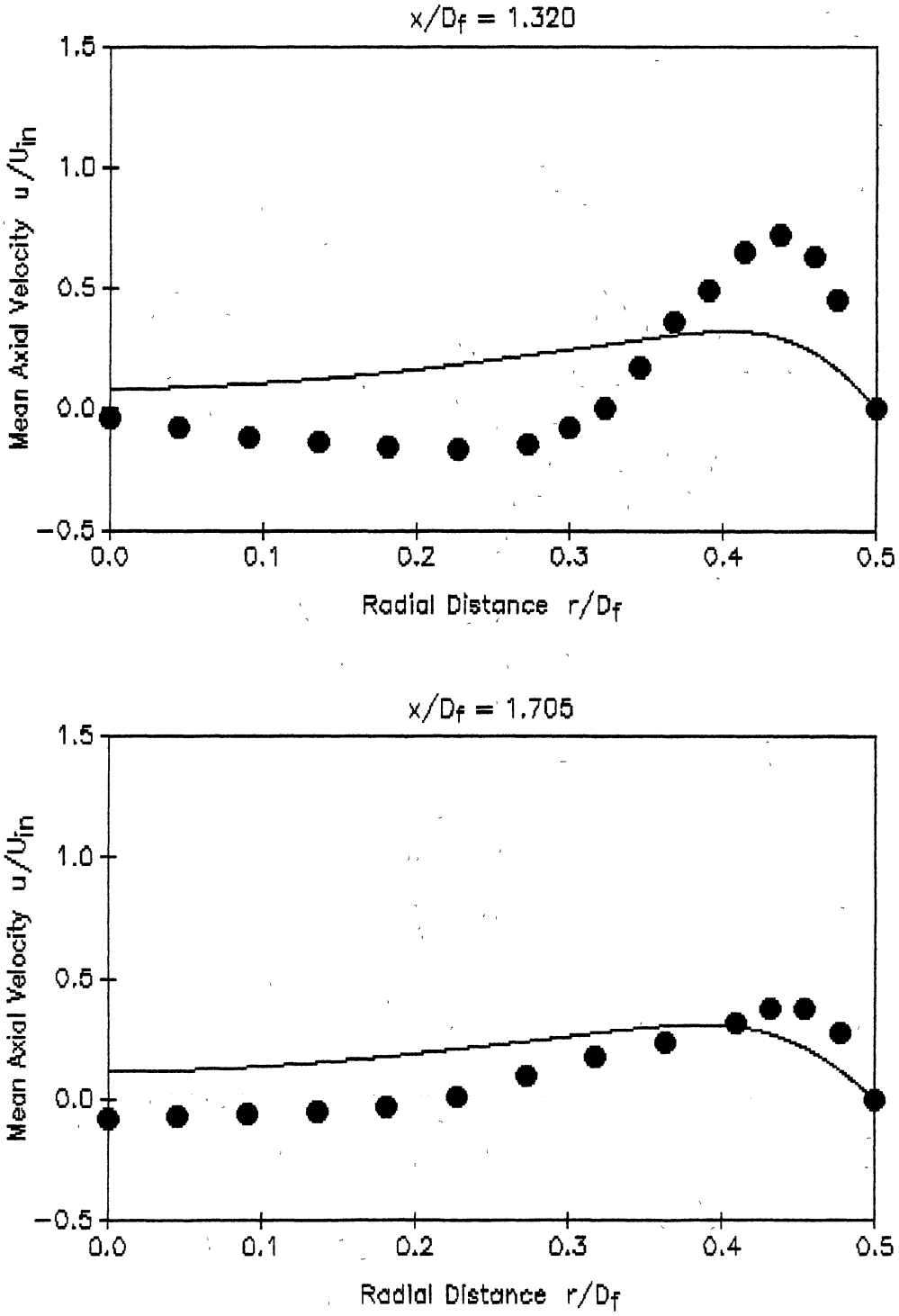

Figure 24 (Continued)

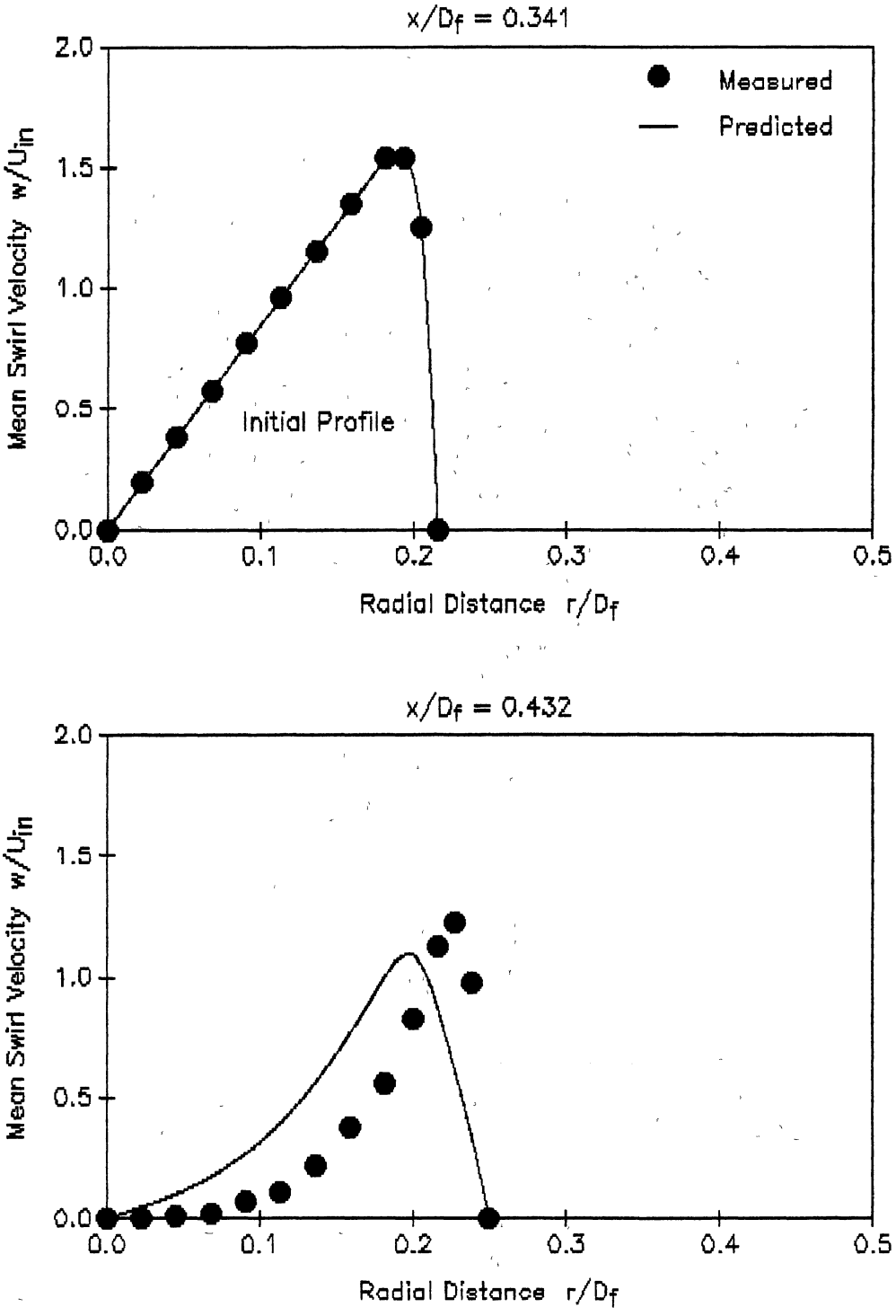

Figure 25. Case 6; Comparison of Predicted and Measured Swirl Velocity Profiles [Weber et al., Ref. 54]

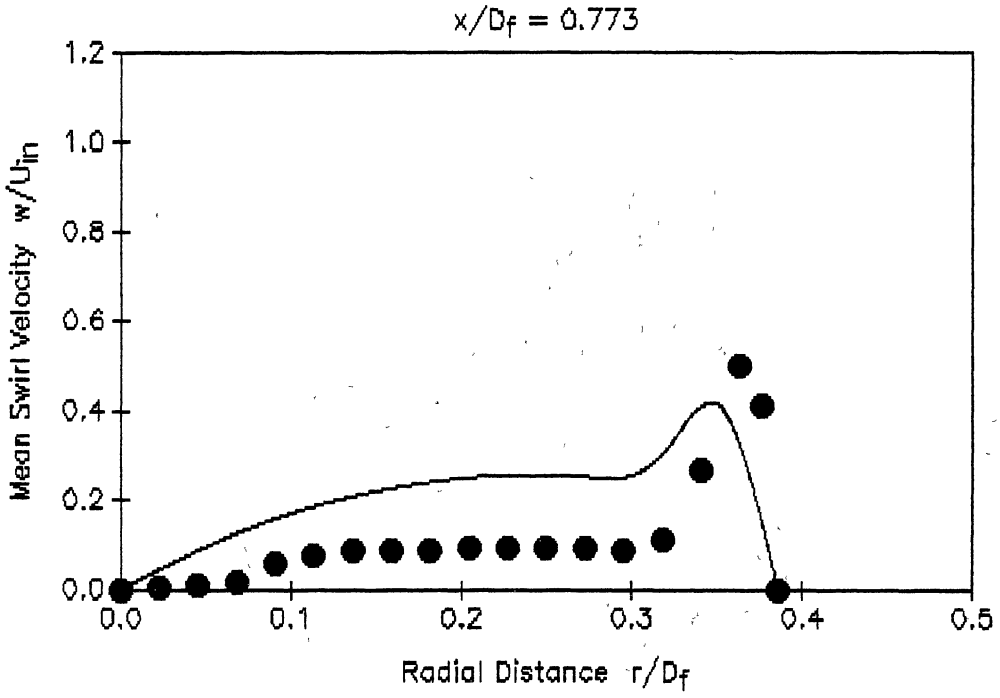

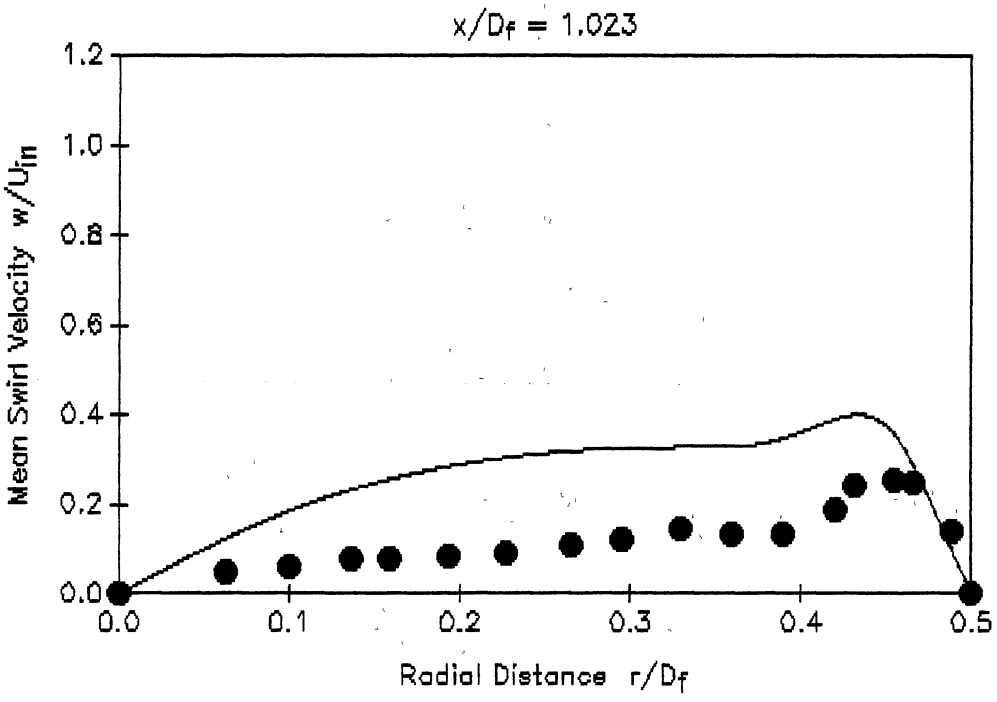

Figure 25 (Continued)

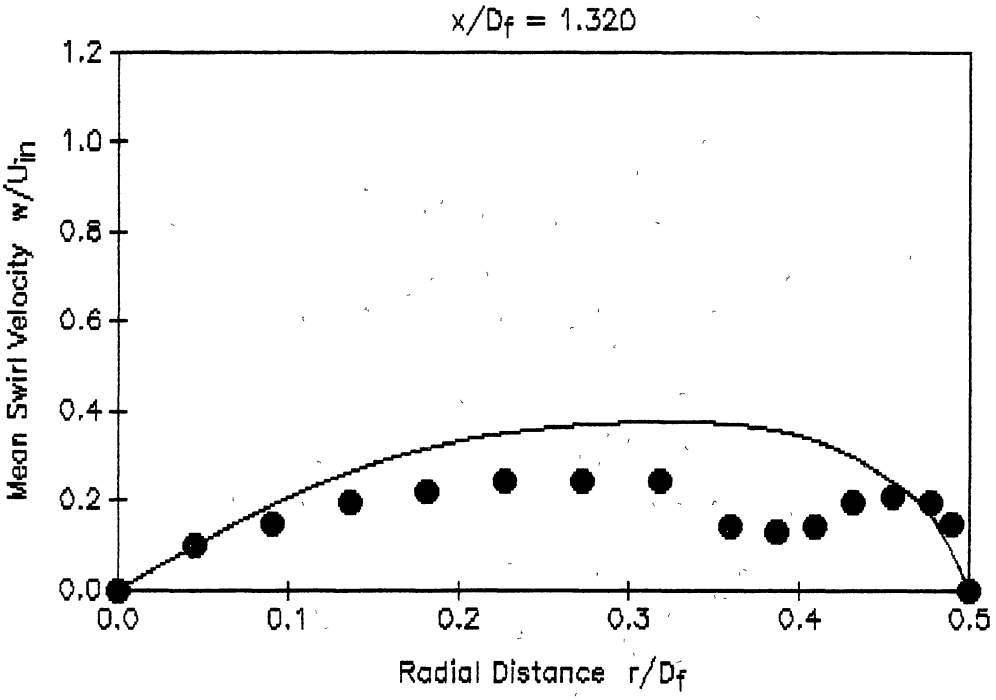

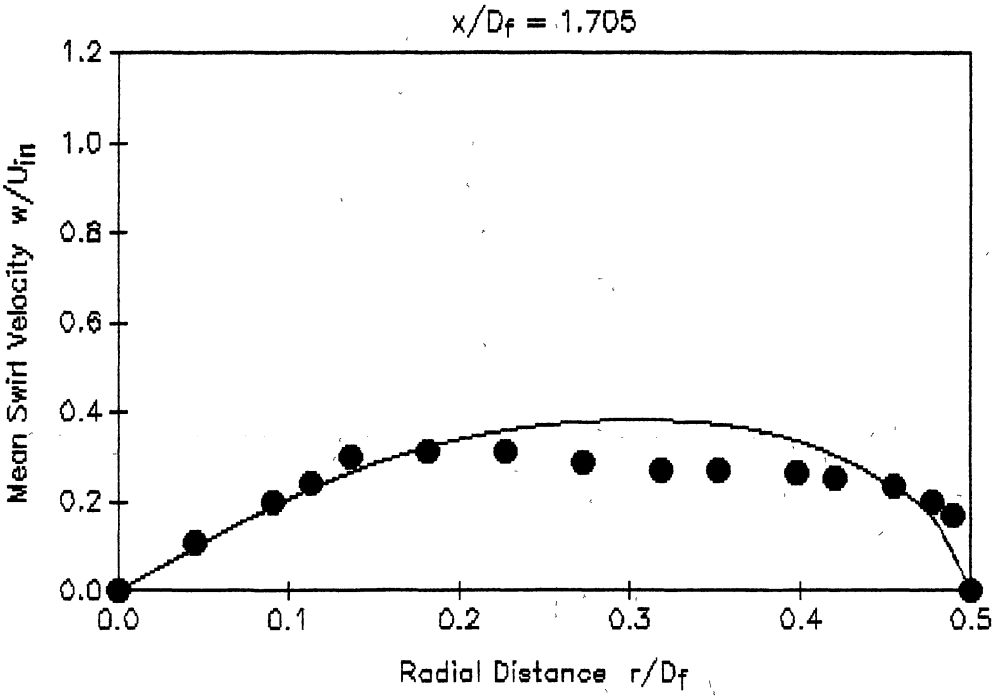

Figure 25 (Continued)

VITA

Afif S. Halal

Candidate for the Degree of

Doctor of Philosophy

Thesis: A BOUNDARY-FITTED NON-ORTHOGONAL GRID TECHNIQUE FOR INCOMPRESSIBLE TURBULENT SWIRLING FLOWS

Major Field: Mechanical Engineering

Biographical:

Personal Data: Born in Habbouche, Lebanon, March 25, 1961, the son of Samih F. and Fatima H. Hallal.

Education: Graduated from Raml El-Zarif High School, Beirut, Lebanon, 1979; received a Bachelor of Science Degree in Mechanical Engineering from Oklahoma State University in May, 1982; received a Master of Science Degree in Mechanical Engineering from Oklahoma State University in December, 1983; completed requirements for the Doctor of Philosophy degree at Oklahoma State University in December 1991.

Professional Experience: Manufacturing Engineer, Lakewood Engineering, Downey, California, 1984-1985; Teaching Assistant, School of Mechanical and Aerospace Engineering, Oklahoma State University, 1985-1987; Manager, Advanced Computing Facility, College of Engineering, Architecture, and Technology, Oklahoma State University, 1988-1990; Lecturer, School of Mechanical and Aerospace Engineering, Oklahoma State University, 1988-1991.

Honorary Organizations: Pi Tau Sigma, Tau Beta Pi

Professional Organizations: ASME